



UNIVERSITÀ DEGLI STUDI DI NAPOLI FEDERICO II

FACOLTÀ DI INGEGNERIA

DIPARTIMENTO DI INGEGNERIA AEROSPAZIALE



DOTTORATO DI RICERCA IN
INGEGNERIA AEROSPAZIALE, NAVALE, E DELLA QUALITÀ
INDIRIZZO AEROSPAZIALE, XX CICLO

THE VIBROACOUSTIC BEHAVIOUR OF AEROSPACE STRUCTURES.
EXPERIMENTAL MEASUREMENTS AND SIMULATIONS ACCOUNTING FOR
UNCERTAINTIES

TUTOR:
CH.MO PROF. ING
FRANCESCO MARULO

CANDIDATO:
TIZIANO POLITO

COORDINATORE CORSO DI DOTTORATO:
CH.MO PROF. ING:
ANTONIO MOCCIA

NOVEMBRE 2007

*...dai diamanti non nasce niente, dal letame nascono i fiori
(...from diamonds nothing originates, from manure flowers rise)*

Fabrizio De Andrè, Via del Campo, 1967

TABLE OF CONTENTS

ACKNOWLEDGEMENTS	5
LIST OF TABLES	6
LIST OF FIGURES	7
SUMMARY	10
INTRODUCTION	11
1 PHYSICAL PRINCIPLES OF SOUND	16
1.1 SOUND WAVES	18
1.1.1 Plane sound waves.....	20
1.1.2 Spherical sound waves.....	22
1.2 ACOUSTIC MEASUREMENTS.....	23
1.2.1 The energy in a sound field	24
1.3 OCTAVE FREQUENCY BANDS.....	26
1.4 SOUND LEVELS PERCEPTION	27
1.5 WHITE AND PINK NOISE	29
1.6 SOUND FIELDS.....	30
2 TRANSMISSION LOSS	32
2.1 TRANSMISSION LOSS PREDICTION	34
2.1.1 Mass Law for Normal incidence.....	38
2.1.2 Mass Law for Oblique incidence.....	40
2.1.3 Mass Law for Random incidence	40
2.1.4 Infinite panel Transmission Loss model.....	41
2.1.5 Coincidence Effect	43
2.1.6 Finite panel Transmission Loss model	44
2.1.6.1 Incident Power Expression.....	46
2.1.6.2 Radiated Power Expression.....	47
2.2 TL CALCULATIONS IN DISCRETE COORDINATES	51
2.2.1 Radiated Power in discrete coordinates	51
2.2.2 Incident Power in discrete coordinates	54
2.3 SOUND ABSORPTION.....	55
2.3.1 Equivalent absorption area	55
2.3.2 Energy balance in a room	55
2.3.3 Reverberation Time. Sabine’s formula	56
2.4 DAMPING	59
2.4.1 Structural damping	59
2.4.2 Acoustic damping	60
2.4.3 Damping treatments.....	60
3 TL EXPERIMENTAL MEASUREMENTS	64
3.1 TL MEASUREMENTS METHODS	64
3.1.1 Reverberation chambers	67
3.1.2 Schroeder Frequency	68
3.2 APPLICABLE STANDARDS.....	69
3.2.1 TL standard measurements with pressure-based method	70
3.2.2 TL standard measurements with intensity-based method	72
3.2.3 Single Number Ratings: Sound Transmission Class (STC).....	74
3.3 SMALL ACOUSTIC RESEARCH FACILITY (SMARF)	75
3.3.1 SMARF Validation.....	78
3.3.2 Geometrical dimensions and Standards prescription	78
3.3.3 Isolation from external noise sources	80
3.3.4 Flanking Transmission evaluation	81
3.3.5 Sound field diffuseness evaluation	82

3.3.6	Reverberation Time calculation.....	85
3.4	TEST PROCEDURE	89
3.5	EXPERIMENTAL RESULTS	92
4	NUMERICAL MODELS	98
4.1	FEM MODELS MESH SIZING	98
4.1.1	Isotropic plates.....	98
4.1.2	Orthotropic plates	100
4.2	FEM MODELLING APPROACHES FOR DAMPING TREATMENTS	101
4.3	STRUCTURAL-ACOUSTIC COUPLING	103
4.3.1	Structural domain equations	103
4.3.2	Fluid domain equations	104
4.3.3	Coupled domain equations	105
4.4	TRANSMISSION LOSS CALCULATIONS.....	107
5	UNCERTAINTY AND VARIABILITY	109
5.1	SOURCE OF UNCERTAINTIES IN COMPOSITE STRUCTURES	109
5.2	TAXONOMY OF NON-DETERMINISTIC TERMS	111
5.3	POSSIBILISTIC APPROACHES	113
5.3.1	Interval analysis.....	113
5.3.2	Fuzzy analysis	114
5.3.3	Information-gap analysis	114
5.4	PROBABILISTIC APPROACH.....	115
5.4.1	Monte Carlo and other Sampling Methods.....	118
5.4.2	Response Surface Approximation Method.....	123
5.4.2.1	Step 1: Analyze Structure at Chosen Values.....	125
5.4.2.1.1	Central Composite design	126
5.4.2.1.2	Box-Behnken design	127
5.4.2.1.3	Latin hypercube sampling method.....	128
5.4.2.2	Step 2: Develop regression equations.....	130
5.4.2.3	Step 3: Develop Response Variable PDF	130
5.4.2.4	Step 4: Evaluate Probability of Failure	130
5.4.3	Limit State Approximation Methods.....	131
5.4.3.1	Mean Value methods.....	131
5.4.3.2	Most Probable Point Methods	132
5.4.3.2.1	Step 1: Evaluate Probability of Failure	133
5.4.3.2.2	Step 2: Identify Most Probable Point	135
5.4.3.2.3	Step 3: Develop g-Function and Determine Failure Probability	136
5.5	RELIABILITY-BASED DESIGN OPTIMIZATION.....	141
6	APPLICATIONS	144
6.1	ANALYSIS USING NESSUS	144
6.1.1	Complex Modal Analysis results.....	146
6.1.2	Frequency Response Analysis results.....	146
6.1.3	Probabilistic FE Analysis	147
6.2	ANALYSIS USING OPTIMUS.....	151
6.2.1	Deterministic analysis.....	152
6.2.2	Probabilistic FE Analysis	154
6.2.3	Robust optimization results	157
6.3	ANALYSIS USING IN-HOUSE DEVELOPED CODE	158
6.3.1	TL numerical-experimental correlation.....	159
6.3.2	Effects of boundary conditions variability on predicted TL	161
6.3.3	Effects of material properties variability on predicted TL.....	165
	CONCLUSIONS.....	169
	REFERENCES AND BIBLIOGRAPHY	170
	APPENDIX A – PLATE FLEXURAL VIBRATIONS	178

Acknowledgements

Nowadays we live so fast that we often forget to look at the people we have around and that allow us to live a better life. These lines could be a good opportunity to think about this. Between six and seven years ago I was looking for an advisor for my Master thesis, I was a bit confused and I knocked on the door of some professors. Behind one of these doors there was a big man bright-eyed: at that time I didn't realize this could be a vital encounter. When I was back home, I told my girlfriend that I had met a professor with whom it was possible to have an interesting scientific discussion in the framework of a distressed interaction. She was an psychologist and suggested me to go back to that professor's office. It would be obvious to say that the guy, professor Marulo, changed my professional life, because he was my advisor for that thesis and he is now the advisor of my PhD thesis. He also changed something about my self confidence and vision of life, and this is, in my opinion, more important than to supervise my scientific work. I don't want to be wrong, so I thank him for everything. I've also to thank the psychologist, Maria, and not only for what she did that day. She still fills my personal life, with her smiles and her grumbles, I feel I would not be here without her. She is my wife, my best friend, my partner and the mother of my daughter, Giuliana Gaia, aka Pulce. She is so beautiful that I should thank Maria only for mother her. Last period of my PhD work has been done with the special support of the Pulce, that gave me new motivations and a lot of lovely, irresistible gazes and smiles. Tatata, Pulce. I want also to acknowledge my family of origin, for the love and the support they gave me and in particular, my mother, who taught me to look at the world with intellectual curiosity and my father, who taught me how much self-sacrifice is needed to be a good researcher. I want to remind here the backing and the fondness I'm receiving from the Suppa family, I appreciate it very much. Of course I can not forget, also because I meet them every day, my colleagues, aka Marulo boys, even if they are not all boys. Sergio, that is between a big brother and a co-supervisor, Franken, for his stinging irony, Carla, for her maternal love, Michele and Angelo, because it's a pleasure and a privilege to work with them. And, sometimes, it's also very funny. During last four years I was the co-advisor of about twenty master students, some of them became friends of mine. I want to acknowledge them all and, in particular, Katamar, who is Barbieri, Diego Turoturi, Aurelio and Paskà. Last but not least I want to remember my friends, Roberto, Andrea, Piermaria and Nello, with whom, some time ago, I was used to share emotions and expectations: this is not the only possible world.

List of Tables

Table 2.1 - TL measurements and prediction from an historical prospective	34
Table 3.1 - 95% Confidence Intervals amplitudes	71
Table 3.2 - Reference sound insulation contour for calculation of SNR.....	75
Table 3.3 - Main geometrical dimensions of the small TL facility	77
Table3.4 - Relation between minimum room volume and lower band of analysis	82
Table 3.5 - Maximum Standard Deviation of SPL	83
Table3.6 - 95% confidence limits of SPL	84
Table 3.7 - Test panels characteristics	92
Table 5.1 - Factors a and b for Central Composite designs.....	127
Table 5.2 - Box-Behnken experimental design matrix.....	127
Table 6.1 - Panel and coupled system natural modes.....	146
Table 6.2 - Coordinates of the nodes used for frequency response analysis.....	147
Table 6.3 - Correlation matrix	148
Table 6.4 - Statistically characterized material properties for the composite panel.....	154
Table 6.5 - Regression parameters for the two response model.....	157
Table 6.6 - RBDO results	158
Table 6.7 - Probabilistic analysis performed	163
Table 6.8 - Statistically characterized properties for the viscoelastic material	166

List of Figures

Figure 1.1- Sketch in Newton’s Principia of the passage of waves through a hole	17
Figure 1.2 - Sound Intensity physical interpretation	25
Figure 1.3 - One-third octave spectrum.....	27
Figure 1.4 - Equal loudness contours from ISO 226-2003.....	28
Figure 1.5 - Acoustic weighting curves.....	28
Figure 1.6 - Behaviour with frequency of different types of Random Noise.....	29
Figure 2.1 - Pressure Waves Normally Incident on a Panel.....	35
Figure 2.2 - TL behaviour with frequency	36
Figure 2.3 - Coincidence frequency as a function of plate thickness, h	37
Figure 2.4 - Oblique VS. Diffuse incidence on a surface.....	41
Figure 2.5 - Geometry on the incident side of the plate	42
Figure 2.6 - Definition of incident angles in a diffuse sound field.....	47
Figure 2.7 - Integration surface	48
Figure 2.8 - Image method	49
Figure 2.9 - Decay of sound in a room if the source is switched off at $t=1$ s.....	57
Figure 2.10 - Free layer damping treatment	60
Figure 2.11 - Constraining/Embedded layer damping treatment	61
Figure 2.12 - Variation of Complex Modulus with Temperature.....	63
Figure 3.1 - Airborne sound transmission from source room to receiving room	64
Figure 3.2 - STC calculation	75
Figure 3.3 - SMARF scheme-	75
Figure 3.4 - SMARF construction.....	76
Figure 3.5 - Details of SMARF construction	76
Figure 3.6 - SMARF locking system.....	76
Figure 3.7 - Knife-edge support	77
Figure 3.8 - SMARF septum cap.....	77
Figure 3.9 - Panel’s installation details	77
Figure 3.10 - Microphones mounting system.....	78
Figure 3.11 - Mode population in one-third octave bands	79
Figure 3.12 - External VS. internal ground noise levels	80
Figure 3.13 - lower SPL measured in the receiving room VS. background noise levels.....	80
Figure 3.14 - External VS. internal noise levels with external sound source.....	81
Figure 3.15 - SMARF measurements boundaries	82
Figure 3.16 - standard deviation of SPL in the source room.....	83
Figure 3.17 - 95% confidence interval of SPL in the source room	84
Figure 3.18 - Spatial distribution of the acoustic load on the panel at 100 Hz.....	85
Figure 3.19 - Spatial distribution of the acoustic load on the panel at 4000 Hz.....	85
Figure 3.20 - Time signal recorded for reverberation time calculations	86
Figure 3.21 - Calculated T_{60} as function of number of time blocks, NT	87
Figure 3.22 - One-third octave filter bank complying ANSI S1.1-1986.....	88
Figure 3.23 - Time signal filtered with 1000 Hz band filter.....	88
Figure 3.24 - Time decay at 1000 Hz.....	88
Figure 3.25 - Comparison between T_{60} estimates.....	89
Figure 3.26 - Correction factor for calculate TL from NR measurements.....	89
Figure 3.27 - Loudspeaker and microphones used for the acquisition.....	90

Figure 3.28 - Microphones positions in receiving room	90
Figure 3.29 - 95% confidence intervals on NR calculated on 42 (a) and 8 (b) positions.....	91
Figure 3.30 - 95% confidence intervals on NR in the range 250-10000 Hz	91
Figure 3.31 - Average NR of Aluminium panels	93
Figure 3.32 - Average NR of Composite panels	93
Figure 3.33 - Average Loss Factor @ 20°C	94
Figure 3.34 - NR of the three CFRP 7 samples coupon	94
Figure 3.35 - NR measured on CFRP 5 with a lapse of time of 8 months	95
Figure 3.36 - NR measured on CFRP 6 with a lapse of time of 8 months	95
Figure 3.37 - Average TL of Aluminium panels	96
Figure 3.38 - Average TL of Aluminium panels 1 and 2 mm thick with mass law	96
Figure 3.39 - Average TL of Aluminium panels 0.5 and 1.5 mm thick with mass law ..	97
Figure 4.1 - Wavelength curves for the composite panel modelled	100
Figure 4.2 - Wavelength curves to determine the panel's critical frequency	101
Figure 4.3 - Finite element models of viscoelastic damping	102
Figure 4.4 - Transmission Loss numerical results	107
Figure 4.5 - Composite panel modes (1,3)@1815.4 Hz and (2,3)@1850.7 Hz	108
Figure 4.6 - Transmission Loss numerical results in 1/3 octave bands	108
Figure 5.1 - Causes of uncertainties in the composite material	111
Figure 5.2 - Deterministic VS. Probabilistic design approach (from Schuëller, 2007) ..	116
Figure 5.3 - Two random variables JPDF	117
Figure 5.4 - Use of fitted CDF to estimate p_f	119
Figure 5.5 - Reliability Analysis by Monte Carlo Simulation	121
Figure 5.6 - Importance sampling function in X space	123
Figure 5.7 - RSM procedure using 3 levels of N design variables	125
Figure 5.8 - The example points of a Central Composite Circumscribed design	126
Figure 5.9 - Box-Behnken design cube	128
Figure 5.10 - CDF and PDF of a Latin hypercube sample for a Normal variable	129
Figure 5.11 - CDF and PDF of a Latin hypercube sample for a Uniform variable	129
Figure 5.12 - MPP based methods application procedure	133
Figure 5.13 - JPDF and MPP for Two Random Variables	134
Figure 5.14 - Geometry for computing the principal curvature	137
Figure 5.15 - FORM and SORM approximations of the limit state function	138
Figure 5.16 - Illustration of the AMV method	138
Figure 5.17 - AMV+ Iteration Algorithm for a Specified probability level	140
Figure 5.18 - First Order methods limits	141
Figure 5.19 - Deterministic VS. Reliability Based Optimum	142
Figure 6.1 - System FE model (a) and Frequency Responses at the chosen nodes (b) ..	147
Figure 6.2 - Sound Pressure versus ρ_t (a) and E_{fl} (b) close to a proper frequency	148
Figure 6.3 - Sound Pressure versus ρ_t (a) and E_{fl} (b) far from a proper frequency	149
Figure 6.4 - Average sound pressure in third octave bands, MC (a) VS. AMV+ (b) ..	149
Figure 6.5 - Relative errors between AMV+ and MC evaluations	150
Figure 6.6 - Mixed AMV+ and MC probabilistic frequency response	151
Figure 6.7 - Composite panel lay-up structure	152
Figure 6.8 - Composite panel FE model: lay-up details	152
Figure 6.9 - Finite Element model of the composite panel and the anechoic chamber ..	153
Figure 6.10 - Fringe acoustic plot of the acoustic pressure	153
Figure 6.11 - FRF Variability for the range of variation of the input parameters	155

Figure 6.12 - Sections of RM for the Maximum Acoustic Pressure	156
Figure 6.13 - Sections of RM for Max Acoustic Pressure's frequency of occurrence.	156
Figure 6.14 - Histograms of the Max Acoustic Pressure and of its freq. of occurr.....	157
Figure 6.15 - Results of the RBDO in the standard normal space.....	158
Figure 6.16 - Numerical VS. experimental TL in one-third octave bands	160
Figure 6.17 - Modal Analysis results, for the aluminium panel 2 mm thick.....	162
Figure 6.18 - Modal Analysis results, for the aluminium panel 1 mm thick.....	162
Figure 6.19 - FE model with springs along the edges	163
Figure 6.20 - TL results for the runs 1-4 (from the top left, clockwise).....	164
Figure 6.21 - Probabilistic results in terms of CDF, for the runs 1 (left) and 5 (right)	164
Figure 6.22 - TL behaviour with panel's thickness and damping variability.....	165
Figure 6.23 - Shear modulus and loss factor variability for a viscoelastic material.....	166
Figure 6.24 - TL behaviour with panel's thickness and damping variability.....	167
Figure 6.25 - CDF of the performance function, MV, AMV and AMV+.....	168
Figure 6.26 - CDF of the performance function calculated with MC method	168
Figure 6.27 - CDF of the performance function calculated with MC method	168
Figure A.0.1 - Force and Moments definition	178

Summary

In static as well as dynamic design it is important to allow for the fact that uncertainties can exist in the properties of the designed system and in the applied loading. Traditionally this has been faced through the use of factors of safety, which are developed and refined on the basis of experience and historical evidence. For systems where efficient design is of the utmost importance (for example the minimum weight design of an aircraft structure) it is possible that the traditional factors of safety may be overly conservative, so that optimal efficiency cannot be achieved. Furthermore, historical factors of safety are unlikely to be appropriate for new design concepts or new composite materials. The properties of composites, in fact, present a scattering much higher than metals, mainly due to manufacturing and assembling process. It follows that there is a need for a method (or methods) that can be applied objectively to a new design to yield information on the safety and reliability of the system without reliance on established factors of safety. The principal aim of the present work is to investigate capabilities offered by a probabilistic approach in the evaluation of vibroacoustic behaviour of aerospace composite damped panels. This is done interfacing probabilistic techniques with a numerical analysis of sound transmission loss. The numerical analysis, performed with a discrete coordinate approach, has been validated comparing simulation results with experimental ones measured in a dedicated facility, recently design and assembled, with the contribution of the author, at Department of Aerospace Engineering of the University of Naples “Federico II”.

Introduction

The higher specific strength and stiffness of reinforced composites versus metals as well as other attributes such as tailorability to load directionality, acoustic damping, and high fatigue endurance are attractive to manufacturers.

In the aerospace industry, the weight savings combined with improved structural efficiency are directly translated into increased payload, reduced acquisition and operating costs, and increased performance.

A pound of weight saved on a commercial aircraft is estimated from FAA to be worth \$100 to \$300 over the service life of the aircraft. This has led to large sections of transport airframes, entire empennages, and major portions of wing structure being made from composites. Composites on the new Boeing 787 Dreamliner will account for 50% of the aircraft's structural weight. By contrast, the Boeing 777 is 12% composites and 50% aluminium, and composites make up about 25% of the total airframe on the Airbus A380. The lower weight will allow the 787 to be 20% more fuel efficient than similarly sized airplanes.

Then, advanced composite materials offer measurable improvements in weight savings, maintainability, durability, and reliability.

Unfortunately, there are a number of performance factors that have limited their success.

A weak point of the design with composites, that will be analyzed in the present work is their poor acoustic performance. The elastic behaviour of a single ply of plywood, in fact, is different along and across the fibre direction. The bending stiffness of the ply changes gradually from the softest direction to the stiffest direction. Therefore, the bending wave phase velocity changes with direction. As a result, instead of a single critical frequency, there is a continuous range of critical frequencies, a critical region. Due to the high stiffness to weight ratio, this region is at lower frequencies than for metallic panels and, given the thickness used for aircraft skin panels, it occurs just where human hearing mechanism is more sensitive.

Nevertheless, unlike conventional metallic built-up structures, fibre-reinforced laminated structures are often constructed using adhesive joints with which there are fewer additional sources of energy dissipation associated than, for example, with bolted

or riveted joints. Thus, even if the intrinsic damping of composites is higher than metals, the overall damping performance of composite structures is generally lower.

This aspects are especially up-to-date because of the increasing importance of passenger comfort, related to the wider use of large, long-distance cruise aircraft. Nowadays comfort, that is connected to noise and vibration levels but also to air quality aspects, is one of the key factor that can ensure the success of a commercial airplane.

Thus far, composite design and treatment of unique performance factors have been handled in a traditional metals approach in the aircraft industry. This approach is characteristically deterministic in nature.

Composite properties suffer of high scattering, mainly related to composites manufacturing and assembling process. Using a deterministic approach, that seeks out and defines a worst case or an extreme value to meet, in the design of composite structures, can lead to the need to oversize structures and damping-soundproofing treatments in order to be able to satisfy required performances, penalizing in this way weight saving issues that drive the use of composite materials.

Probabilistic methods offer a different technology that can be used as a design tool, or, in a more conservative manner, as a risk analysis. The application of probabilistic methods opens up technical information not available in traditional approaches.

Probabilistic methods represent a technology that cannot be implemented without careful development. It is, however, a technology that is easily controllable. It may be used as an assessment of deterministic designs; it may be used to establish realistic criteria for deterministic designs; or it may be implemented as a preferred design approach. If used as the preferred design approach, probabilistic methods utilize a reliability target in lieu of factors-of-safety. Component dimensions, environmental factors, material properties, and external loads are design variables. They may be characterized with statistical models. The probabilistic approach utilizes the statistical characterization and attempts to provide a desired reliability in the design. The deterministic approach introduces conservatism by specifying a factor of safety to cover unknowns. The factor of safety is traditionally 1.5. The probabilistic approach depends on the statistical characterization of a variable to determine its magnitude and frequency. The amount of data (how well the variable is defined) influences its extreme values.

Application of a factor-of-safety to cover unknowns has a history of success. The danger in this approach is that the factor of safety may be too large, or in some cases, too small.

Advanced composite materials were introduced in the early 1960's and since that time have undergone significant development. Some obstacles appeared insurmountable, including susceptibility of material strength degradation to elevated temperature, absorbed moisture, impact damage, and hidden flaws or damage. The approach to accommodate these material strength reduction factors has been to develop worst case manufacturing and operational scenarios and assume their existence for the life of the part. These factors, which are in reality variables, are thereby treated as constants.

Composite part design is governed by compounded conservatism illustrated by the following criteria:

- Worst case loading x safety factor (1.5)
- Worst case temperature
- Worst case moisture
- Worst case damage, undetected
- Material allowables derived from conservative statistical criteria

The effect of combining these conservative structural criteria is to produce inefficient products. Probabilistic methods offer an alternative to compound conservatism. They quantify the degree of safety and permit the designer to discover the risk drivers.

In order to conduct a probabilistic design, the following parameters should be characterized as random variables:

1. Material mechanical properties
2. External loads anticipated during the life of the article
3. Manufacturing processes and their effects
4. Environmental effects
5. Environmental history during operational usage
6. Flaw and/or damage locations, severity, probability of occurrence and effect on strength
7. Predictive Accuracy

Adopting specific structural criteria should not be done without a reason. The current criteria has its origins in metals technology. The goal of probabilistic design is to make reliability the foundation of composite design criteria.

The principal aim of the present work is to investigate capabilities offered by a probabilistic approach in the evaluation of vibroacoustic behaviour of aerospace composite panels. This is done interfacing well assessed probabilistic techniques with a numerical analysis of sound transmission loss. The numerical analysis, performed with a discrete coordinate approach, has been validated comparing numerical results with experimental ones measured in a dedicated facility, recently design and assembled, with the contribution of the author, at Department of Aerospace Engineering of the University of Naples “Federico II”.

In Chapter 1 the fundamentals of the sound and the definition of the quantities used in the noise control field are defined and briefly accounted.

Chapter 2 deals with sound transmission loss prediction techniques, whose mathematical expressions are derived for infinite as well for finite panels. The discrete coordinate approach, applied for the calculation carried out in the following chapters, is presented together with a discussion about sound absorption and damping mechanisms.

Chapter 3 discusses the standards in force for transmission loss measurements and shows the different phases of design and validation of the Small Acoustic Research Facility (SMARF). Furthermore, the test procedure and results achieved from a test campaign on metallic and composite panels are presented. Some of the composite panel tested have a layer of a viscoelastic material co-cured. The effectiveness of such configuration, that seems to be a viable solution in increasing the damping of composite structures with little reduction in stiffness and strength to increase the damping, is argued.

Chapter 4 examines the theories on which the numerical models developed are founded. The mesh sizing problem for isotropic and orthotropic flat panels is tackled, in the latter case following a spectral method to calculate the dispersion properties of the structural waves. The FE approaches for embedded damping treatments are briefly outlined and reviewed. The problem of the structural-acoustic coupling is presented highlighting the governing equations for separate structural and fluid domain and for the coupled one. Finally, transmission loss results obtained from numerical simulations are showed.

Chapter 5 is devoted to the discussion of concepts of uncertainty and variability. A review of possibilistic and probabilistic approaches is given. Benefits and drawbacks of sampling methods, such as Monte Carlo and variance reduction techniques, Response Surface Approximation method and Limit State Approximation methods are explained, together with a definition of the algorithms that implement these methods. At the end of the Chapter, an introduction to the reliability based optimization procedure is provided. Chapter 6 covers the results of probabilistic finite elements applications performed using commercial codes, as NESSUS and OPTIMUS and an in-house developed code. The reasons for development of this code are pointed out together with encountered difficulties and limits in applying available codes to vibroacoustic typical test cases. The conclusions drawn from this research are given in the devoted section.

1 Physical Principles of Sound

The speculation that sound is a wave phenomenon grew out of observations of water waves. The rudimentary notion of a wave is an oscillatory disturbance that moves away from some source and transports no discernible amount of matter over large distances of propagation. The possibility that sound exhibits analogous behaviour was emphasized, for example, by the Greek philosopher Chrysippus (c. 240 B.C.), by the Roman architect and engineer Vitruvius (c. 25 B.C.), and by the Roman philosopher Boethius (A.D. 480-524). The wave interpretation was also consistent with Aristotle's (384-322 B.C.) statement to the effect that air motion is generated by a source, "thrusting forward in like manner the adjoining air, to that the sound travels unaltered in quality as far as the disturbance of the air manages to reach".

A pertinent experimental result, inferred with reasonable conclusiveness by the early seventeenth century, with antecedents dating back to Pythagoras (c. 550 B.C.) and perhaps further, is that the air motion generated by a vibrating body sounding a single musical note is also vibratory and of the same frequency as the body. The history of this is intertwined with the development of the laws for the natural frequencies of vibrating strings and of the physical interpretation of musical consonances. Principal roles were played by Marin Mersenne (1588-1648), a French natural philosopher often referred to as the "father of acoustics," and by Galileo Galilei (1564-1642), whose *Mathematical Discourses Concerning Two New Sciences* (1638) contained the most lucid statement and discussion given up until then of the frequency equivalence.

Mersenne's description in his *Harmonic Universelle* (1636) of the first absolute determination of the frequency of an audible tone (at 84 Hz) implies that he already demonstrated that the absolute-frequency ratio of two vibrating strings, radiating a musical tone and its octave, is as 1 : 2. The perceived harmony (consonance) of two such notes would be explained if the ratio of the air oscillation frequencies is also 1 : 2, which in turn is consistent with the source-air-motion-frequency-equivalence hypothesis.

The analogy with water waves was strengthened by the belief that air motion associated with musical sounds is oscillatory and by the observation that sound travels with a finite speed. Another matter of common knowledge was that sound bends around corners, which suggested diffraction, a phenomenon often observed in water waves.

Also, Robert Boyle's (1640) classic experiment on the sound radiation by a ticking watch in a partially evacuated glass vessel provided evidence that air is necessary, either for the production or transmission of sound.

The wave viewpoint was not unanimous, however. Gassendi (a contemporary of Mersenne and Galileo), for example, argued that sound is due to a stream of "atoms" emitted by the sounding body; velocity of sound is the speed of atoms; frequency is number emitted per unit time.

The apparent conflict between ray and wave theories played a major role in the history of the sister science optics, but the theory of sound developed almost from its beginning as a wave theory. When ray concepts were used to explain acoustic phenomena, as was done, for example, by Reynolds and Rayleigh, in the nineteenth century, they were regarded, either implicitly or explicitly, as mathematical approximations to a then well-developed wave theory; the successful incorporation of geometrical optics into a more comprehensive wave theory had demonstrated that viable approximate models of complicated wave phenomena could be expressed in terms of ray concepts. (This recognition has strongly influenced modern developments in architectural acoustics, underwater acoustics, and noise control.)

The mathematical theory of sound propagation began with Isaac Newton (1642-1727), whose Principia (1686) included a mechanical interpretation of sound as being "pressure" pulses transmitted through neighbouring fluid particles. Accompanying diagrams (Figure 1.1) illustrated the diverging of wave fronts after passage through a slit. The source is in A, the hole is described by points B and C, the points de, fg, etc. describe the "tops of several waves, divides from each other by as many intermediate valleys or hollows".

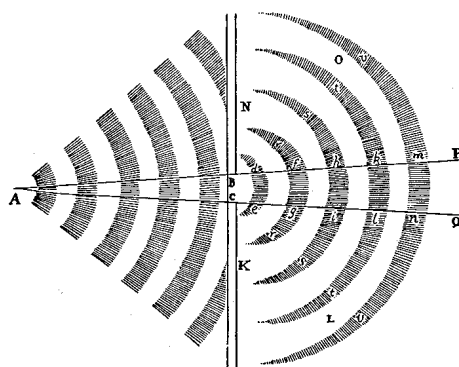


Figure 1.1- Sketch in Newton's Principia of the passage of waves through a hole

The mathematical analysis was limited to waves of constant frequency, employed a number of circuitous devices and approximations, and suffered from an incomplete definition of terminology and concepts. It was universally acknowledged by his successors as difficult to decipher, but, once deciphered, it is recognizable as a development consistent with more modern treatments, even if Newton's result was underestimating actual speed of sound of about 16%.

Substantial progress toward the development of a viable theory of sound propagation resting on firmer mathematical and physical concepts was made during the eighteenth century by Euler (1707-1783), Lagrange (1736-1813), and d'Alembert (1717-1783). During this era, continuum physics, or field theory, began to receive a definite mathematical structure. The wave equation emerged in a number of contexts, including the propagation of sound in air. The theory ultimately proposed for sound in the eighteenth century was incomplete from many standpoints, but modern theories of today can be regarded for the most part as refinements of that developed by Euler and his contemporaries.

1.1 Sound Waves

Sound waves are compressional oscillatory disturbances that propagate in a fluid. The waves involve molecules of the fluid moving back and forth in the direction of propagation (with no net flow), accompanied by changes in the pressure, density and temperature. The sound pressure, that is, the difference between the instantaneous value of the total pressure and the static pressure, is the quantity that can be heard. It is also much easier to measure the sound pressure than the other quantities. It has to be noted that sound waves are longitudinal waves, unlike bending waves on a beam or waves on a stretched string, which are transversal waves in which the particles move back and forth in a direction perpendicular to the direction of propagation.

The pressure changes associated with a sound wave can be very small if compared with ambient pressure: the human hear can perceive as sound pressure variation in the range ($20 \mu Pa$, $10^4 Pa$), whereas the ambient pressure at sea level is about $1 atm = 1.013 \cdot 10^5 Pa$.

A mathematical description of the wave motion in a fluid can be obtained by combining equations that express the facts that:

- mass is conserved

- the local longitudinal force caused by a difference in the local pressure is balanced by the inertia of the medium
- sound is very nearly an adiabatic phenomenon, that is, there is no flow of heat.

The observation that most acoustic phenomena involve perturbations that are several orders of magnitude smaller than the equilibrium values of the medium makes it possible to simplify the mathematical description by neglecting higher-order terms.

Thus, it is useful to describe pressure, density and particle velocity as constituted by an “ambient” term, denoted by a subscript “0” plus and additional one related to the fluctuation around the ambient value, denoted by a superscript “f”.

The pressure, density and particle velocity at a point in the fluid can then be expressed as:

$$\begin{aligned}
 p &= p_0 + p^f \\
 \rho &= \rho_0 + \rho^f \\
 v &= v^f
 \end{aligned}
 \tag{1.1}$$

where $v_0=0$ because there is no ambient fluid flow.

The equation of continuity or conservation of the mass is:

$$\frac{\partial \rho}{\partial t} + \nabla \cdot (\rho v) = 0
 \tag{1.2}$$

that, in the linearized form, appears to be

$$\frac{\partial \rho^f}{\partial t} + \rho_0 \nabla v^f = 0
 \tag{1.3}$$

The Euler’s equation of motion (conservation of motion quantity) is:

$$\rho \frac{Dv}{Dt} + \nabla p = 0 \text{ where } \frac{D}{Dt} = \frac{\partial}{\partial t} + v \cdot \nabla
 \tag{1.4}$$

this equation, after the linearization becomes:

$$\rho_0 \frac{\partial v^f}{\partial t} + \nabla p^f = 0
 \tag{1.5}$$

The equation of state, under the assumption that the sound propagation is an adiabatic process, is:

$$p \rho^{-\gamma} = \text{const.}
 \tag{1.6}$$

The linearization of the equation of state leads to the relation:

$$p^f \approx \left(\frac{\gamma P_0}{\rho_0} \right) \rho^f = c^2 \rho^f \quad (1.7)$$

where c is the speed of sound in the elastic medium. Differentiating the previous equation it results that:

$$\frac{\partial^2 p^f}{\partial t^2} = c^2 \frac{\partial^2 \rho^f}{\partial t^2} \quad (1.8)$$

The combination of these three equation linearized gives the wave equation that is the basic partial differential equation governing the spatial and time dependence of the acoustic field.

$$\nabla^2 p - \frac{1}{c^2} \frac{\partial^2 p}{\partial t^2} = 0 \quad (1.9)$$

It has to be noted that for sake of simplicity in the previous equation it has been dropped the superscript “ f ” in the notation, so that p is the fluctuating component of the pressure (and v will be the acoustic particle velocity).

1.1.1 Plane sound waves

A disturbance at great distance from the source is approximated as a plane wave. This approximation is founded on the fact that, when considering a limited area at a distance far from a source of sound in free space, the curvature of the spherical wavefronts is negligible and the waves can be regarded as locally plane. Each acoustic variable has constant amplitude and phase on any plane perpendicular to the direction of propagation.

There is no y or z dependence, so that $\frac{\partial}{\partial y} = \frac{\partial}{\partial z} = 0$ and the equation (1.9) can be expressed in one-dimensional form as:

$$\frac{\partial^2 p}{\partial x^2} - \frac{1}{c^2} \frac{\partial^2 p}{\partial t^2} = 0 \quad (1.10)$$

The general solution of the previous equation is:

$$p(x, t) = f_1(ct - x) + f_2(ct + x) \quad (1.11)$$

The first term of expression (1.11) represents a wave that propagates undistorted and unattenuated in the x -direction with constant speed, c , whereas the second term represents a similar wave travelling in the opposite direction.

The special case of a harmonic plane progressive wave is of great importance. Harmonic waves are generated by sinusoidal sources, for example a loudspeaker driven with a pure tone. A harmonic plane wave propagating in the x -direction can be written as:

$$p(x, t) = p_1 \sin \left[\frac{\omega}{c}(ct - x) + \varphi \right] = p_1 \sin(\omega t - kx + \varphi) \quad (1.12)$$

where $\omega = 2\pi f$ is the angular (or circular) frequency, [rad/s], k , defined as $k = \omega/c$, is the propagation constant or acoustic wavenumber, [m^{-1}]. The quantity p_1 is known as the amplitude of the wave, and φ is a phase angle. At any position in this sound field the sound pressure varies sinusoidally with the angular frequency ω , and at any fixed time the sound pressure varies sinusoidally with x . The spatial period is given by:

$$\lambda = \frac{c}{f} = \frac{2\pi c}{\omega} = \frac{2\pi}{k} \quad (1.13)$$

λ is the wavelength and can be thought as the distance between two peaks in the propagating sound wave.

Sounds are often studied in the frequency domain. This leads to the introduction of the complex exponential representation, where the sound pressure is written as a complex function of the position multiplied with a complex exponential. The former function takes account of the amplitude and phase, and the latter describes the time dependence.

Thus, at any given position the sound pressure can be written as a complex function:

$$\hat{p} = Ae^{j\omega t} = |A|e^{j\varphi}e^{j\omega t} = |A|e^{j(\omega t + \varphi)} \quad (1.14)$$

(where φ is the phase of the complex amplitude A), and the real, physical sound pressure is the real part of the complex pressure:

$$p = \text{Re}\{\hat{p}\} = \text{Re}\{|A|e^{j(\omega t + \varphi)}\} = |A|\cos(\omega t + \varphi) \quad (1.15)$$

Since the entire sound field varies as $e^{j\omega t}$, the operator $\partial/\partial t$ can be replaced by $j\omega$ (because the derivative of $e^{j\omega t}$ with respect to time is $j\omega e^{j\omega t}$), and the operator $\partial^2/\partial t^2$ can be replaced by $-\omega^2$.

It follows that Euler's equation of motion (1.5) can now be rewritten as:

$$j\omega\rho_0\hat{v} + \nabla\hat{p} = 0 \quad (1.16)$$

and the wave equation can be expressed in the simplified form:

$$\nabla^2 \hat{p} + k^2 \hat{p} = 0 \quad (1.17)$$

which is known as the Helmholtz equation.

Written with complex notation the equation for a plane wave that propagates in the x -direction becomes:

$$\hat{p} = p_i e^{j(\omega t - kx)} \quad (1.18)$$

Equation (1.16) shows that the particle velocity is proportional to the gradient of the pressure. It follows that the particle velocity in a plane propagating wave can be expressed in the form:

$$\hat{u} = -\frac{1}{j\omega\rho_0} \frac{\partial \hat{p}}{\partial x} = \frac{k}{\omega\rho_0} p_i e^{j(\omega t - kx)} = \frac{P_i}{\rho_0 c} e^{j(\omega t - kx)} = \frac{\hat{p}}{\rho_0 c} \quad (1.19)$$

where u is the x -component of the particle velocity.

From the previous relation descends that the sound pressure and the particle velocity are in phase in a plane propagating wave.

The ratio of the sound pressure to the particle velocity is called characteristic impedance of the medium:

$$\hat{Z} = \frac{\hat{p}}{\hat{u}} = \rho_0 c \quad (1.20)$$

1.1.2 Spherical sound waves

The wave equation can be expressed in other coordinate systems than the Cartesian. If sound is generated by a source in an environment without reflections (which is usually referred to as a free field), it will generally be more useful to express the wave equation in a spherical coordinate system (r, θ, φ) . The resulting equation is more complicated than equation (1.9). However, if the source under study is spherically symmetric there can be no angular dependence, and the equation becomes quite simple:

$$\frac{\partial^2 p}{\partial r^2} + \frac{2}{r} \frac{\partial p}{\partial r} - \frac{1}{c^2} \frac{\partial^2 p}{\partial t^2} = 0 \quad (1.21)$$

that, if rewritten in the form:

$$\frac{\partial^2}{\partial r^2}(rp) - \frac{1}{c^2} \frac{\partial^2(rp)}{\partial t^2} = 0 \quad (1.22)$$

is identical to the one-dimensional wave equation (1.10) with rp instead of p . It follows that the general solution of the (1.21) is:

$$rp(r, t) = f_1(ct - r) + f_2(ct + r) \quad (1.23)$$

that is equivalent to the following:

$$p(r, t) = \frac{1}{r} [f_1(ct - r) + f_2(ct + r)] \quad (1.24)$$

The first term is a wave that travels outwards, away from the source. It is worth to notice that the shape of the wave is preserved. However, the sound pressure is seen to decrease in inverse proportion to the distance. This is called the “inverse distance law” and express the fact that in a free field the pressure level halves if doubling the distance from the sound source. The second term represents a converging wave, that is, a spherical wave travelling inwards. In principle such a wave could be generated by a reflecting spherical surface centred at the source, but that is a rare phenomenon and the second term is usually neglected.

An harmonic spherical wave is a solution to the Helmholtz equation:

$$\frac{\partial^2}{\partial r^2} (r\hat{p}) + k^2 r\hat{p} = 0 \quad (1.25)$$

Expressed in the complex notation the diverging wave can be written as:

$$\hat{p} = A \frac{e^{j(\omega t - kr)}}{r} \quad (1.26)$$

1.2 Acoustic measurements

The most important measure of sound amplitude is the effective sound pressure p_{rms} , defined as:

$$p_{rms} = \left(\lim_{T \rightarrow \infty} \frac{1}{T} \int_0^T p^2(t) dt \right)^{\frac{1}{2}} \quad (1.27)$$

where *rms* stands for root mean square and is a measure of the energy in the acoustic wave.

For a pure tone (sine wave) over a period $T = 2\pi/\omega$, it results $p_{rms} = p/\sqrt{2}$ where *p* is called peak pressure value.

The human ear can perceive sounds over a very large range of sound pressure. Therefore, sound pressure is commonly expressed in a logarithmic scale, rather than a linear scale, using dB as unit. The reference used, p_0 is 20 μ Pa RMS, that corresponds to the threshold of the human hearing at 1 kHz.

The definition of Sound Pressure Level (SPL) is then:

$$SPL[dB] = 20 \log_{10} \left(\frac{p_{rms}}{p_0} \right) \quad (1.28)$$

A doubling of the sound amplitude corresponds to an increase of 6 dB of the SPL.

Beyond sound pressure, there are some other quantities that characterize a sound field: sources of sound emit sound power, and sound fields are also energy fields in which potential and kinetic energies are generated, transmitted and dissipated.

It is apparent that the radiated sound power is a negligible part of the energy conversion of almost any source. However, energy considerations are nevertheless of great practical importance in acoustics. The usefulness is due to the fact that a statistical approach, where the energy of the sound field is considered, turns out to give very useful approximations in room acoustics and in noise control. This approach, known as Statistical Energy Analysis, SEA, predicts the flow of energy between the various components of a multi-assembly system and have found large application for vibroacoustic problems in the high frequency range.

1.2.1 The energy in a sound field

It can be shown that the instantaneous potential energy density in a sound field (the potential sound energy per unit volume) is given by the expression:

$$w_{pot}(t) = \frac{p^2(t)}{2\rho_0 c^2} \quad (1.29)$$

This quantity describes the energy stored per unit volume of the medium because of the compression or rarefaction; the phenomenon is analogous to the potential energy stored in a compressed or elongated spring, and the derivation is similar.

The instantaneous kinetic energy density in a sound field (the kinetic energy per unit volume) is:

$$w_{kin}(t) = \frac{1}{2} \rho_0 v^2(t) \quad (1.30)$$

This quantity describes the energy per unit volume represented by the mass of the particles of the medium moving with the velocity v . This corresponds to the kinetic energy of a moving mass, and the derivation is similar.

The instantaneous sound intensity $I(t)$ is the product of the instantaneous sound pressure and the instantaneous particle velocity

$$I(t) = p(t) \cdot v(t) \quad (1.31)$$

This quantity, which is a vector, expresses the magnitude and direction of the instantaneous flow of sound energy per unit area, or the work done by the sound wave per unit area of an imaginary surface perpendicular to the vector.

In practice the time-averaged energy densities:

$$w_{pot} = \frac{p_{rms}^2}{2\rho_0 c^2} \quad (1.32)$$

and

$$w_{kin} = \frac{1}{2} \rho_0 v_{rms}^2 \quad (1.33)$$

are more important than the instantaneous quantities, and so the time-averaged sound intensity (which is usually referred to just as the ‘sound intensity’):

$$\bar{I}(t) = \bar{p}(t) \cdot \bar{v}(t) \quad (1.34)$$

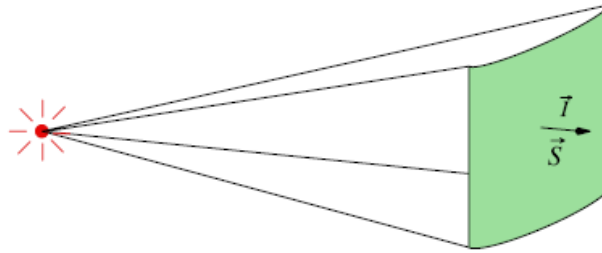


Figure 1.2 – Sound Intensity physical interpretation

It can be shown that the integral of the normal component of the sound intensity over a closed surface S is zero:

$$\int_S I \cdot dS = 0 \quad (1.35)$$

in any sound field unless there is generation or dissipation of sound power within the surface S . If the surface encloses a source, the integral equals the radiated sound power of the source, W_s , irrespective of the presence of other sources of noise outside the surface:

$$\int_S I \cdot dS = W_s \quad (1.36)$$

If complex notation is used, the sound intensity can be written as:

$$I = \text{Re}\{\bar{p} \cdot \bar{v}^*\} \quad (1.37)$$

where the apex “*” indicates the complex conjugate.

From the previous equation and using the (1.19), it descends that for a plane propagating wave, the sound intensity can be expressed as:

$$I = \frac{1}{2} \operatorname{Re} \left\{ \widehat{p} \cdot \frac{\widehat{p}^*}{\rho_0 c} \right\} = \frac{|\widehat{p}|^2}{2\rho_0 c} = \frac{p_{rms}^2}{2\rho_0 c} \quad (1.38)$$

However, it should be emphasised that in the general case the relation (1.38) is not valid, and one will have to measure both the sound pressure and the particle velocity simultaneously and time integrate the instantaneous product in order to measure the sound intensity.

Equation (1.36) implies that one can determine the sound power radiated by a source by integrating the normal component of the sound intensity over a surface that encloses the source.

That is the sound intensity method of measuring sound power that will be introduced later as measurement technique that can be used in transmission loss facilities to determine power radiated by a vibrating surface.

1.3 Octave frequency bands

The human hearing mechanism is more sensitive to frequency ratios rather than actual frequencies. The frequency of a sound determines its pitch as perceived by a listener, and a frequency ratio of two is a perceived pitch change of one octave, no matter what the actual frequencies are. For instance if a sound of 100 Hz frequency is raised to 200 Hz, its pitch will rise one octave, and a sound of 1000 Hz, when raised to 2000 Hz, will also rise one octave in pitch. This fact is so precisely true over a wide frequency range that it is convenient to define the octave as a frequency ratio of two, even though the octave itself is really a subjective measure of a sound pitch change.

This phenomenon can be summarized by saying that the pitch perception of the ear is proportional to the logarithm of frequency rather than to frequency itself. Therefore, it makes sense to express the frequency axis of acoustic spectra on a log frequency axis. The octave is such an important frequency interval to the ear that so-called octave band analysis has been defined as a standard for acoustic analysis. Its bandwidth follows reasonably well with the critical bandwidth of the human ear throughout the audible frequency range. Each octave band has a bandwidth equal to about 70% of its centre frequency.

This type of spectrum is called constant percentage bandwidth because each frequency band has a width that is a constant percentage of its centre frequency. In other words, the analysis bands become wider in proportion to their centre frequencies. It can

be argued that the frequency resolution in octave band analysis is too poor to be of much use, especially in analyzing structure borne sound, but it is possible to define constant percentage band analysis with frequency bands of narrower width. A common example of this is the one-third-octave spectrum, whose filter bandwidths are about 27% of their centre frequencies. Three one-third octave bands span one octave, so the resolution of such a spectrum is three times better than the octave band spectrum. The Figure 1.3 shows a typical one-third octave band spectrum where the ANSI S1.6 standard centre frequencies are used.

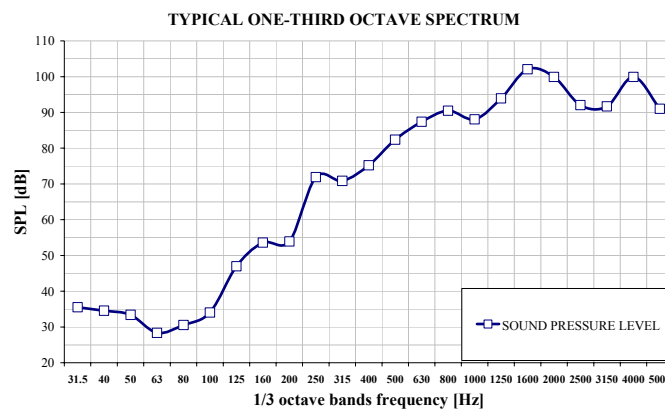


Figure 1.3 - One-third octave spectrum

1.4 Sound Levels perception

From SPL definition, as already observed, it descends that a doubling of the sound amplitude corresponds to an increase of 6 dB of the SPL.

However, this will not result in a doubling of the perceived level of sound. Although obviously related to the SPL of the sound, in fact, the perception of loudness is also highly dependent on the frequency.

The Loudness is expressed in Phon or in Sone, Sone is the linear unit derived from Phon: $S = 2^{(P-40)/10}$. An increase by 10 Phon (or a doubling in Sone) is experienced as a doubling in loudness.

Several tests, using pure tones which were adjusted in amplitude such that they were perceived at the same loudness as a 1 kHz tone, lead to the concept of Equal Loudness Contours. These curves, originally introduced by Fletcher and Munson in 1933, have been standardized in ISO 226-1961, based on the work of Robinson and Dadson (1956). Recently, new equal-loudness contours, standardized in ISO 226-2003 and illustrated in the following Figure 1.4, have been derived in order to take into account discrepancies between classic iso-loudness contours and data obtained in later studies. In the low

frequency range, these differences are nearly as high as 15 dB. Such marked deviations are not only of theoretical importance, they also have practical implications.

These equal loudness curves, in fact, led to the development of the well-known acoustic weighting curves (A, B, C and D), see Figure 1.5. For example, the current A-weighting for the sound level meter is based on the equal-loudness contour at 40 phons

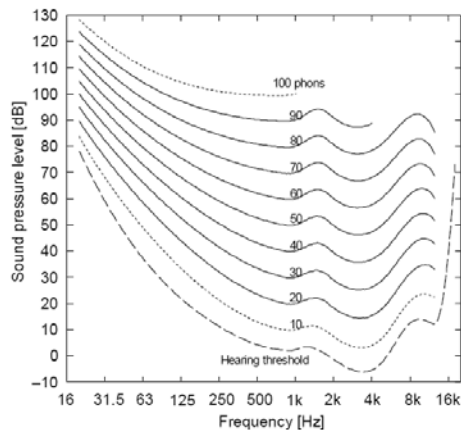


Figure 1.4 – Equal loudness contours from ISO 226-2003

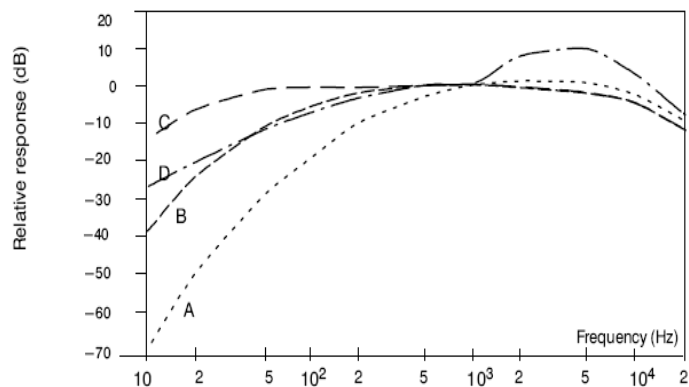


Figure 1.5 - Acoustic weighting curves

The idea behind these weighting curves is that by applying these weightings on the signals before calculating the SPL level, one would compensate for the frequency-dependency of the hearing sensitivity, yielding a sound pressure level that is more closely related to the perceived Loudness. As the shape of Equal Loudness Contours changes with the loudness level, a number of filters are used, each covering a certain range of sound level. For instance A-weighting (dBA) is used to compensate at low SPL levels (40 dB), B for middle SPL levels (70 dB) and C-weighting for high level SPL

levels (100 dB). D-weighting has been designed and standardized for aircraft noise measurements that are characterized to have very high SPL values.

Although proven to be successful in a large range of applications, the estimation of Loudness based on the acoustic weighting of SPL levels has a number of severe limitations. Firstly, it is based on curves that were obtained in experiments using pure tones. These results can not be used to estimate the loudness of, for instance, broad-band noise, or of sound consisting of both tonal and broad-band noise components. Furthermore, they do not take into account the effects of spectral masking.

1.5 White and Pink noise

White noise is analogous to white light in that the energy of both is distributed uniformly throughout the spectrum. In other words, white noise energy exhibits a flat distribution of energy with frequency, see curve “A” in Figure 1.6.

White light sent through a prism is broken down into a range of colours. The red colour is associated with the longer wavelengths of light, that is, light in the lower frequency region. Pink noise is noise having higher energy in the low frequencies. In fact, pink noise has come to be identified specifically as noise exhibiting high energy in the low-frequency region, with a specific downward slope of 3 dB per octave (curve “C” in Figure 1.6).

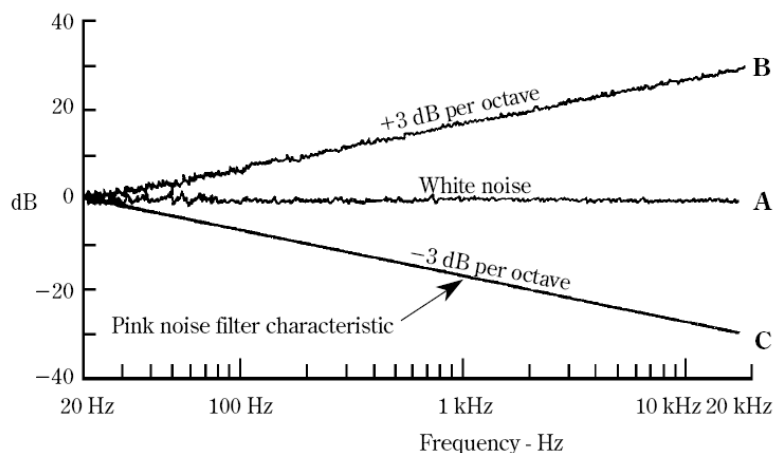


Figure 1.6 – Behaviour with frequency of different types of Random Noise

These two colourful terms arose because there are two types of spectrum analyzers in common use. One is the constant bandwidth analyzer, which has a pass band of fixed width as it is tuned throughout the spectrum. If white noise with its flat spectrum were measured with a constant-bandwidth analyzer, another flat spectrum would result because the fixed bandwidth would measure a constant energy throughout the band.

Another very popular and convenient spectrum analyzer is the constant percentage bandwidth analyzer. In this instrument the bandwidth changes with frequency. An example of this is the one-third octave analyzer, At 100 Hz the bandwidth of the one-third octave analyzer is only 23 Hz but at 10 kHz the bandwidth is 2,300 Hz. Obviously, it intercepts much greater noise energy in a one-third octave band centred at 10 kHz than one centred at 100 Hz.

Measuring white noise with a constant-percentage analyzer would give an upward-sloping result with a slope of 3 dB/octave, as shown in the curve “B” in Figure 1.6.

In audio-frequency measurements, the desired characteristic of many instruments, rooms, etc. is a flat response throughout the frequency range. Assume that the system to be measured has a characteristic almost flat with frequency. If this system is excited with white noise and measured with the very convenient constant-percentage analyzer, the result would have an upward slope of 3 dB/octave. It would be far more desirable if the measured result would be close to flat so that deviations from flatness would be very apparent. This can be accomplished by using a noise with a downward slope of 3 dB/octave. Such a noise is the pink noise. A close-to-flat system (amplifier, room) excited with this pink noise would yield a close-to-flat response, which would make deviations from flatness very easy to be appreciated.

1.6 Sound fields

Measured sound pressure in a given field point depends, other than from sound power of the generating source and from distance between source and point itself, from environmental conditions.

In fact, the sound power is the cause of the acoustic phenomenon, whereas sound pressure is its effect. The part of the propagation medium in which there are effect of one or more acoustic sources is called sound field.

On the base of source and propagation medium characteristics, it is possible to have different sound fields. A first distinction is between free and reverberant field.

In a free field environment, the sound produced by the source can propagate without obstacles. The mean-square sound pressure level varies inversely as the square of the distance from the source. The general rule of thumb is that, under ideal conditions (no reflecting surfaces or other background sound or interference), a sound level drops 6 dB for every doubling of the distance from the source.

The free field is an active field because all energy radiated by the source can make work by inducing oscillation in medium particles. In an active field, in fact, particle velocity and sound pressure are in phase and all the acoustic energy is transmitted away from the source. For laboratory measurements purposes, the free field is usually approximated in so called anechoic chambers that are special acoustic chambers whose walls are treated with sound absorbing materials, such that walls reflections are negligible.

In a reverberant, also called diffuse, field, the sound pressure in a generic position is due to a number of reflections on obstacles and walls of the wave generated from the source. At any given point in the diffuse field, sound will arrive from all angles in a uniform manner.

In a reverberant field can be distinguished three main areas: direct, mixed and downright diffuse field.

In the direct field, that is the part closer to the source, sound pressure behaviour is quite similar to that of free field and inverse law rules.

In a properly diffuse field, primary sound waves radiated from the source are reflected and refracted from obstacles. Thus, in a generic field position, sound pressure depends by the interactions undergone from the waves. The mixed field is the transition zone between direct and diffuse field.

The diffuse field is approximated in acoustic reverberant chambers where all the walls are reflecting the sound waves without absorption. The sound pressure level at any point will be an average value due to the reflections.

2 Transmission Loss

Much of the interest in the study of transmission loss through panels began in the early 1900's. The first theoretical formulation to determine the sound transmission loss of a partition between two rooms was presented in the 1920's by Davis and Buckingham that defined transmission loss as the \log_{10} of the ratio of transmitted to incident pressure waves on a surface.

Several more studies were conducted over the next twenty five years which further developed the transmission loss theory. These studies included theories of infinite panel dimensions which eliminated the accounting of the boundary constraints. The most referred to prediction model for thin infinite panels was presented by Cremer in 1942. This theory included the effect of bending stiffness and the sound incidence angle θ .

Further investigation during this time lead to the development of theories for the transmission of sound through partitions which incorporated the now well known mass law term of the panel. This accounting of the mass effect of the panel was developed by Beranek (1949).

London advanced the theory one step further by including the mechanical impedance of the panel (London, 1950). This is one of the first accounts of incorporating the vibration of the panel in predicting the transmission loss. Since then, there has been more development in the details of transmission loss theory. In early sixties Smith Jr. and Maidanik studied respectively the sound radiation of structural modes and the acoustic behaviour of ribbed panels from a statistical point of view, and Lyon evaluated the Noise Reduction produced by a rigid enclosure with an elastic wall in a broad frequency range, highlighting the sound transmission relation with panel's and cavity's modes.

In 1966, White and Powell presented a mode-coupling model for resonant transmission of a finite rectangular panel. According to Bhattacharya and Guy (1971), the most essential limitation of the infinite panel model was that freely propagating flexural waves can not exist in a finite plate. The wavenumbers of the plate are defined by the dimensions and the boundary conditions of the panel. Therefore, the position of the coincidence frequency is independent of the sound incidence angle. Ordubadi and Lyon in 1979 discussed the effect of orthotropy on sound transmission of laminated

panels, starting from the observation of experimental results where the sound insulation drop typical of homogeneous panes at the coincidence frequency was not present. A well established formulation for prediction of the noise transmission characteristics of isotropic and orthotropic rectangular panels can be found in the work of Roussos (1985)

More recently, the effects of cavity modes have also been incorporated into the science of predicting sound transmission (Oldham et al., 1991). In this paper the authors suggested that the fundamental mode of a panel is the only mode that would effectively radiate noise.

With the advent of digital computers, which are capable of multiple computations, the ability to simulate acoustic behaviour through mathematical analysis has become more successful and subsequently more useful. Methods like mode simulation analysis, statistical energy analysis, finite element analysis and boundary element analysis have become some of the more popular techniques used in recent years (Crocker, 1994).

As it can be seen, studies regarding the prediction of panel's transmission loss, power radiated from vibrating structures and radiation efficiency cover more than 80 years and were not developed in an homogeneous manner, even because performed in almost independent way in different countries and with substantially different approaches.

To have a complete overview of laboratory measurement methods of airborne sound insulation is also tricky, if considering that the first tentative standardization, the ASTM E-90, goes back to 1950, even if, as London wrote in his work dated 1951, "standardization efforts along these lines go back to the late 1930's".

More recent is the introduction of sound intensity measurement technique, although the first work to be referred to was made by Waterhouse in 1955. In the middle of the 80's, in fact, the Waterhouse correction was suggested to be used to modify the results obtained by the intensity method closer to the results obtained by the pressure method settled in the ASTM E-90.

Thus, try to reconstruct the chronological evolution of such research field is not a simple matter.

An organic and well organized resume can be found in the work of Hongisto (2000). The author coped with the topic discussing the evolution of measurements techniques and prediction methods. The experimental part was treated analyzing contributions from literature to pressure and intensity based techniques, also highlighting their limitations

and drawbacks (flanking transmission, sound leakage). The prediction part was organized separating the problem of sound insulation of single panels from double panels and sandwich structures.

Integrating Hongisto's references with a further cataloguing that differentiates deterministic and energy methods, it can be obtained the time scale illustrated in the following Table 2.1.

Years	1925-1934	1935-1944	1945-1954	1955-1964	1965-1974	1975-1984	1985-1994
Pressure Meth.	Davis (1925)		ASTM E-90 (1950)				
Intensity Meth.				Waterhouse (1955)		Gade (1982)	
Single Panel			Cremer (1942)			Ordubadi and Lyon (1979)	
Double Panel			London (1950)		White and Powell (1966)		
Sandwich Panel				Kurtze and Watters (1959)			Moore and Lyon (1991)
Deterministic Meth.					Zienkiewicz (1967)	Everstine (1981)	Roussos (1985)
Energy Meth.				Maidanik (1962)			Leppington et alii (1986)

Table 2.1 – TL measurements and prediction from an historical prospective

Of course the latter papers cited for each topic mean only that at that time, the specific technique reached, in the opinion of the author of the present work, a plenty development. In the last 15 years the topic of the radiated/transmitted sound has been object of further studies, some of them dealing with prediction methods, for example the discrete coordinate approach (Cunefare and Alley, 1994) applied in the following chapters, some others centred on innovative measurements techniques based on microphones arrays such as acoustic holography (Hald, 2000) and beamforming (Christensen and Hald, 2004).

A topic related with the sound insulation that will be discussed hereby is the evaluation of the effects of innovative damping treatments for composite panels, for example Chandra et alii (1999) and Crocker (2006).

Other interesting works, whose results have been applied in the present work deal with structural waves propagation, coped with spectral approaches (Shorter 2004), or with waveguides FE models (Mace 2005).

2.1 Transmission Loss prediction

The propagation of sound begins with the vibration of a fluid. The vibration of the fluid produces pressure waves. When a propagating pressure wave is interrupted by an

infinite barrier, the incident pressure wave is dispersed into two new waves. The infinite barrier is used because it eliminates the need to account for diffraction of the sound around the edges of the barrier. Some of the wave is reflected back toward the source and some of the wave is allowed to pass through the barrier. The part of the wave that is reflected back is referred to as the reflected pressure wave and the part of the wave that is allowed to pass through the barrier is called the transmitted pressure wave.

These three basic pressure terms are used to discuss the effects of barriers and enclosures.

Figure 2.1 is a representation of incident and transmitted pressure on a surface. This representation is only for normal incidence even though a noise source can produce random incidence on a surface.

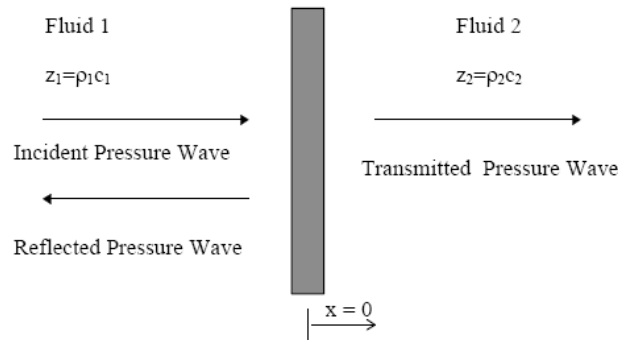


Figure 2.1 - Pressure Waves Normally Incident on a Panel

The equation for pressure waves on a surface is complex and varies over frequency and position. It is further complicated by the effects of the multiple degrees of incidence on the surface. Since computations were done by hand, the early models that were developed are quite simplistic and do not incorporate boundary conditions, nor the effects of random incidence of noise on a surface or its directivity.

Sound Transmission Loss, TL, is generally used to describe the amount of sound reduction, in dB units, that a partition imparts to the transmitted acoustic wave.

It is possible to define the TL as

$$TL = 10 \log \left(\frac{1}{\tau} \right) = 10 \log \left(\frac{\Pi_i}{\Pi_t} \right) = 10 \log \left(\frac{|p_i|^2}{|p_t|^2} \right) \quad (2.1)$$

where τ is the sound transmission coefficient, Π_i and Π_t are respectively the sound power incident and transmitted through the partition (p_i and p_t are the correspondent pressure values).

The sound reduction of a solid partition is frequency-selective as can be seen from the diagram in Figure 2.2. At low frequencies the stiffness of the material is the main controlling factor. Just above this point, various resonances cause major variation in sound transmission.

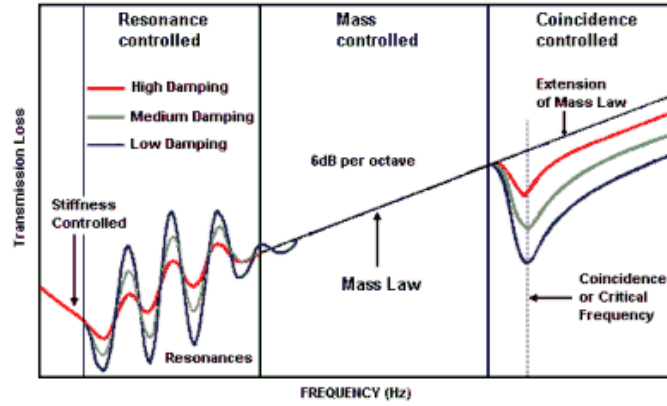


Figure 2.2 - TL behaviour with frequency

At about an octave above the lowest resonance, the mass of the wall takes over and dominates the sound reduction performance. Here the sound transmission loss depends on the surface density of the panel. It increases by 6 dB per doubling of mass.

High frequencies cause bending or ripple waves through a wall. Unlike compression waves, the velocity c_b of bending waves increases with frequency and, for an homogeneous wall is given by the relation.

$$c_b = \sqrt[4]{\frac{\omega^2 D}{\rho h}} \quad (2.2)$$

Where $\omega=2\pi f$ is the angular frequency, ρ and h are respectively the density and the thickness of the wall, supposed homogeneous, and D is its flexural stiffness:

$$D = \frac{Eh^3}{12(1-\nu^2)} \quad (2.3)$$

With E Young modulus and ν Poisson coefficient.

The wavelength of the bending wave is different from that of the incident sound wave which created it except at one frequency. This is the critical or coincidence frequency f_{crit} at which the bending wave speed in the material equals the speed of sound in the air, c_0 .

$$f_{crit} = \frac{c_0}{2\pi} \sqrt{\frac{\rho h}{D}} \quad (2.4)$$

At this frequency the waves coincide, and reinforce each other, in phase. This greatly reduces the sound reduction performance of the panel around the critical frequency. Every wall has a critical or coincidence frequency at which point the transmission loss reduces considerably. In the following Figure 2.3, the coincidence frequency, f_{crit} , for radiation into air from plates of various materials as a function of plate thickness is illustrated. A first order approximation of the critical frequency of an aluminium panel can be obtained dividing 12000 by the panel thickness in millimetres.

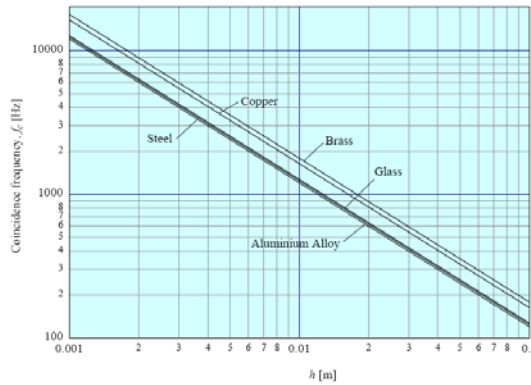


Figure 2.3 - Coincidence frequency as a function of plate thickness, h

Many text books such as Kinsler et al. (1982), Fahy (1985), Beranek et al. (1992) provide apparently simple mathematical models to approximate transmission loss. These models are for the ideal cases of infinite panel dimensions and do not include boundary conditions.

To explain the infinite panel, theories on transmission loss begin with the mathematical expressions to describe the incident, reflected and transmitted pressures. It is important to discern the incident side and the transmitted side of a barrier.

In the Figure 2.1 the effects of a barrier on an incident pressure wave at normal incidence are illustrated. The mathematical expressions for the different pressure components, under the hypothesis of progressive plane wave incident on the wall, are:

$$p_i(x, t) = P_i e^{j(\omega t - K_1 x)} \quad (2.5)$$

$$p_r(x, t) = P_r e^{j(\omega t + K_1 x)} \quad (2.6)$$

$$p_t(x, t) = P_t e^{j(\omega t - K_2 x)} \quad (2.7)$$

Where the wavenumbers K_1 and K_2 are defined as $K_1 = \frac{\omega}{c_1}$ and $K_2 = \frac{\omega}{c_2}$

The equilibrium of the pressures and the normal velocities on the wall, under the hypothesis of neglecting the mass of the wall itself, can be formulated as:

$$p_i(0,t) + p_r(0,t) = p_t(0,t) \quad (2.8)$$

$$u_i(0,t) + u_r(0,t) = u_t(0,t) \quad (2.9)$$

Where the normal velocity u of the pressure wave is defined as

$$u = \pm \frac{p}{Z_x} \text{ with } Z_x = \rho_x c_x \text{ acoustic impedance of the fluid and the sign that depends}$$

on the direction of propagation of the wave.

Therefore the continuity of normal velocity can be written as:

$$\frac{p_i(0,t)}{\rho_1 c_1} - \frac{p_r(0,t)}{\rho_1 c_1} = \frac{p_t(0,t)}{\rho_2 c_2} \quad (2.10)$$

It is then possible to solve the following system of linear equations in the unknown P_t and P_r :

$$P_t - P_r = P_i \quad (2.11)$$

$$\frac{P_t}{\rho_2 c_2} + \frac{P_r}{\rho_1 c_1} = \frac{P_i}{\rho_1 c_1} \quad (2.12)$$

The system above admits the following solutions:

$$R = \frac{\rho_2 c_2 - \rho_1 c_1}{\rho_1 c_1 + \rho_2 c_2} \quad (2.13)$$

$$T = \frac{2\rho_2 c_2}{\rho_1 c_1 + \rho_2 c_2} \quad (2.14)$$

Where they have been defined the pressure reflection coefficient $R = P_r/P_i$ and the pressure transmission coefficient $T = P_t/P_i$.

It has to be noted that if $\rho_1 c_1 = \rho_2 c_2$, then $R=0$ and $T=1$, i.e. the wall is acoustically transparent.

2.1.1 Mass Law for Normal incidence

If the hypothesis of neglecting wall mass is removed, it can be considered a wall with a finite thickness h and surface density $\rho_s = \rho h$. In this latter case the wall is characterized by its mass whereas its stiffness and damping properties are not considered. This assumption is representative of the case where inertial forces are much higher than elastic forces acting on the panel.

The force equilibrium on the wall can be written as:

$$p_i(0,t) + p_r(0,t) = p_t(0,t) + \rho h \frac{\partial u}{\partial t} \quad (2.15)$$

if the velocity is expressed in harmonic form as

$$u(x,t) = U e^{j(\omega t - Kx)} \quad (2.16)$$

The above equation leads to the linear equation:

$$P_i + P_r = P_t + j\omega\rho_s U_t \quad (2.17)$$

The transmitted normal velocity, if the medium on both sides of the wall is the same and its impedance is equal to $\rho_0 c$, can be expressed as:

$$U_t = \frac{P_t}{\rho_0 c} \quad (2.18)$$

That, if substituted in the equation (2.17) gives the relation:

$$P_i + P_r = P_t \left(1 + \frac{j\omega\rho_s}{\rho_0 c} \right) \quad (2.19)$$

That, if solved as system together with the equation of equilibrium of the normal velocities on the wall, (2.9), leads to following the relation:

$$T = \frac{P_t}{P_i} = \left(\frac{1}{1 + \frac{j\omega\rho_s}{2\rho_0 c}} \right) \quad (2.20)$$

The transmitted acoustic intensity is:

$$I_T = \frac{1}{2} \frac{|P_t|^2}{\rho_0 c} = \frac{1}{2} \frac{|P_i|^2}{\rho_0 c} \left| \frac{1}{1 + \frac{j\omega\rho_s}{2\rho_0 c}} \right|^2 \quad (2.21)$$

If normal incidence is considered, then is possible to define the power transmitted through the wall Π_t as:

$$\Pi_t = \frac{1}{2} \frac{A |P_i|^2}{\rho_0 c} \left| \frac{1}{1 + \frac{j\omega\rho_s}{2\rho_0 c}} \right|^2 \quad (2.22)$$

From the previous equation it derives that the sound transmission coefficient, τ , can be defined as:

$$\tau(\omega) = \frac{\Pi_t}{\Pi_i} = \frac{P_t^2}{P_i^2} = \frac{1}{\left|1 + \frac{j\omega\rho_s}{2\rho_0c}\right|^2} = \frac{1}{1 + \left(\frac{\omega\rho_s}{2\rho_0c}\right)^2} \quad (2.23)$$

It is possible to express the sound Transmission Loss, TL, as

$$TL(\omega) = 10\log\left(\frac{1}{\tau(\omega)}\right) = 10\log\left(\frac{\Pi_i}{\Pi_t}\right) = 10\log\left(1 + \left(\frac{\omega\rho_s}{2\rho_0c}\right)^2\right) = 20\log\left(\frac{\omega\rho_s}{2\rho_0c}\right) \quad (2.24)$$

The sound transmission loss under the hypotheses made depends only by the surface density of the partition. It has a linear behaviour in a log scale and its value increases of 6 dB per octave. Furthermore, from the previous expression it descends that doubling the mass of the partition at fixed frequency causes a 6 dB increase of the TL.

In ambient conditions, $\rho_0 = 1.18 \text{ Kg/m}^3$ and $c = 343 \text{ m/s}$, it results:

$$TL(f) = 20\log\left(\frac{2\pi f\rho_s}{2\rho_0c}\right) = 20\log(f\rho_s) + 20\log\left(\frac{2\pi}{2\rho_0c}\right) = 20\log(f\rho_s) - 42.3 \quad (2.25)$$

2.1.2 Mass Law for Oblique incidence

If the acoustic wave impinges the wall with an angle $\theta \neq 90^\circ$, then the sound transmission coefficient depends from θ :

$$\tau(\omega, \theta) = \frac{1}{1 + \cos\theta \left(\frac{\omega\rho_s}{2\rho_0c}\right)^2} \quad (2.26)$$

From this relation it descends that the transmission loss too depends from the angle of incidence:

$$TL(\omega, \theta) = 20\log\left(\frac{\omega\rho_s}{2\rho_0c} \cos\theta\right) \quad (2.27)$$

2.1.3 Mass Law for Random incidence

If it is considered not a single wave incident on the partition but a number of waves having different angles of incidence, an average sound transmission coefficient can be expressed as:

$$\bar{\tau}(\omega) = \frac{2}{1 - \cos 2\theta} \int_0^\theta \tau(\omega, \theta) \sin 2\theta d\theta \quad (2.28)$$

The integration is usually performed for angles θ included in the interval $[0^\circ, 78^\circ]$.

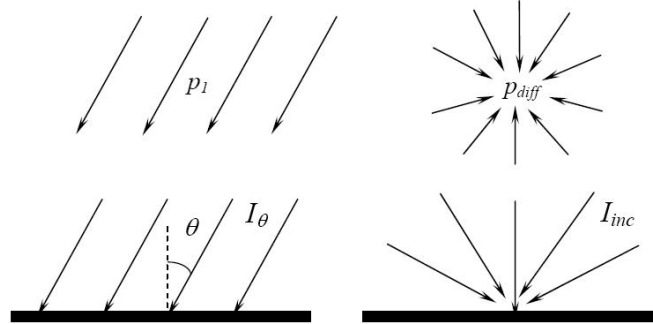


Figure 2.4 – Oblique VS. Diffuse incidence on a surface

In this case, integrating the previous equation, the following average sound transmission coefficient is achieved:

$$\bar{\tau}(\omega) = \frac{1}{0.473 \left(\frac{\omega \rho_s}{2 \rho_0 c} \right)^2} \ln \left[\frac{1 + \left(\frac{\omega \rho_s}{2 \rho_0 c} \right)^2}{1 + 0.0435 \left(\frac{\omega \rho_s}{2 \rho_0 c} \right)^2} \right] \quad (2.29)$$

From where it can be derived for the transmission loss for random incidence:

$$TL(\omega) = 10 \log \left[\frac{\left(0.978 \frac{\omega \rho_s}{2 \rho_0 c} \right)^2}{\ln \left[\frac{1 + \left(\frac{\omega \rho_s}{2 \rho_0 c} \right)^2}{1 + \left(0.208 \frac{\omega \rho_s}{2 \rho_0 c} \right)^2} \right]} \right] \quad (2.30)$$

2.1.4 Infinite panel Transmission Loss model

If the hypothesis of neglecting the stiffness of the partition with respect to inertial forces is removed, the fundamental equilibrium equation, for a symmetrically layered composite partition, is the dynamic bending equation (see Appendix A):

$$\begin{aligned}
D_{11} \frac{\partial^4 w}{\partial x^4} + 4D_{16} \frac{\partial^4 w}{\partial x^3 \partial y} + 2(D_{12} + 2D_{66}) \frac{\partial^4 w}{\partial x^2 \partial y^2} + 4D_{26} \frac{\partial^4 w}{\partial x \partial y^3} + D_{22} \frac{\partial^4 w}{\partial y^4} + \rho_s \frac{\partial^2 w}{\partial t^2} = \\
= p_i(x, y, t) + p_r(x, y, t) - p_t(x, y, t)
\end{aligned} \quad (2.31)$$

Where $w(x, y, t)$ are the panel's displacements in the normal direction, D_{ij} are the anisotropic plate stiffness values that relate the internal bending and twisting moments of the plate to the twists and curvatures they induce and $\rho_s = \rho h$ is the surface density of the panel of thickness h .

For an isotropic plate, it results:

$$D_{11} = D_{22} = \frac{Eh^3}{12(1-\nu^2)}; \quad D_{12} = \nu D_{11}; \quad D_{66} = \frac{Gh^3}{12} \quad (2.32)$$

And, because twisting behaviour is uncoupled from bending behaviour:

$$D_{16} = D_{26} = 0 \quad (2.33)$$

For an orthotropic plate, it results

$$D_{11} \neq D_{22} \text{ but again } D_{16} = D_{26} = 0 \quad (2.34)$$

If boundary conditions are not considered, the displacements of the panel can be expressed as:

$$w(x, y, t) = W e^{j[\omega t - (k_x x + k_y y)]} \quad (2.35)$$

Where $k_x = \frac{\omega}{c} \sin \theta_i \cos \phi_i$ and $k_y = \frac{\omega}{c} \sin \theta_i \sin \phi_i$.

Angles θ and ϕ respectively are co-elevation and azimuth angle formed by the incident wave with the panel's normal, are the wave numbers in both directions x and y .

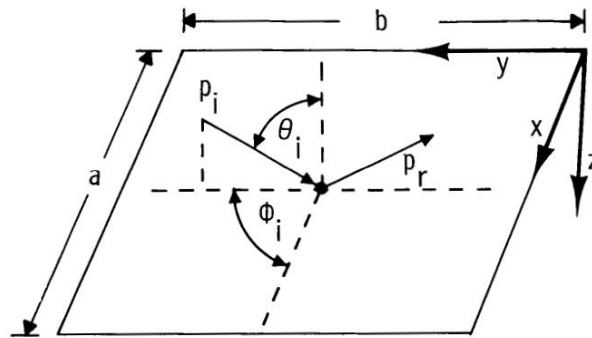


Figure 2.5 – Geometry on the incident side of the plate

By substituting the previous relation in the equation of motion of the panel (2.31), this assumes the form:

$$\begin{aligned} & \left[D_{11}K_x^4 + 4D_{16}K_x^3K_y + 2(D_{12} + 2D_{66})K_x^2K_y^2 + 4D_{26}K_xK_y^3 + D_{22}K_y^4 + \rho_s\omega^2 \right] W = \\ & = P_i + P_r - P_t \end{aligned} \quad (2.36)$$

Considering that the displacement W can be expressed in terms of normal component of the the vibration velocity V_n , thus of the transmitted pressure P_t , as:

$$W = \frac{V_n}{j\omega} = \frac{1}{j\omega} \frac{P_t}{\rho_0 c} \quad (2.37)$$

And indicating as:

$$\begin{aligned} \tilde{D} = & D_{11} \cos^4 \phi_i + 4D_{16} \cos^3 \phi_i \sin \phi_i + 2(D_{12} + 2D_{66}) \cos^2 \phi_i \sin^2 \phi_i + \\ & + 4D_{26} \cos \phi_i \sin^3 \phi_i + D_{22} \sin^4 \phi_i \end{aligned} \quad (2.38)$$

The previous equation (2.36) becomes

$$\left(\tilde{D} \frac{\omega^4}{c^4} \sin^4 \theta_i + \rho_s \omega^2 \right) \frac{P_t}{j\omega \rho_0 c} = P_i + P_r - P_t \quad (2.39)$$

From where it results:

$$\left(1 + \frac{j\rho_s \omega}{\rho_0 c} - \frac{j}{\omega \rho_0 c} \tilde{D} \frac{\omega^4}{c^4} \sin^4 \theta_i \right) P_t = P_i + P_r \quad (2.40)$$

That, if solved in system with equation (2.9) in terms of the ratio between incident and transmitted pressure leads to the relation:

$$\frac{P_i}{P_t} = \frac{1}{2} \left(2 + \frac{j\rho_s \omega}{\rho_0 c} - \frac{j}{\omega \rho_0 c} \tilde{D} \frac{\omega^4}{c^4} \sin^4 \theta_i \right) \quad (2.41)$$

It can be noted that if incident wave is normal to the panel so that $\theta_i=0$, the previous relation gives again the mass law.

In order to achieve the field incidence sound transmission coefficient, the incident and transmitted intensities are each integrated over a hemispherical solid angle defined by θ_i and ϕ_i .

$$\bar{\tau}(f) = \frac{\int_{\phi_i=0}^{2\pi} \int_{\theta_i=0}^{\theta_{im}} \tau(\theta_i, \phi_i, f) \cos \theta_i \sin \theta_i d\theta_i d\phi_i}{\int_{\phi_i=0}^{2\pi} \int_{\theta_i=0}^{\theta_{im}} \cos \theta_i \sin \theta_i d\theta_i d\phi_i} \quad (2.42)$$

Where θ_{im} is commonly equated to 78° for diffuse incidence transmission.

2.1.5 Coincidence Effect

From the equation (2.41) it appears that exists a frequency for which the inertial forces are in equilibrium with elastic forces:

$$\frac{\rho_s \omega}{\rho_0 c} = \frac{1}{\omega \rho_0 c} \tilde{D} \frac{\omega^4}{c^4} \sin^4 \theta_i \quad (2.43)$$

If the acoustic media in which the panel is collocated have equal impedance, at this frequency it results:

$$\tau(f_c) = 1 \text{ and } TL(f_c) = 0 \quad (2.44)$$

The panel is transparent to the acoustic radiation, i.e. all the incident sound is transmitted through the panel.

This effect is known as coincidence effect and the frequency at which it arises is called coincidence frequency:

$$f_c = \frac{c^2}{2\pi \sin^2 \theta_i} \sqrt{\frac{\rho_s}{\tilde{D}}} \quad (2.45)$$

From the point of view of its physical meaning, the coincidence effect is a spatial resonance that occurs when the trace on the panel of the acoustic wavelength is equal to the free bending wavelength of the panel. If the incident sound wave is normal to the panel ($\theta_i=0$), there is no coincidence effect.

The critical frequency, f_{crit} , is defined as the lowest possible value of the coincidence frequency.

In presence of damping, the Transmission Loss will not be zero: for a metallic panel a drop of 10-15 dB from the mass law level is quite usual.

2.1.6 Finite panel Transmission Loss model

Infinite panel theory is applicable when panel's dimensions are much bigger than its bending wavelength λ_b . This latter depends from stiffness characteristic of the structure as well as from the frequency of the incident acoustic wave.

$$\lambda_b = 2\pi \frac{c_b}{\omega} \quad (2.46)$$

Being the bending velocity c_b given by the relation:

$$c_b^2 = \omega \sqrt{\frac{\tilde{D}}{\rho_s}} \quad (2.47)$$

The bending wavelength is:

$$\lambda_b = 2\pi \frac{1}{\sqrt{\omega}} \sqrt[4]{\frac{\tilde{D}}{\rho_s}} \quad (2.48)$$

If the frequency of the acoustic wave impinging the panel decreases, the bending wavelength increases and the hypothesis of the infinite panel theory is not verified anymore. Boundary conditions effects are not negligible and it is important to evaluate consequences of the finite dimension of the panel on its acoustic behaviour.

For this reasons, the acoustic behaviour of panels in the low frequency region is usually modelled considering the panel simply supported along its edges and collocated in an infinite baffle.

Under the hypothesis of the classic thin panel theory, the equation of motion governing the bending vibrations of a symmetric anisotropic composite plate is the:

$$D_{11} \frac{\partial^4 w}{\partial x^4} + 4D_{16} \frac{\partial^4 w}{\partial x^3 \partial y} + 2(D_{12} + 2D_{66}) \frac{\partial^4 w}{\partial x^2 \partial y^2} + 4D_{26} \frac{\partial^4 w}{\partial x \partial y^3} + D_{22} \frac{\partial^4 w}{\partial y^4} + C_D \frac{\partial w}{\partial t} + \rho_s \frac{\partial^2 w}{\partial t^2} = p_i(x, y, t) + p_r(x, y, t) - p_t(x, y, t) \quad (2.49)$$

This equation differs from the (2.31) for the presence of the damping term that was neglected in the infinite panel theory discussion. C_D , in fact, is the so called viscous damping coefficient.

For the sake of simplicity, the following results will be deduced for an homogeneous panel, knowing that noise transmission calculations can be performed in the same manner for composite panels.

The cited dynamic equilibrium equation for an homogeneous panel is in the form:

$$D\nabla^4 w + C_D \frac{\partial w}{\partial t} + \rho_s \frac{\partial^2 w}{\partial t^2} = p_i(x, y, t) + p_r(x, y, t) - p_t(x, y, t) \quad (2.50)$$

Where:

$$\nabla^4 = \frac{\partial^4}{\partial x^4} + 2 \frac{\partial^4}{\partial x^2 \partial y^2} + \frac{\partial^4}{\partial y^4}$$

The three pressure terms involved in the previous equation can be rewritten as the sum of the blocked pressure (the pressure that occurs on the incident side when the plate is considered as infinitely rigid) and the reradiated pressure (the pressure due to the plate vibration). The reradiated pressure is an unknown function of the plate displacement w , that make very complicated the solution of the previous equation. If reradiated pressure contribution in the equation of motion of the plate is neglected, as it

will be done herein, the error is acceptable, less than 1 dB according to infinite panel theory, except at frequencies close to panel's first proper frequencies.

2.1.6.1 Incident Power Expression

The known term of the equation of motion of the panel can then be written as:

$$p_i(x, y, t) + p_r(x, y, t) - p_t(x, y, t) \cong p_b(x, y, t) = 2p_i(x, y, t) \quad (2.51)$$

If the incident pressure is assumed to be a plane wave impinging on the panel, at $z=0$, with constant amplitude P_i and with an oblique angle (θ_i, ϕ_i) , then it can be expressed as:

$$p_i(x, y, t) = P_i e^{j(\omega t - K_x x - K_y y)} \quad (2.52)$$

Starting from the expression of incident pressure, incident intensity and power can to be calculated.

The acoustic intensity is defined as the average rate of flow of energy through a given area:

$$I = \frac{\text{Force}}{\text{Area}} \text{Velocity} = pv$$

For a plane wave, pressure and velocity are in phase, then the intensity can be expressed as:

$$I = \frac{P_{rms}^2}{\rho_0 c} = \frac{P^2}{2\rho_0 c} \quad (2.53)$$

Where P_{rms} is the "effective" value of the pressure and is given by the relation:

$$P_{rms} = \sqrt{\frac{1}{T} \int_0^T p^2 dt} \quad (2.54)$$

If the pressure has harmonic dependence, then it results $P_{rms} = P/\sqrt{2}$

Considering that the incident intensity on the plate can be calculated as the amount of intensity that is normal to the plate, it leads to the following relation:

$$I_i = \frac{P_i^2}{2\rho_0 c} \cos \theta_i \quad (2.55)$$

The acoustic power Π_i incident on the plate is given by the incident intensity multiplied by the area it acts on, that is, the area of the plate. Thus, Π_i is given by:

$$\Pi_i = \frac{P_i^2 ab}{2\rho_0 c} \cos \theta_i \quad (2.56)$$

Again, if a diffuse incidence is considered, the rms value of the incident pressure p_{diff_rms} can be calculated as the result of sound waves propagating from all the directions, each having intensity I_i .

$$P_{diff_rms}^2 = \int_{\psi=4\pi} I_i \rho_0 c d\psi = 4\pi I_i \rho_0 c \quad (2.57)$$

The total incident sound power per unit area is found by integration over all angles of incidence covering a half sphere in front of the surface, see Figure 2.6.

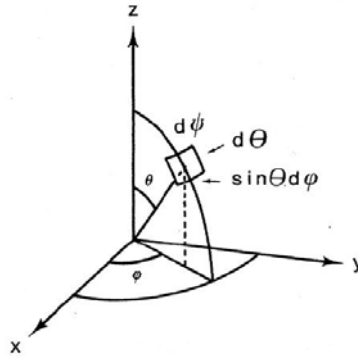


Figure 2.6 – Definition of incident angles in a diffuse sound field

$$I_{diff} = \int_{\psi=2\pi} I_i d\psi = \int_0^{2\pi} \int_0^{\pi/2} \frac{P_{diff_rms}^2}{\rho_0 c} \cos \theta \sin \theta d\theta d\phi = \frac{P_{diff_rms}^2}{4\rho_0 c} \quad (2.58)$$

It is worth to notice that the incident acoustic intensity in the hypothesis of diffuse fields is four times less than in the case of a plane wave with normal incidence.

2.1.6.2 Radiated Power Expression

The determination of the pressure field radiated by a vibrating plate can be started from the well known Helmholtz-Kirchhoff theorem that states that the solution of the homogeneous wave equation, (1.9), reported here:

$$\nabla^2 p - \frac{1}{c^2} \frac{\partial^2 p}{\partial t^2} = 0 \quad (2.59)$$

in a generic field position Q can be expressed in terms of p and $\frac{\partial p}{\partial n}$ on a arbitrary closed surface S that encloses Q .

By applying the Green theorem, it is possible to write:

$$P(q) = -\frac{1}{4\pi} \int_S \left[\frac{\partial P(q_s)}{\partial n} \left(\frac{e^{-jkR}}{R} \right) - P(q_s) \frac{\partial}{\partial n} \left(\frac{e^{-jkR}}{R} \right) \right] dS \quad (2.60)$$

Where $R=Q-Q_s$ with Q_s belonging to the surface S .

The expression:

$$G(Q/Q_s) = \left(\frac{e^{-jkR}}{R} \right) \quad (2.61)$$

introduces the so called first-type or full space Green's function and represents the pressure field in x generated by a point source in Q_s .

In the case of the panel collocated in an infinite baffle, S can be thought as constituted by the panel surface Σ and a spherical cap centred in Q (Figure 2.7).

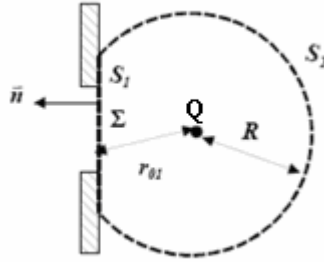


Figure 2.7 – Integration surface

On the spherical cap, if R tends toward infinite, it can be applied Sommerfeld radiation condition:

$$\lim_{R \rightarrow \infty} R \left(\frac{\partial P}{\partial n} - jkP \right) = 0 \quad (2.62)$$

that express the behaviour of a spherical wave to be locally plane when the radius approaches at infinity.

It descends that the pressure field radiated by a vibrating surface Σ can be expressed in terms of the boundary conditions on the surface as:

$$P(Q) = \frac{1}{4\pi} \int_{\Sigma} \left[\frac{\partial P(Q_s)}{\partial n} \left(\frac{e^{-jkR}}{R} \right) - P(Q_s) \frac{\partial}{\partial n} \left(\frac{e^{-jkR}}{R} \right) \right] d\Sigma \quad (2.63)$$

The term $\frac{\partial P}{\partial n}$ can be related to the panel normal velocities and displacements by the equation:

$$\frac{\partial P(Q_s)}{\partial n} = -j\omega\rho_0 V_n(x_s, y_s) = \omega^2 \rho_0 W(x_s, y_s) \quad (2.64)$$

where x_s and y_s are the coordinate of Q_s on the surface Σ .

The pressure term, instead, can not be related to panel's displacement neither can be measured.

It is then possible to apply the so called image method by choosing an opportune Green function that is constituted by the superposition of two monopole source, one in the position of the solution point Q and the other one, Q' in opposite position with respect to the panel. By following this method, it can be written the half space Green's function:

$$G_H [(Q/Q_s), (-Q_s/Q)] = \frac{e^{-jkR}}{R} + \frac{e^{-jkR'}}{R'} = 2G(Q/Q_s) \quad (2.65)$$

It can be noted that:

$$\frac{\partial G_H}{\partial n} = \frac{\partial G}{\partial R} \cos \theta + \frac{\partial G}{\partial R'} \cos(\pi - \theta) = 0 \quad (2.66)$$

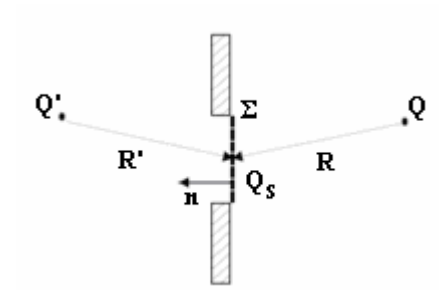


Figure 2.8 – Image method

By substituting in the equation (2.63) it can be achieved the Rayleigh integral that expresses the radiated pressure in terms of the panel's displacements:

$$P(Q) = \frac{\omega^2 \rho_0}{4\pi} \int_{\Sigma} \frac{e^{-jkR}}{R} W(x_s, y_s) d\Sigma \quad (2.67)$$

The steady state solution for the plate vibration displacement is the only part of solution that influences plate noise transmission. Being the forcing pressure harmonic, the displacement will be harmonic too.

$$w(x, y, t) = W(x, y) e^{j\omega t} \quad (2.68)$$

Substituting the expression found for pressure and displacement into the equation of motion and dividing by $e^{j\omega t}$, the equation (2.50) becomes:

$$D\nabla^4 W + j\omega C_D W - \omega^2 \rho_s W = 2P_i \exp[-jk \sin \theta_i (x \cos \phi_i + y \sin \phi_i)] \quad (2.69)$$

If the plate is assumed to be finite, rectangular, with dimensions a and b , the solution of previous equation can be achieved by using the method of eigenfunctions, also called modal approach. Homogeneously solving the cited equation and applying simple

support boundary conditions along the edges, as it has been showed in the Appendix A, leads to the relation:

$$W(x, y) = \sum_{m=1}^{\infty} \sum_{n=1}^{\infty} W_{mn} \sin\left(\frac{m\pi x}{a}\right) \sin\left(\frac{n\pi y}{b}\right) \quad (2.70)$$

In similar manner, expressing the spatial part of the forcing pressure as and infinite series of eigenfunctions allows to write the following relation:

$$2P_i \exp[-jk \sin \theta_i (x \cos \phi_i + y \sin \phi_i)] = \sum_{m=1}^{\infty} \sum_{n=1}^{\infty} P_{mn} \sin\left(\frac{m\pi x}{a}\right) \sin\left(\frac{n\pi y}{b}\right) \quad (2.71)$$

Where P_{mn} , the generalized pressure is given by:

$$\begin{aligned} P_{mn} &= \int_0^a \int_0^b p_b(x, y) \sin\left(\frac{m\pi x}{a}\right) \sin\left(\frac{n\pi y}{b}\right) dx dy = \\ &= 2P_i \int_0^a \int_0^b \exp[-jk \sin \theta_i (x \cos \phi_i + y \sin \phi_i)] \sin\left(\frac{m\pi x}{a}\right) \sin\left(\frac{n\pi y}{b}\right) dx dy \end{aligned} \quad (2.72)$$

The integral can be solved in closed form to obtain the generalized forcing pressure for each mode, :

$$P_{mn} = 2P_i \bar{I}_m \bar{I}_n \quad (2.73)$$

Where:

$$\bar{I}_m = \begin{cases} -\frac{j}{2} \operatorname{sgn}(\sin \theta_i \cos \phi_i) & se(m\pi) = (ka \sin \theta_i \cos \phi_i) \\ \frac{m\pi [1 - (-1)^m e^{-jka \sin \theta_i \cos \phi_i}]}{(m\pi)^2 - (ka \sin \theta_i \cos \phi_i)^2} & se(m\pi) \neq (ka \sin \theta_i \cos \phi_i) \end{cases} \quad (2.74)$$

$$\bar{I}_n = \begin{cases} -\frac{j}{2} \operatorname{sgn}(\sin \theta_i \sin \phi_i) & se(n\pi) = (kb \sin \theta_i \sin \phi_i) \\ \frac{n\pi [1 - (-1)^n e^{-jkb \sin \theta_i \sin \phi_i}]}{(n\pi)^2 - (kb \sin \theta_i \sin \phi_i)^2} & se(n\pi) \neq (kb \sin \theta_i \sin \phi_i) \end{cases} \quad (2.75)$$

The generalized displacement W_{mn} can now be achieved by substituting expression found in the equation of motion of the panel:

By dividing the expression found for P_{mn} by the generalized mass, that for a simply supported panel is $\gamma_{mn} = \rho_s ab/4$, it results

$$\bar{P}_{mn} = \frac{P_{mn}}{\gamma_{mn}} = \frac{8P_i \bar{I}_m \bar{I}_n}{\rho_s ab} \quad (2.76)$$

Thus, the generalized displacement can be written as:

$$W_{mn} = \frac{8P_i \bar{I}_m \bar{I}_n}{\rho_s [\omega_{mn}^2 - \omega^2 + j C_D \omega / \rho_s]} \quad (2.77)$$

Where

$$\omega_{mn}^2 = \frac{D\pi^4}{\rho_s} \left(\frac{m^2}{a^2} + \frac{n^2}{b^2} \right)^2 \quad (2.78)$$

2.2 TL calculations in discrete coordinates

As seen in the previous paragraphs, the TL of flat homogeneous and orthotropic panels, simply supported along the edges can be analytically calculate. For more complex structures including curvatures, different boundary conditions and damping treatments, it is useful to use capabilities offered by discrete coordinates. With a discrete coordinates approach, in fact, it is possible to perform calculations of some quantities necessary for TL prediction using a FE model of the structure to be investigated.

2.2.1 Radiated Power in discrete coordinates

The Rayleigh integral, whose derivation has been discussed in the previous paragraphs, expresses the sound pressure radiated from a vibrating surface Σ in a field point Q belonging to an hemisphere, as function of the surface normal displacements, w :

$$p(\omega, Q) = \frac{\omega^2 \rho_0}{2\pi} \int_{\Sigma} \frac{e^{-jkR}}{R} w(\omega, Q_s) d\Sigma \quad (2.79)$$

The power radiated from a vibrating surface is defined as:

$$\Pi_{rad}(\omega) = \frac{1}{2} \text{Real} \left\{ \int_{\Sigma} p(\omega, Q) v^*(\omega, Q) dS \right\} \quad (2.80)$$

thus, by substituting the (2.79) in the (2.80) it is obtained:

$$\Pi_{rad}(\omega) = \frac{1}{2} \text{Re} \left\{ \frac{\omega^2 \rho_0}{2\pi} \int_{\Sigma} \left(\int_{\Sigma} \frac{e^{-jkR}}{R} w(\omega, Q_s) d\Sigma \right) v^*(\omega, Q) d\Sigma \right\} \quad (2.81)$$

being the complex conjugate of the normal velocity $v^*(\omega, Q) = j\omega w^*(\omega, Q)$, the power Π_{rad} can then be written as:

$$\Pi_{rad}(\omega) = \frac{1}{2} \operatorname{Re} \left\{ \frac{j\omega^3 \rho_0}{2\pi} \int_{\Sigma} \left(\int_{\Sigma} \frac{e^{-jkR}}{R} w(\omega, Q_s) d\Sigma \right) w^*(\omega, Q) d\Sigma \right\} \quad (2.82)$$

multiplying and dividing for the wavenumber k , the (2.82) is:

$$\Pi_{rad}(\omega) = \frac{\omega^4 \rho_0}{4\pi c} \operatorname{Re} \left\{ \int_{\Sigma} \int_{\Sigma} j \frac{e^{-jkR}}{kR} w(\omega, Q_s) w^*(\omega, Q) d\Sigma d\Sigma \right\} \quad (2.83)$$

by applying the Euler's formula for complex analysis:

$$e^{-jkR} = \cos(kR) - j \sin(kR)$$

and being $j^2 = -1$, the equation (2.83) becomes:

$$\Pi_{rad}(\omega) = \frac{\omega^4 \rho_0}{4\pi c} \operatorname{Re} \left\{ \int_{\Sigma} \int_{\Sigma} \frac{[j \cos(kR) + \sin(kR)]}{kR} w(\omega, Q_s) w^*(\omega, Q) d\Sigma d\Sigma \right\} \quad (2.84)$$

when taking the real part, the radiated power can be expressed as:

$$\Pi_{rad}(\omega) = \frac{\omega^4 \rho_0}{4\pi c} \int_{\Sigma} \int_{\Sigma} \frac{\sin(kR)}{kR} w(\omega, Q_s) w^*(\omega, Q) d\Sigma d\Sigma \quad (2.85)$$

From the previous equations, it has to be noted that:

- in equation (2.83), the radiation function

$$\underline{R}(\omega) = \frac{e^{-jkR}}{kR} = \frac{\exp(-jk|Q-Q_s|)}{k|Q-Q_s|} \quad (2.86)$$

is symmetrical, $\underline{R}(\omega, Q, Q_s) = \underline{R}(\omega, Q_s, Q)$;

- the singularity in (2.85) is of the first order, $\lim_{|Q-Q_s| \rightarrow 0} \frac{\sin k|Q-Q_s|}{k|Q-Q_s|} = 1$

Thus, the power radiated can be expressed in its final formulation as:

$$\Pi_{rad}(\omega) = \frac{\omega^4 \rho_0}{4\pi c} \begin{cases} \int_{\Sigma} \int_{\Sigma} w^*(\omega, Q_s) \frac{\sin(kR)}{kR} w(\omega, Q) d\Sigma d\Sigma & \text{if } P \neq Q \\ \int_{\Sigma} \int_{\Sigma} w^*(\omega, Q_s) w(\omega, Q) d\Sigma d\Sigma & \text{if } P \equiv Q \end{cases} \quad (2.87)$$

The previous relation can be specialized for discrete coordinates, in the following manner:

$$\Pi_{rad}(\omega) = \frac{\omega^4 \rho_0}{4\pi c} \{W(\omega)\}^H [A][R(\omega)][A]\{W(\omega)\} \quad (2.88)$$

where: W is the displacement vector; R is the radiation resistance matrix; A is the nodal equivalent areas matrix.

Using modal coordinates, W can be expressed as:

$$\{W(\omega)\} = [\Phi][H(\omega)][\Phi]^T \{F(\omega)\} \quad (2.89)$$

where $[H(\omega)]$ is the panel's transfer matrix and $[\Phi]$ is the normal component of the modal displacement matrix that can be obtained, as it has been done in the present work, from finite element modal analysis.

The generic term of the transfer matrix for an undamped panel is in the form:

$$H_i(\omega) = \frac{1}{-m_i\omega^2 + k_i} \quad (2.90)$$

The damping can be introduced in the equation of motion using a complex stiffness term, $K_c(\omega) = K(\omega) \cdot (1 + j\eta(\omega))$. Among the several models using the complex modulus approach, the simplest is the so-called frequency-independent hysteretic damping model (e.g., Nashif), in which the modulus and loss factor of the material are assumed to be constant with frequency.

If the equation (2.90) is rewritten in terms of complex stiffness, the following expression is obtained:

$$H_i(\omega) = \frac{1}{-m_i\omega^2 + k_i(1 + j\eta(\omega))} \quad (2.91)$$

If a viscous damping model is introduced, where the damping is proportional to the velocity of motion and varies linearly with frequency, the transfer matrix terms are in the form:

$$H_i(\omega) = \frac{1}{-m_i\omega^2 + j\eta(\omega)\omega + k_i} \quad (2.92)$$

According to Mace, it is possible to write a general modal frequency operator that includes any structural modal damping model and evidences the generalised mass, m_i :

$$H_i(\omega) = \frac{1}{m_i} \frac{1}{\omega_i^2 - \omega^2 + j\Delta_i(\omega)\omega} \quad (2.93)$$

Here the generalized stiffness k_i is expressed as function of m_i and ω_i , the natural circular frequency for the i -th mode.

By substituting the expression (2.89) in the (2.88) it can be achieved:

$$\Pi_{rad}(\omega) = \frac{\omega^4 \rho_0}{4\pi c} \left\{ [\Phi][H(\omega)][\Phi]^T \{F(\omega)\} \right\}^H [\Lambda] \left\{ [\Phi][H(\omega)][\Phi]^T \{F(\omega)\} \right\} \quad (2.94)$$

where it has been defined the radiation matrix Λ :

$$[\Lambda] = [A][R(\omega)][A] \quad (2.95)$$

The equation (2.94) can be further manipulated considering that the transfer matrix H is diagonal, thus $H^H(\omega) \equiv H^*(\omega)$.

$$\Pi_{rad}(\omega) = \frac{\omega^4 \rho_0}{4\pi c} \left\{ \{F(\omega)\}^H [\Phi][H(\omega)]^* [\Phi]^T \right\} [\Lambda] \left\{ [\Phi][H(\omega)][\Phi]^T \{F(\omega)\} \right\} \quad (2.96)$$

The central product can be defined as a modal radiation resistance matrix:

$$[R_{rad}(\omega)] = \frac{\omega^4 \rho_0}{4\pi c} [\Phi]^T [A][\Phi] \quad (2.97)$$

that, substituted in the (2.96) gives the following expression of the radiated power in discrete coordinates :

$$\Pi_{rad}(\omega) = \{F(\omega)\}^H [\Phi][H(\omega)]^* [R_{rad}(\omega)][H(\omega)][\Phi]^T \{F(\omega)\} \quad (2.98)$$

2.2.2 Incident Power in discrete coordinates

Being the sound power impinging on the panel, under the hypothesis of normal incidence, given by the following relation:

$$\Pi_{inc}(\omega) = \frac{1}{2} \text{Re} \left(\{P(\omega)\} [A] \{V(\omega)\} \right) \quad (2.99)$$

where $V(\omega)$ is the particle velocity.

Once the A matrix and the pressure acting on each node are known, it is possible to calculate the force vector $F(\omega)$ that, in the present work has been calculated via a FE analysis of the panel under study when under the action of a distributed pressure load.

$$\{F(\omega)\} = [A] \{P(\omega)\} \quad (2.100)$$

given the previous relation, the following expression can be written for the incident power in discrete coordinates.

$$\Pi_{inc}(\omega) = \frac{1}{2} \text{Re} \left(j\omega \{F(\omega)\}^H \{W(\omega)\} \right) \quad (2.101)$$

In the hypothesis of a generic plane wave impinging on the panel with an angle θ_i , the incident pressure has the expression given in equation (2.56), $\Pi_i = \frac{P_i^2 ab}{2\rho_0 c} \cos \theta_i$.

Thus, it is possible, on the base of the results achieved from a modal analysis of the finite element model of a generic plane structure, to calculate the transmission loss by opportunely combining expressions (2.98) and (2.101).

$$TL(\omega) = 10 \log \frac{\Pi_{inc}(\omega)}{\Pi_{rad}(\omega)} = \frac{\frac{1}{2} \operatorname{Re} \left(j\omega \{F(\omega)\}^H \{W(\omega)\} \right)}{\{F(\omega)\}^H [\Phi] [H(\omega)]^* [R_{rad}(\omega)] [H(\omega)] [\Phi]^T \{F(\omega)\}} \quad (2.102)$$

2.3 Sound absorption

Another very important parameter to deal with when performing acoustic predictions and measurements is the absorption coefficient α , defined as the ratio of the non-reflected sound energy to the incident sound energy on a surface. It can take values between 0 and 1, and $\alpha=1$ means that all incident sound energy is absorbed in the surface. An example of a surface with absorption coefficient $\alpha=1$ is an open window.

2.3.1 Equivalent absorption area

The product of area and absorption coefficient of a surface material is the equivalent absorption area of that surface, i.e. the area of open windows giving the same amount of sound absorption as the actual surface. The equivalent absorption area of a room is:

$$A = \sum_i S_i \alpha_i = S_1 \alpha_1 + S_2 \alpha_2 + \dots = S \alpha_m \quad (2.103)$$

where S is the total surface area of the room and α_m is the mean absorption coefficient. The unit of A in the International System of Units (S.I.) is m^2 . In general, the equivalent absorption area may also include sound absorption due to the air and due to persons or other objects in the room.

2.3.2 Energy balance in a room

The total acoustic energy in a room is the sum of potential energy and kinetic energy, or twice the potential energy, since the time average of the two parts must be equal (see equation (1.32)). The total energy E is the energy density multiplied by the room volume V :

$$E = (w_{pot} + w_{kin}) V = \frac{p_{diff-rms}^2}{\rho_0 c^2} V \quad (2.104)$$

The energy absorbed in the room is the incident sound power per unit area, given by the equation (2.58), multiplied by the total surface area and the mean absorption coefficient, i.e. the equivalent absorption area.

$$W_{abs} = I_{inc} S \alpha_m = \frac{p_{diff-rms}^2}{4 \rho_0 c} A \quad (2.105)$$

If W_s is the sound power of a source in the room, the energy balance equation of the room is:

$$W_s - W_{abs} = \frac{dE}{dt} \quad (2.106)$$

By substituting in the previous equation the expressions found for E and W_{abs} , it can be achieved the relation:

$$W_s - \frac{p_{diff_rms}^2}{4\rho_0 c} A = \frac{V}{\rho_0 c^2} \frac{d}{dt} (p_{diff_rms}^2) \quad (2.107)$$

With a constant sound source a steady state situation is reached after some time, and the right side of the equation is zero. So, the absorbed power equals the power emitted from the source, and the steady state sound pressure in the room is:

$$p_{steady} = \sqrt{\frac{4W_s}{A}} \rho_0 c \quad (2.108)$$

From this equation it derives that the absorption area in a room has a direct influence on the sound pressure in the room.

2.3.3 Reverberation Time. Sabine's formula

If the sound source is turned off after the sound pressure has reached the stationary value, the first term in the energy balance equation (2.107) is zero, and the rms sound pressure is now a function of time:

$$\frac{p_{diff_rms}^2}{4\rho_0 c} A + \frac{V}{\rho_0 c^2} \frac{d}{dt} (p_{diff_rms}^2) = 0 \quad (2.109)$$

The solution of this equation, indicating p_{diff_rms} as \tilde{p} , can be written in the form:

$$\tilde{p}^2(t) = p_{steady}^2 e^{-\frac{cA}{4V}t} \quad (2.110)$$

where p_{steady}^2 is the mean square sound pressure in the steady state and $t=0$ is the time when the source is turned off. It is seen that the mean square sound pressure, and hence the sound energy, follows an exponential decay function. On a logarithmic scale the decay is linear, and this is called the decay curve, see Figure 2.9.

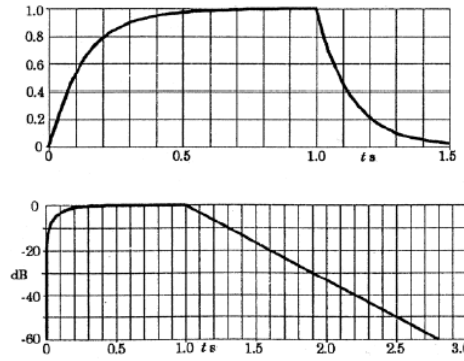


Figure 2.9 – Decay of sound in a room if the source is switched off at $t=1$ s. The upper curve is in a linear scale [p^2], whereas the lower is in a log scale [dB]

The reverberation time T_{60} is defined as the time it takes for the sound energy in the room to decay to one millionth of the initial value, i.e. a 60 dB decay of the sound pressure level. Hence, for $t=T_{60}$ it results:

$$\tilde{p}^2(t) = \frac{p_{steady}^2}{10^6} = p_{steady}^2 e^{-\frac{cA}{4V}T_{60}} \quad (2.111)$$

From the previous equation it can be obtained the expression of the reverberation time:

$$T_{60} = 6 \ln(10) \frac{4V}{cA} = \frac{55.26V}{cA} \quad (2.112)$$

This is Sabine's formula named after Wallace C. Sabine, who introduced the reverberation time concept around 1896. He was the first to demonstrate that T_{60} is inversely proportional to the equivalent absorption area A .

For this reason the mean absorption coefficient α_m introduced in the equation (2.103) is also known as Sabine's absorption coefficient:

$$\alpha_m = \frac{1}{S} \sum_i S_i \alpha_i = \frac{A}{S} \quad (2.113)$$

Hence the Sabine absorption coefficient of an absorbent can be determined by comparing the reverberation times of a room before and after the absorbent is introduced into the room.

If T_1 and T_2 are respectively the reverberation times of the chamber before and after the installation of the test specimen, then the absorption area A_s of the specimen is:

$$A_s = \frac{55.3V}{c} \left(\frac{1}{T_2} - \frac{1}{T_1} \right) \quad (2.114)$$

For a plane absorber, the absorption coefficient α is then calculated as:

$$\alpha = \frac{A_s}{S} \quad (2.115)$$

where S is the surface area of the absorber.

Another descriptor frequently used, for the pressure decay is the so called decay rate, d [dB/s], that can be obtained from the reverberation time by using the relation:

$$d = \frac{60}{T_{60}} \quad (2.116)$$

The essential requirement of the procedure is to ensure that the sound field in the reverberant room is as close as possible to Sabine's diffuse field model:

1. the local average energy density in the room is uniform,
2. energy is uniformly incident onto a surface from all directions,
3. the total sound absorption in the room is the sum of the absorptions of individual surfaces.

It is worth to notice that the last hypothesis implies that the incident energy per unit area over time is the same for all surfaces in the room. For this to hold it is necessary that no one part of the room has predominant absorptions.

Other absorption coefficient equations have been developed, the most notable from C.F. Eyring and R.F. Norris. Their derivation is based on the mean free path and the attenuation of reflections. The total energy attenuation is $(1 - \bar{\alpha}_E)^N$, where N is the number of reflections per second and $\bar{\alpha}_E$ is the average absorption coefficient for the Eyring-Norris derivation. Therefore,

$$\bar{\alpha}_E = 1 - e^{0.00268Vd/S} \quad (2.117)$$

This equation is consistent with the Sabine equation for small values of α_E . For large values of α_E , the Eyring-Norris equation yields a slightly smaller value for the absorption coefficient than the Sabine equation. When the sound field in the room is less diffuse, the Eyring-Norris formula predicts the absorption coefficient of the material more accurately than the Sabine equation. Thus, the Eyring-Norris equation is used commonly for architectural acoustics.

However, for absorption testing in reverberation chambers, where the sound field is very nearly diffuse, the Sabine equation is accurate and computationally straightforward.

2.4 Damping

In the previous paragraph different damping models have been introduced without going in detail about damping definitions and mechanisms. On the other hand, the importance of damping when discussing structure borne sound phenomena is undisputed.

Furthermore, aerospace structures, and sensitive equipment mounted on those structures, are often required to function through a wide range of dynamic loads. When structural resonances are excited, excessive levels of noise or vibration may be produced that can lead to structural failure such as acoustic fatigue. Additionally, excessive vibration may lead to the malfunction of equipment having, for example, electronic or optical components. Controlling vibration, other than reduce the level of sound transmitted through a structure, can reduce the likelihood of structural failure and increase the reliability of sensitive equipment.

The main sources of damping of structural response, before any attempt is made to increase it by artificial means, are structural, where energy is dissipated within the structure in the form of heat, and acoustic, where energy is radiated from the structure as sound. For typical aircraft structures, structural damping is dominant.

2.4.1 Structural damping

For traditional metallic structures, slip of mechanical joints and internal hysteresis of materials contribute to structural damping. The internal hysteretic damping of structural materials normally used in aircraft is small compared with that attributable to slipping of joints. At small amplitudes of vibration slip does not occur and any damping can only arise from material hysteresis. As the amplitude of vibration increases slip begins to occur near rivets and bolts and damping increases more.

When using fibre-reinforced composite materials, joints are usually bonded so that slippage does not occur at the joints and material damping is important for the reduction of dynamic response. The main sources of material damping in a composite arise from microplastic or viscoelastic phenomena associated with the matrix and relative slipping at the interface between the matrix and the reinforcement (Saravanos and Chamis, 1991, Chandra et alii, 1999).

The following factors influence the material damping in composites:

- The properties and relative proportions of the matrix and reinforcement materials within the composite.
- The size of the inclusions (e.g. long or short fibres, and fibre diameter).
- The orientation of the reinforcing material to the axis of loading.
- The surface treatment of the reinforcement.

2.4.2 Acoustic damping

The dominant source of acoustic damping derives from the radiation of sound energy into the fluid adjacent to the vibrating structure. The damping arises from the acoustic pressure that is in counter phase with and proportional to the plate velocity.

Within a panel array, the magnitude of the acoustic damping is dependent on the phase relationship between the motion of adjacent panels. Maximum acoustic damping occurs when adjacent panels are vibrating in-phase.

2.4.3 Damping treatments

When a damping layer is attached to a vibrating structure, it dissipates energy by direct and shear strains. When a solid beam or plate is bending, the direct strain increases linearly with distance from the neutral axis. Unconstrained damping layers, also known as free layer, which dissipate energy mainly by direct strain are attached to the remote surfaces, see Figure 2.10. For a complete survey of the damping treatments, see, for example the books of Nashif or Jones.

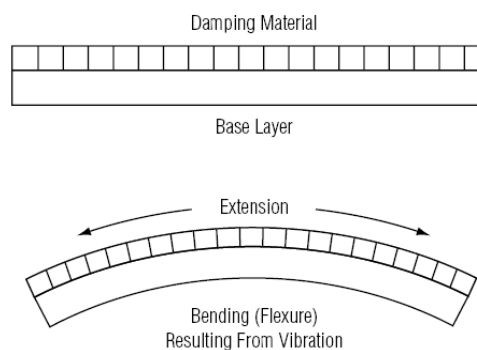


Figure 2.10 –Free layer damping treatment

The damping mechanism for constrained or embedded treatments, is substantially different. When the stiffness layers (constraining layer or skin) deform under transverse loads, the damping layers sandwiched between the stiffness layers experience shearing deformation (Figure 2.11).

The damping in these structures is mainly due to, and depends on, this shearing motion of the damping layers. On the other hand, the shear stress is the largest at the neutral axis and zero on the free surfaces. Therefore, layers embedded in the middle of the stacking sequence of a composite material maximize the dissipation of energy by shear stress

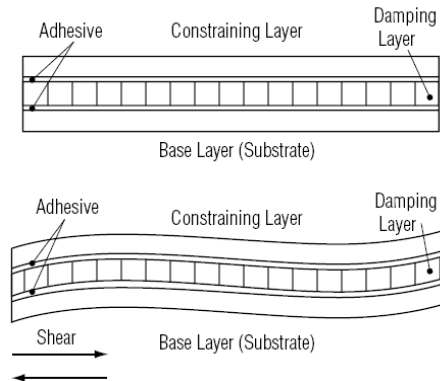


Figure 2.11 –Constraining/Embedded layer damping treatment

Furthermore, when viscoelastic layers are embedded in composite structures, their damping performance can be tailored to work in a given frequency range.

This can be done by using in the design phase a compliant layering approach, i.e. optimizing the lamination sequences such that the stiffness ratio between the damping and the adjacent composite layers maximize the damping for a given vibration mode of structure (Rao et alii, 1996).

Since the late 1950's many papers have been published on the vibration of sandwich structures. The Ross-Ungar-Kerwin model is one of the first theories which was developed for the damping in sandwich structures. In 1959 Kurtze evaluated that if one could construct plates which favour the propagation of shear rather than bending waves, such plates would have good sound insulation properties, provided the velocity of propagation of shear waves is appreciably less than the speed of the sound in air. He suggested that a plate consisting of a soft but incompressible core sandwiched between two metal skins could have the desirable properties of a large bending stiffness and a small shear stiffness. Since then, many models describing the dynamic behaviour of sandwich structures with single and multiple damping layers have been presented in the literature. These models are applicable for elastic and isotropic face plates and constraining layers. Gibson and Plunkett in 1977 have reviewed experimental and

analytical studies to characterize the dynamic properties of fibre-reinforced composite materials.

Instead of only considering the damping in the core, Ungar and Kerwin in 1962 proposed the so-called modal strain energy (MSE) model in order to include the damping capacities of all the elements. In this model the damping of the material can be characterized by the ratio of the energy dissipated in each element to the energy stored in the material. Based on the MSE method, Johnson and Kienholz in 1982 produced a method to predict damping in structures with constrained viscoelastic layers by using finite element analysis.

Moreover, special attention has to be paid to the choice of the viscoelastic material, in dependence of the operative temperature and frequency ranges.

Viscoelastic materials behaviour is usually described in terms of a complex modulus of elasticity, accounting for the elastic behaviour as well for the viscous one.

$$E_c = E_1 + jE_2 = E_1(1 + j\eta) \quad (2.118)$$

The real part of this complex term is the storage modulus, E_1 that defines the stiffness. The imaginary component is called loss modulus, E_2 and defines the energy dissipative ability of the material. The loss factor is here introduced as $\eta = E_2/E_1$.

Both E_1 and E_2 depend strongly from frequency and temperature, the latter is showed in the Figure 2.12.

Viscoelastic materials, in fact, exist in various unique states or “phases” over the broad temperature and frequency ranges in which they are used. These regions are typically referred to as the Glassy, Transition and Rubbery regions.

In the glassy region the polymer chains are rigidly ordered and crystalline in nature, possessing glass-like behaviour. Stiffness, E_1 , is at its highest for the material in this region, and damping levels are typically low.

The glass transition temperature, T_g , of a material refers to the elbow of the storage modulus curve at the edge of the glassy region as it enters into the transition region. T_g also defines the peak of the loss modulus, E_2 , curve. The transition region is so named because the material is transitioning from the glassy to the rubbery region. In this region the viscoelastic material goes through its most rapid rate of change in stiffness and possesses its highest level of damping performance. This is due to the fact that the long molecular chains of the polymer are in a semi-rigid and semiflow state, and are able to

rub against adjacent chains. These frictional effects result in the mechanical damping characteristic of viscoelastic materials.

In the rubbery region, the material reaches a lower plateau in stiffness. Damping is at a lower, but reasonable level. A material selected to exist in this region is ideally suited for such devices as isolators or tuned mass dampers because the modulus varies only slightly with changes in frequency and temperature.

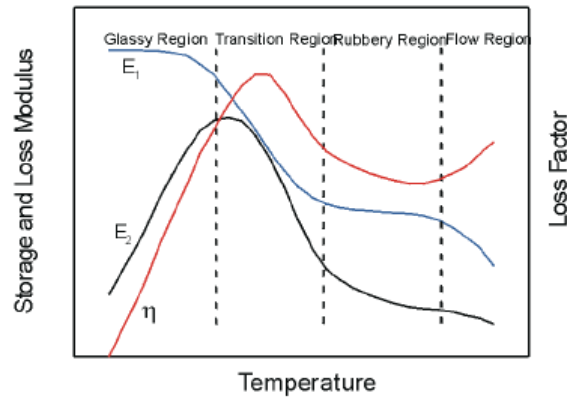


Figure 2.12 – Variation of Complex Modulus with Temperature for a Typical Viscoelastic Material

3 TL experimental measurements

As already stated, the sound transmission loss (TL) is a measure of the transmission coefficient, that is the fraction of the sound energy incident on a structure that is transmitted through it. Laboratory measurements of the sound Transmission Loss of a specimen can be conducted in dedicated facilities, usually constituted by a pair of reverberation chambers (sound pressure method) or by a reverberant source chamber coupled to an anechoic receiving chamber (sound intensity method). Generally the frequency range of interest is given by 1/3 octave bands centred between 100 Hz and 5000 Hz. This frequency range may be extended downward to the 63 Hz octave band in large chambers and upwards to the 10000 Hz octave band.

Measurements units used for Transmission Loss are decibels (dB) in octave or 1/3 octave bands. Also TL may be expressed in terms of the single number ratings STC, OITC or R_w . Sound Transmission Coefficient, dimensionless.

3.1 TL measurements methods

A sound wave incident on a test partition separating two adjacent rooms partly reflects back to the source room, partly dissipates as heat within the material of the partition, partly propagates to other connecting structures, and partly transmits into the receiving room.

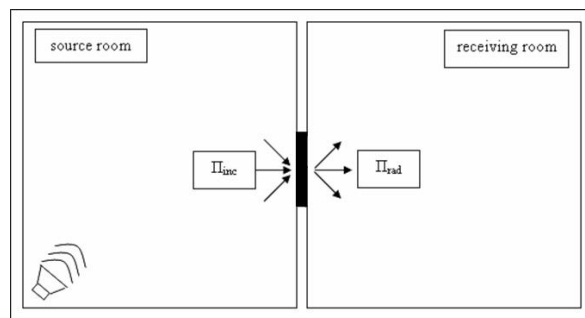


Figure 3.1 – Airborne sound transmission from source room to receiving room

With the assumption, on which pressure method is founded, of diffuse sound fields in both rooms, it is possible to derive a simple relation between the transmission loss and the sound pressure levels in the two rooms. The rooms are called the source room and the receiving room, respectively. In the first room, with strong reverberant characteristics, is a sound source that generates a diffuse sound field measured by the average sound pressure $\langle p_i \rangle$.

In the hypothesis of perfectly diffuse sound field, the intensity per unit area incident on the partition is:

$$I_i = \frac{\langle p_i^2 \rangle}{4\rho_0 c_0} \quad (3.1)$$

The sound power incident on the partition causes it to vibrate and create a sound field in the second room, the receiving room. The rate of transfer of sound energy, i.e. the sound power transmitted through the partition separating the two rooms is:

$$\Pi_t = \tau S \frac{\langle p_i^2 \rangle}{4\rho_0 c_0} \quad (3.2)$$

where τ is the transmission coefficient of the partition of area S .

The rate of energy loss in the receiving room is given by:

$$\frac{d}{dt} \int_{V_2} w_2 dV \quad (3.3)$$

where w_2 is the energy density in the receiving room with volume V_2 and is function of position in the room. In the steady state these two rates will be equal giving rise to the equation:

$$\tau S \frac{\langle p_i^2 \rangle}{4\rho_0 c_0} = \frac{\partial}{\partial t} \int_{V_2} w_2 dV \quad (3.4)$$

If in the receiving room an exponential decay of energy with time constant d is assumed, then the right side of equation (3.4) becomes $d \int_{V_2} w_2 dV$.

With the further assumption that the integral can be replaced by $\frac{V_2 \langle p_i^2 \rangle}{\rho_0 c_0^2}$, where it has been introduced the temporal and spatial average of the transmitted pressure, $\langle p_t \rangle$, the (3.4) can be rewritten as:

$$\tau S \frac{\langle p_i^2 \rangle}{4\rho_0 c_0} = \frac{dV_2 \langle p_i^2 \rangle}{\rho_0 c_0^2} \quad (3.5)$$

Setting:

$$A = \frac{4dV_2}{c_0} \quad (3.6)$$

it results:

$$\frac{1}{\tau} = \frac{\langle p_i^2 \rangle S}{\langle p_t^2 \rangle A} \quad (3.7)$$

thus, taking logarithms, the equation for TL measurements with sound pressure method is obtained:

$$TL = 10 \log \left(\frac{1}{\tau} \right) = Lp_{source} - Lp_{receiving} + 10 \log_{10} \left(\frac{S}{A} \right) \quad (3.8)$$

Special care has to be taken in order to ensure that the only significant sound transmission path between the rooms is by the way of test partition. The pressure methods, in fact, presupposes that all sound energy is transmitted via the test specimen. In practice, the specimen is never the only path, via which sound enters the receiving room. A certain part of the total sound energy measured in the receiving room is always radiated by other room surfaces. This is called flanking transmission.

When using the sound intensity technique, the source chamber has to be reverberant, whereas requirements of receiving room are less stringent.

The incident intensity on the partition can be obtained from the (3.1) whereas the direct measurement of sound intensity on the receiving side of the partition provides enough information to calculate transmission loss without any consideration of the properties of the receiving room, other than the requirement that the reverberant field level there does not invalidate the measurements.

Being the sound intensity a vector quantity defined as the product of sound pressure and particle velocity in the case of sound intensity measurements these two quantities have to be acquired. There are intensity probes where the particle velocity is determined directly using an ultrasonic particle velocity transducer (*p-u probes*), however, the two microphone technique (*p-p*) is the most usual method to determine the one dimensional particle velocity u_x . When using *p-p probes*, the time-averaged particle velocity in direction x is determined by the time-averaged pressure gradient between two microphones using Euler's equation:

$$u_x = -\frac{1}{\rho_0 \Delta r} \int (p_B - p_A) dt \quad (3.9)$$

where Δr is the distance between the microphones A and B , and p_A and p_B are the pressures sensed by the microphones A and B , respectively. Thus, the phase information contained in the pressure signals is fully utilized in the two-microphone intensity

technique. To calculate the intensity, the pressure is determined by the average of the two microphone signals by $(p_A+p_B/2)$.

The distance between the microphones is usually set at $\Delta r = 6 \dots 50 \text{ mm}$, depending on the frequency range of interest. The main assumption of the two-microphone method is that the inherent phase difference between the microphones is negligible. This is realized by selecting two microphones from the production batch, which have as similar a phase response as possible (phase matched microphones).

3.1.1 Reverberation chambers

Reverberation chambers are intended to produce a diffuse sound field. Their design and construction can be optimized to best achieve a diffuse field. Intuitively, its surfaces should be highly reflective, i.e. very hard. Concrete and steel panel are most commonly used for the chamber surfaces. Also, the chamber shape should not be a simple shape, not a cube, sphere or cylinder. Simple shaped rooms have dominant room modes that make the sound field highly dependent on position in the room. Rectangular rooms are common. Optimal dimension ratios for rectangular rooms are given in the Annex D of the standard ISO 3741, that gives guidelines for reverberation chambers design.

Also, rooms with dimensions that are large compared to the longest wavelength of interest are more diffuse than small rooms.

The diffusion of a room increases when the room dimensions are carefully chosen to separate room modes and equalize the frequency response of the room. Diffusion increases as the frequency spacing between room modes decreases and the bandwidth of room modes increases. With regard to frequency spacing, 20 room modes per one-third octave band is a suggested lower limit for a “diffuse” field (Schultz, 1971).

This relation can be translate in the expression:

$$V \geq 4\lambda^3 \tag{3.10}$$

Where the room volume V determines the maximum wavelength λ , or the minimum frequency, for which the sound field can be thought to be diffuse.

The volume of the rooms is then the most important factor to determine the frequency range of use of a facility.

To have 20 room modes in the 100 Hz band, where the lowest frequency is 89 Hz, a room must have a volume greater than 230 m^3 .

3.1.2 Schroeder Frequency

M.R. Schroeder found an empirical relation between the volume and decay rate, d , of a room to determine a cut-off frequency that marks the transition from individual, well separated resonances to many overlapping normal modes. Above this frequency a diffuse field could be expected, the statistical parameters of frequency response curves for all acoustic enclosures are either identical or depend at most from reverberation time, T_{60} .

He showed that for a given room frequency response, when the average frequency spacing between natural modes is less than about one third the bandwidth of a mode, the sound field is diffuse. Below a certain frequency, referred to as the Schroeder frequency of a room, the spacing between natural modes is more than one-third of the bandwidth of a mode.

The Schroeder frequency can be expressed as:

$$f_s = 2000 \sqrt{\frac{60}{Vd}} = 2000 \sqrt{\frac{T_{60}}{V}} \quad (3.11)$$

The previous equation descends from equating the half-power bandwidth B of the resonances:

$$B = \frac{\ln 10^6}{2\pi T_{60}} = \frac{13.81}{2\pi T_{60}} = \frac{2.2}{T_{60}} \quad (3.12)$$

with three times the average asymptotic spacing Δf between resonance frequencies:

$$\Delta f = \frac{c^3}{4\pi V f^2} \quad (3.13)$$

In fact, it results:

$$\frac{2.2}{T_{60}} = 3 \frac{c^3}{4\pi V f^2} \Rightarrow f_s = \sqrt{\frac{3c^3}{8.8\pi}} \sqrt{\frac{T_{60}}{V}} \approx 2000 \sqrt{\frac{T_{60}}{V}} \quad (3.14)$$

The factor 2000, which contains the velocity of sound c in m/s, guarantees that, on average, at least three resonances fall within the half-power bandwidth of one resonance at frequencies above f_s .

This factor, that is unit dependent, can be eliminated by using a cross-over wavelength λ_s instead of a cross-over frequency f_s .

From the Sabine's formula for reverberation time, equation (2.112), it results that:

$$\frac{T_{60}}{V} = \frac{55.26}{cA} \quad (3.15)$$

Where A is the equivalent absorption area. By substituting this relation in the (3.11), and expressing in function of λ_s , it can be achieved that:

$$\lambda_s = \frac{c}{f_s} \cong \sqrt{\frac{A}{6}} \quad (3.16)$$

where the factor 6 is a pure number and λ_s is given in the same unit as \sqrt{A} . In contrast to equation (3.11), equation (3.16) is independent of units. A diffuse field is obtained for wavelengths smaller than λ_s .

Below the Schroeder frequency, or above the Schroeder wavelength of a room, the repeatability and reproducibility decline because of insufficient diffusion.

Expression found for the Schroeder frequency shows that increasing the room volume or increasing the decay rate, i.e. adding absorption, lowers the Schroeder frequency which is advantageous. It must be noted that with larger rooms, atmospheric attenuation contributes significantly to the decay rate of sound of frequencies above 2000 Hz. This violates the assumption of negligible energy loss along the mean free path used for the derivation of the Sabine equation. So, increasing the volume of the chamber extends its operable range to lower frequencies but makes high frequency data less accurate.

With regard to the bandwidth of room modes, they can be increased by adding absorption to the room. This technique is used to increase the bandwidth of low frequency modes, since the modal density is low at low frequencies. Of course this introduces limitations to the diffuseness of the sound field.

3.2 Applicable Standards

This paragraph lists the international standards for laboratory Sound Transmission Loss measurements, including ISO and ASTM standards.

The following standards utilize a pair of reverberation chambers, measurements of the space/time average sound pressure levels in each chamber and a measurement of the reverberation time in the receiving chamber to determine the ratio of the sound energy incident on a test element to the sound energy transmitted through the element (pressure method).

- ASTM E90-04 Standard Test Method for Laboratory Measurement of Airborne Sound Transmission Loss of Building Partitions and Elements.

- ISO 140- 1: 1997 Acoustics - Measurement of sound insulation in buildings and of building elements - Part 1: Requirements for laboratory test facilities with suppressed flanking transmission .

- ISO 140- 2: 1991 Acoustics - Measurement of sound insulation in buildings and of building elements - Part 2: Determination, verification and application of precision data.

- ISO 140- 3: 1995 Acoustics - Measurement of sound insulation in buildings and of building elements - Part 3: Laboratory measurements of airborne sound insulation of building elements.

The following standard utilizes a reverberant source chamber, in which measurements of the space/time average sound pressure levels are conducted, coupled to another chamber, in which sound intensity measurements are performed, i.e. the already introduce intensity method:

- ASTM E2249-02 Standard Test Method for Laboratory Measurement of Airborne Sound Transmission Loss of Building Partitions and Elements using Sound Intensity.

The following standards utilize the sound transmission loss data obtained in accordance with the basic sound transmission loss measurement standard to determine a single number rating for the test element.

- ASTM E1332-90 Standard Classification for Determination of Outdoor-Indoor Transmission Class

- ASTM E413-04 Standard Classification for Rating Sound Insulation

3.2.1 TL standard measurements with pressure-based method

The measurement of the sound transmission loss of a specimen, according with ASTM E-90, is performed in two adjacent reverberation rooms. Between them an opening is present in which the test article can be installed. A diffuse sound field is produced in the source room where an acoustic source emitting a signal with flat spectrum in the frequency range of interest acts.

The measurement is based on:

- The difference in the space/time averaged sound pressure level between the source chamber and the receiving chamber
- A term that accounts for the area of the test specimen

- A term that normalizes the difference based on the total absorption of the receiving chamber. The total absorption is determined from a measurement of the reverberation time in the receiving chamber.

The mathematical relationship has been already given in (3.8), it is rewritten here for the sake of clarity:

$$TL = Lp_{source} - Lp_{receiving} + 10 \log_{10} \left(\frac{S}{A} \right) \quad (3.17)$$

Where:

Lp_{source} = space/time averaged sound pressure level in the source chamber [dB]

$Lp_{receiving}$ = space/time averaged sound pressure level in the receive chamber [dB]

S = surface area of the test specimen [m^2]

A = total absorption in receive chamber with the test specimen in place [metric Sabins, m^2]

The major source of measurement uncertainty in the transmission loss measurement are spatial variations of the sound pressure levels in the reverberation chamber, and spatial/temporal variations of the decay rate in the receiving chamber. These variations are greatest at low frequencies. This uncertainty is reduced by spatial/temporal sampling of these parameters. A sufficient number of sound pressure level and decay rate samples must be obtained to limit the 95% confidence interval on the transmission loss to the following values:

one-third octave bands	intervals amplitude
125 Hz and 160 Hz bands	3 dB
200 Hz and 250 Hz bands	2 dB
315 Hz to 4000 H	1 dB
Table 3.1 – 95% Confidence Intervals amplitudes	

It has also to be evaluated the presence of flanking transmission that is not taken into account in the measurement.

Advantages/Disadvantages to Approach

- + Fast and Simple measurements to perform
- + Less intensive instrumentation requirements
- + Measurements over entire frequency range of interest in one pass
- Test facilities requirements are more extensive
- Isolated test rooms are necessary to measure heavy structures

Test Environment

Two reverberation chambers, each with a minimum volume of 50 m³ coupled through a test opening equal to the size of the test specimen. The transmission loss limit of the test facility and any filler walls used to adapt the test specimen to the facility opening shall be known.

Equipment

- White/Pink noise generator
- Power amplifier and speakers with sufficient acoustic power to generate sound pressure levels in the receive chamber that are at least 10 dB above the ambient sound pressure levels in each test band.
- Microphone(s) with uniform frequency response over frequency range of interest.
- Integrating, averaging sound level meter with 1/3 octave band filtering.
- Level versus time analyzer with reverberation time analysis.

3.2.2 TL standard measurements with intensity-based method

Another standard test method, ASTM E2249-02 has been introduced for evaluating the sound transmission loss of a partition or partition element under laboratory conditions. It differs from the Standard Test Method E90 in that the sound power radiated by the element under test is measured directly using an intensity probe rather than indirectly from the space averaged receiver room sound pressure and the room reverberation time.

This test method is especially useful when the receiver room requirements of ASTM E90 can not be achieved. In this application, one must ensure that errors due to the reverberant sound field in the receiving room are negligible. This can be achieved by using an anechoic chamber as the receiving room or by adding sound absorbing material to the room to reduce the level of the reactive field. Many facilities use as receiving room an anechoic chamber.

In this case, the TL of a specimen is based on:

- The sound pressure level in the source reverberation chamber
- The average sound intensity radiated by the specimen into the receiving chamber
- A term to account for the area of the test specimen

The average sound intensity level in the vicinity of the test specimen, typically at a distance of 10-30 cm, is measured in discrete points in the form of a grid or by manual scanning. The density of the measurement grid is usually 10-50 cm.

The measurement is based on the assumption that the sound field in the source chamber is diffuse, whereas the receiving room has no specific physical requirements for size or absorption condition. The acceptability of the receiving room has to be determined by a set of field indicators that define the quality and accuracy of the intensity estimate. These field indicators depend by the sound intensity measurement technique used, i.e. discrete points or scanning method.

The mathematical relationship to be used to compute the TL of the test partition in each one-third octave band is:

$$TL = \left[Lp_{source} - L_{in} - 6 + 10 \log \frac{S_s}{S_m} \right] \quad (3.18)$$

Where:

Lp_{source} = space/time averaged sound pressure level in the source chamber [dB]

L_{in} = surface averaged transmitted sound intensity normal to the measurement surface [dB]

S_s = surface area of the test specimen or portion of it, contained in the measurement volume [m²]

S_m = total area of the measurement surface [m²]

The constant 6-dB term arises from the fact that the angle of incidence of the energy in the source chamber is random in orientation, and that the sound pressure level in the source chamber is proportional to the total energy incident on the specimen. The integration of a cos term to calculate the energy normally incident on the specimen results in 6 dB difference between the source chamber sound pressure level and the incident sound intensity.

Compared to the ASTM E-90 method, the sound intensity method is less time consuming, if the scanning approach is used, and it is not necessary to measure the reverberation times in the receiving room. However, a disadvantage of the sound intensity method is the frequency limitations. The low frequency limit is due to the phase mismatch between the two microphones. The high frequency limit is caused by the finite distance approximation error.

Advantages/Disadvantages to Approach

- + Test facilities less extensive
- + Point method enables source localization
- + Reverberation time not needed
- + Enables determination of flanking paths
- + Isolation of test rooms less necessary
- Requires more complex instrumentation and data analysis
- May require more than one pass to cover entire frequency range of interest
- Sound-absorbing specimen prohibited

Equipment

- White/Pink noise generator
- Power amplifier and speakers with sufficient acoustic power to generate sound pressure levels in the receive chamber that are at least 10 dB above the ambient sound pressure levels in each test band.
- Microphones with uniform frequency response over frequency range of interest.
- Integrating, averaging sound level meter with 1/3 octave band filtering.
- Two phase-matched microphones with uniform frequency response over frequency range of interest (intensity probe)
- Dual channel analyzer with cross-spectrum analysis and 1/3 octave band filtering.

3.2.3 Single Number Ratings: Sound Transmission Class (STC)

The sound transmission loss of a specimen can be expressed in terms of a single number rating (SNR). The most common rating is the Sound Transmission Class (STC) of the specimen. The STC rating is determined in accordance with the calculation procedures of ASTM E413. The STC rating of a specimen is determined by comparing the 1/3 octave band sound transmission loss data in the bands between 125 Hz and 4000 Hz to a series of standard transmission loss contours. The reference contour is defined in the table whereas the following contours to fit with the experimental data can be achieved by increasing all the value in the table in 1 dB increments until some of the data are less than the shifted reference contour.

The SNR is given by the value of the shifted reference contour at 500 Hz.

<i>Frequency [Hz]</i>	125	160	200	250	315	400	500	630
<i>Contour Value, dB</i>	-16	-13	-10	-7	-4	-1	0	1
<i>Frequency [Hz]</i>	800	1000	1250	1600	2000	2500	3150	4000
<i>Contour Value, dB</i>	2	3	4	4	4	4	4	4

Table 3.2 – Reference sound insulation contour for calculation of Single Number Ratings



Figure 3.2 – STC calculation

If a measured data point is less than the reference contour this is a deficiency; only deficiencies are counted in the fitting procedure. Continue to increase the reference contour values to the highest level that fits the transmission loss data as follows:

- The sum of the deficiencies in all bands is less than or equal to 32 dB
- The maximum deficiency in any band is less than or equal to 8 dB

3.3 Small Acoustic Research Facility (SMARF)

The vibration and acoustic research group of the Department of Aerospace Engineering at University of Naples has recently concluded the design and assembly of a Small Acoustic Research Facility (SMARF), an experimental facility aimed to the measurements of the Noise Reduction and the Transmission Loss between two reinforced concrete reverberant rooms, separated by a septum bringing a window on which the test specimen can be installed. The reinforced concrete walls are about 100 mm thick and ensure high isolation from exterior noise sources

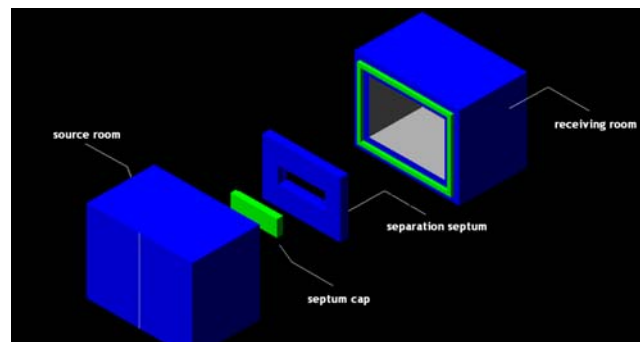


Figure 3.3 – SMARF scheme-



Figure 3.4 – SMARF construction

The source room has been equipped with wheels to open the facility for the installation of the test specimen. The wheels move on a dedicated track ensuring repeatability of the relative positioning of the two chambers and speeding up panels installation procedure. In order to increase isolation from exterior vibrations, the receiving room's backings have been supplied with damping pads.



Figure 3.5 – Details of SMARF construction

The separation septum is made by two layers, respectively 80 mm wood and 30 mm lead allowing to avoid energy passing through it. The contact surfaces between the two chambers are equipped with 10 mm thick rubber strips to minimize structural energy transmission. The locking system is made by 4 steel hinges screwed by nuts.

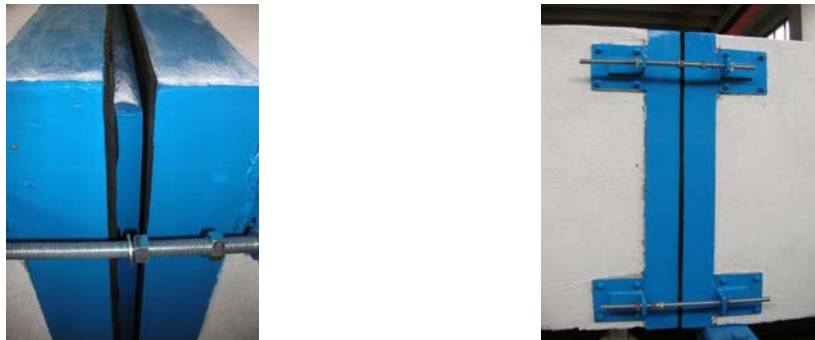


Figure 3.6 – SMARF locking system

The geometrical dimensions of both source and receiving room are given in the following Table 3.3.

Geometrical Characteristic	Source Room	Receiving Room	Chambers' Partition
Internal dimensions [m]	1.40 x 1.04 x 0.75	1.25 x 1.00 x 0.71	---
External dimensions [m]	1.55 x 1.30 x 1.04	1.55 x 1.30 x 1.01	0.10 x 1.04 x 0.75
Total surface [m ²]	5.80	5.00	0.78
Seismic mass [Kg]	2350	2585	---

Table 3.3 - Main geometrical dimensions of the small TL facility

The transmission loss window, in the actual configuration, accommodates flat test articles with dimensions a and b respectively belonging to the intervals (0.590, 0.620) m and (0.190, 0.210) m.

The windows used as lodging has a double side frame that has been designed trying to reproduce a knife-edge support, in order to allow for the panel being simply supported along its edges.

A separation cap, made in similar manner as the separation septum, can be installed between the chambers to provide maximum degree of isolation available.

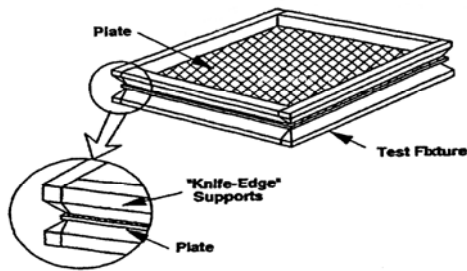


Figure 3.7 – Knife-edge support



Figure 3.8 – SMART septum cap



Figure 3.9 – Panel's installation details

All the measurement phases can be driven from outside without open the facility.

In the receiving room a simple mechanism has been built to allow for microphones positioning. Microphones can be moved in a continue way in the longitudinal as well as

in the vertical direction from outside the facility by using a dedicated hand gear. In the transversal direction, instead, microphones can be mounted at a 50 mm distance one from each other. Some details of the microphones mounting system are presented in the Figure 3.10.

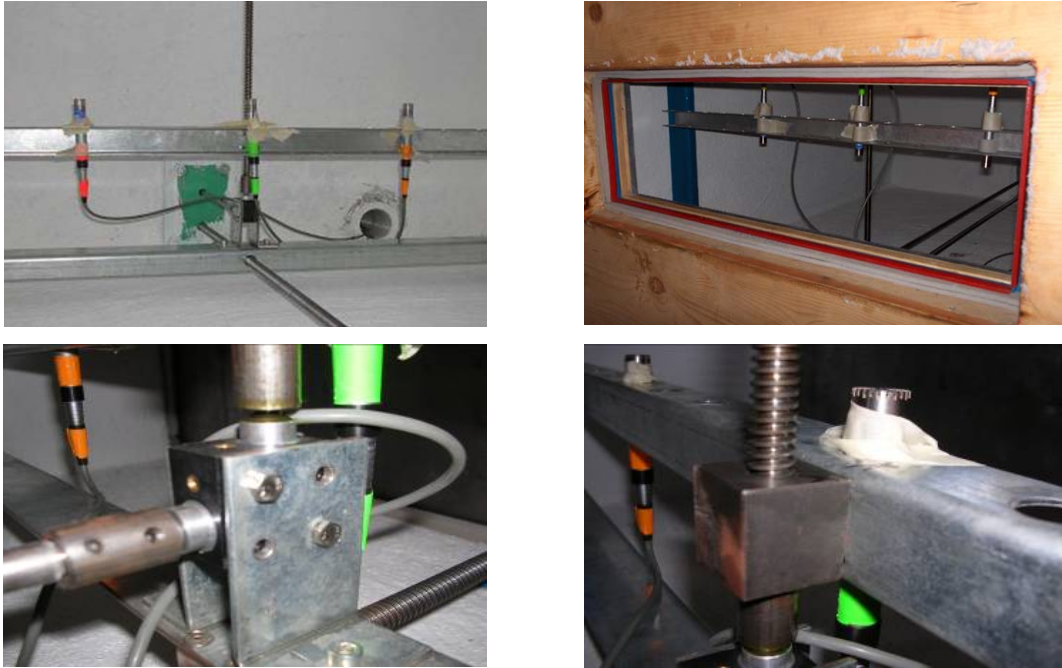


Figure 3.10 – Microphones mounting system

3.3.1 SMARF Validation

Geometrical evaluations and validation measurements have been performed with the aim to identify SMARF measurements limits and frequency range of applicability.

3.3.2 Geometrical dimensions and Standards prescription

The above listed standards for pressure-based sound transmission loss measurements prescribe the use of large rooms. According with ASTM E-90, in fact, the volume of both source and receiving rooms must be 50 m³ or more and the sound absorption in each of the rooms should be made as low as possible to achieve the best possible simulation of the ideal diffuse field condition and to keep the region dominated by the direct field (of the source or of the test specimen) as small as possible. At each frequency, the sound absorption for each room should be no greater than:

$$A = \frac{\sqrt[3]{V^2}}{3} \quad (3.19)$$

where V is the room volume and A is the sound absorption of the room.

Nevertheless, a small TL facility presents several advantages if compared to the standard big facilities, first of all the capability to perform fast and cheap measurements in order to evaluate different candidate solutions.

The problem of using a small facility arises in the low frequency region where it is not possible to assume the sound field to be adequately diffuse.

In the present validation procedure the SMARF minimum operative frequency f_{min} has been calculated on the base of the following relation, according with the already cited equation (3.10)

$$V > 4\lambda^3 \Rightarrow f_{min} > c\sqrt[3]{\frac{4}{V}} \quad (3.20)$$

It descends that the minimum frequency f_{min} where it is possible to perform reliable measurements is around 560 Hz. (one-third octave band centred at 630 Hz).

This result is confirmed by the fact that, if analytical cavity modes and their distribution in one-third octave bands are considered, it results that the lower band in which at least 20 modes occur is the one centred at 630 Hz (see Figure 3.11).

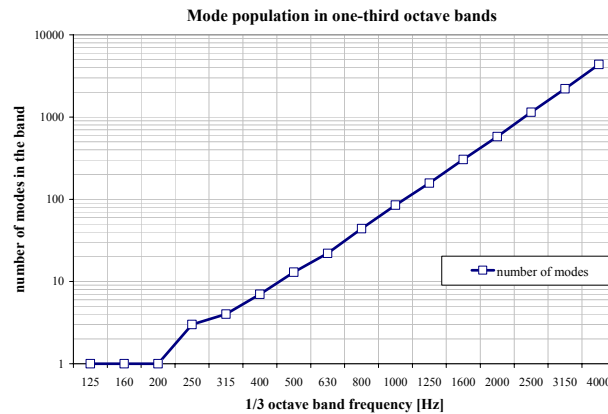


Figure 3.11 – Mode population in one-third octave bands

Another simple geometrical check has been realized on the base of the already cited guidelines for reverberation chambers design given by the ISO 354.

For rectangular rooms it is suggested to avoid that the ratio between two dimensions is an integer and it is stated that ratios $1:2^{1/3}:4^{1/3}$ are often used.

For the SMARF, considering that the smallest dimension of the source room is equal to 0.75 m, such ratios would give for other sides of the room 0.95 m and 1.20 m, that are quite close to the actual values of 1.04 m and 1.40 m.

The same standard also states that the shape of a reverberation room should be such that the following condition is fulfilled:

$$\ell_{\max} < 1.9V^{1/3} \quad (3.21)$$

where ℓ_{\max} is defined as the length of the longest straight line which fits within the boundary of the room, that is, for a rectangular room, its major diagonal. The SMARF dimensions satisfy the imposed conditions for both source and reverberant chambers.

3.3.3 Isolation from external noise sources

The degree of isolation from external noise sources has been assessed by comparing the ground noise levels measured with no source active inside and outside the facility. The results presented in the Figure 3.12 show that internal ground noise is very low and at least 25 dB lower than external ground noise in all the frequency bands analyzed.

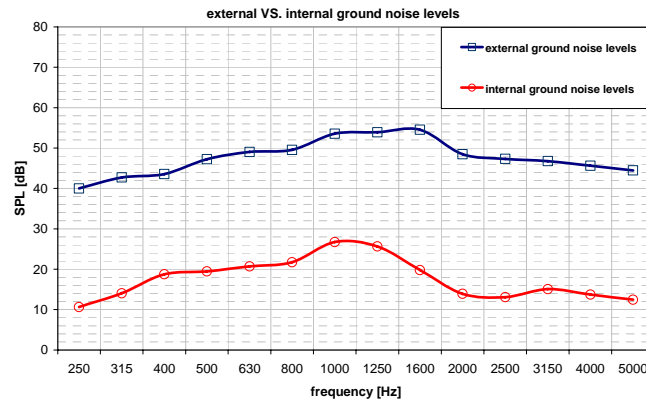


Figure 3.12 – External VS. internal ground noise levels

Furthermore, it results to be verified the prescription, from ASTM E-90 as well as from ISO 3741, that states that, in order to avoid the application of a correction procedure, the background noise levels should be at least 10 dB lower than the sound pressure levels measured in all the one-third octave bands.

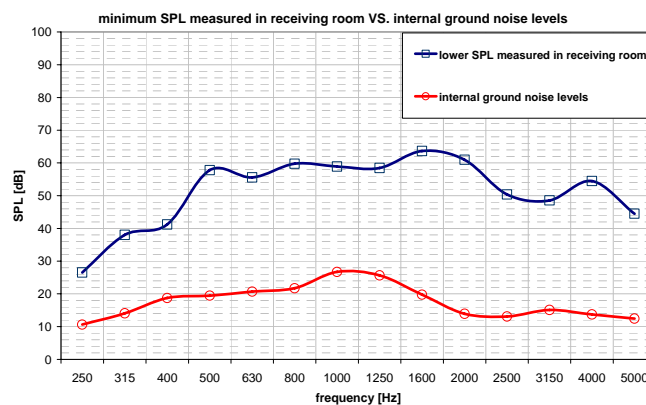


Figure 3.13 – lower SPL measured in the receiving room VS. background noise levels

Another check has been performed placing an acoustic source outside of the facility and measuring the correspondent noise levels nearby the source and inside the facility.

The curves in Figure 3.14 illustrate that in this case differences between sound pressure levels measured inside and outside the facility are even higher than before. Internal noise levels are more than 30 dB lower than external ones in all the frequency bands of interest.

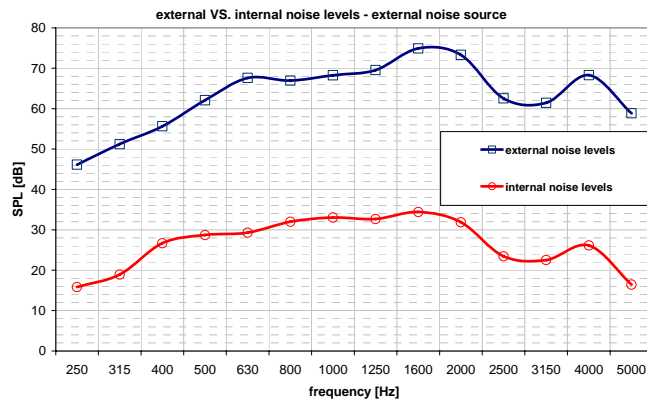


Figure 3.14 – External VS. internal noise levels with external sound source

3.3.4 Flanking Transmission evaluation

The ASTM E-90 prescribes that the possibility of transmission by paths other than that through the test partition should be minimized and that sound pressure levels produced by such flanking transmission should be at least 10 dB lower than the sound radiated into the receiving room by the test partition.

The use of vibration isolators, as it has been for the SMARF, to support one or both rooms is an accepted method to reduce effects from flanking transmission. Furthermore, it is recommended the presence of structural discontinuities between the test specimen and both source and receiving room.

The cited standard suggests also a procedure to identify the limit on the specimen sound transmission loss due to flanking transmission. This procedure is based on the idea to progressively increase the expected transmission loss of the partition by adding soundproofing or shielding materials, measuring at each step the transmission loss, until significant additions to the test partition do not increase anymore the measured TL.

The achieved TL levels constitutes a measurement limit and can be ascribed to flanking transmission. The SMARF's flanking transmission evaluation has been assessed by installing in the transmission loss window a very heavy cap, made by 80

mm wood and 30 mm lead and sealing it with silicon and neoprene rubber. The following Figure 3.15 presents in the discussed sense the measurements boundaries of the SMARF.

If the high measurable noise reduction coincides with the effect of the flanking transmission, a lower limit can be identified by performing a measurement with the TL window open, so that the achieved noise reduction is uniquely due to the characteristics of the facility. It can be noted that the measured NR in these two limit conditions differ of more than 30 dB in the one-third octave bands above 315 Hz.

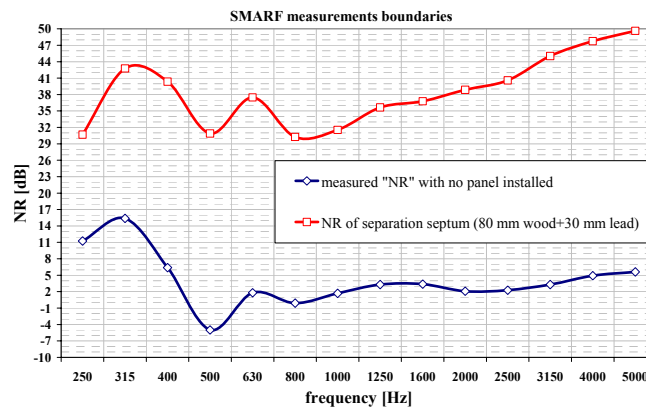


Figure 3.15 – SMARF measurements boundaries

3.3.5 Sound field diffuseness evaluation

The uniformity of the sound field in the source room has been investigated evaluating the ASTM E-90 and ISO 3471 prescriptions as well as via experimental measurements.

According with the ISO 3471, the sound field is diffuse if it results:

$$T_{60} > \frac{V}{S} \quad (3.22)$$

where T_{60} is the reverberation time of the room, V is the volume and S is the total surface, where the minimum volume V is related to the lower one third octave band frequency by relations in the Table3.4

One third octave band lower centre frequency [Hz]	Minimum reverberant room volume [m ³]
100	200
125	150
160	100
> 200	70

Table3.4 – Relation between minimum room volume and lower one third octave band of analysis

For the SMARF dimensions of the source and receiving rooms, it results that the reverberation time has to be bigger than 0.2 that is a very small value. Therefore, the relation in equation (3.22) is verified for all the frequency bands of interest (i.e. for one third octave bands higher than 500 Hz). The same ISO standard describes also a procedure for the room qualification to be applied when the previous one should not be satisfied. The cited procedure is based on sound pressure level measurements in at least 6 different locations, positioning the sound source at a distance not less than $\lambda/2$ from the room walls and microphones at a distance from the source bigger than:

$$d_{\min} = 0.08 \sqrt{\frac{V}{T_{60}}} \quad (3.23)$$

The resulting sound pressure levels must have a standard deviations contained in the limits indicated in the following Table 3.5.

Octave band centre frequency [Hz]	One third octave band centre frequency [Hz]	Maximum allowable standard deviation [dB]
125	100 to 160	1.5
250 and 500	200 to 630	1.0
1000 and 2000	800 to 2500	0.5
4000 and 8000	3150 to 10000	1.0

Table 3.5 – Maximum Standard Deviation of SPL

Applying the explained procedure, the standard deviation of measured sound pressure levels has been calculated at 8 positions in the source room. It has been found that, even not perfectly following calculated limits, as it could be expected considering the small room dimensions, the standard deviation remains under 1.5 dB for one-third octave frequency bands above 400 Hz (see Figure 3.16).

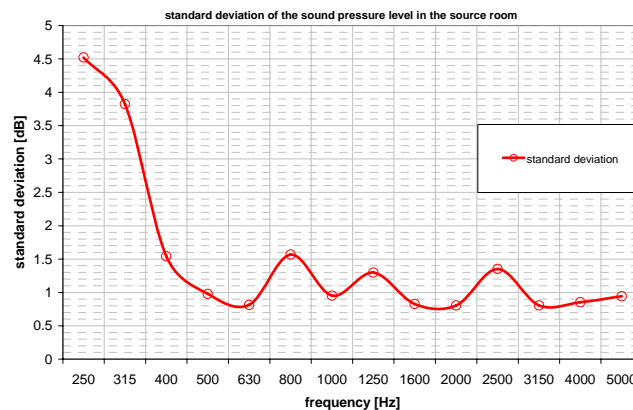


Figure 3.16 – standard deviation of SPL in the source room

The ASTM E-90 proposes a different procedure in order to determinate diffuseness of sound field. First of all it imposes that the direct sound field from the source at the test partition, or the nearest microphone has to be at least 10 dB below the sound pressure level of the reverberant field.

This condition is verified if the distances r between a single source and the microphones and test partition satisfy the relationship:

$$r \geq \frac{1}{4} \sqrt{\frac{10A}{\pi}} \quad (3.24)$$

with A sound absorption in the room. For the SMARF, calculating A with the Sabine's formula on the basis of the measured reverberation time, it can be achieved that $r = 0.12 \text{ m}$. Then the ASTM E-90 identifies the following limits to be respected from the 95% confidence intervals calculated on SPL spatial average in the rooms.

One third octave band centre frequency [Hz]	95% confidence limits [dB]
100 to 160	± 3
200 and 250	± 2
315 to 4000	± 1

Table 3.6 – 95% confidence limits of SPL

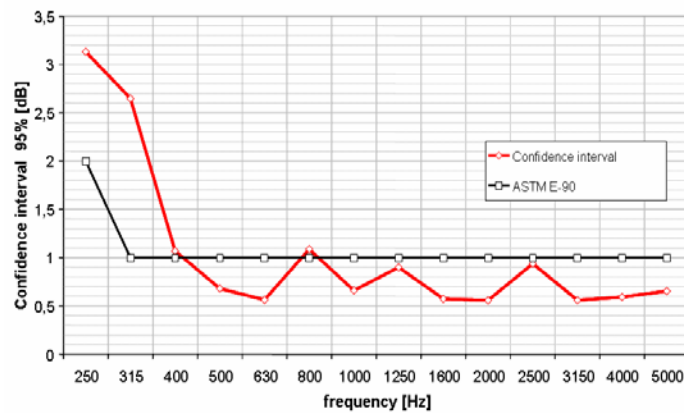


Figure 3.17 – 95% confidence interval of SPL in the source room

Another check has been performed with regard to the spatial distribution of the acoustic load over the test panel. Sound pressure levels have been measured at 24 different positions close to the panel from the source side.

Achieved result confirmed that, in the low frequency range sound pressure levels are low because the sound source is not able to input enough acoustic energy and the sound field is characterized by a modal behaviour. In the following Figure 3.18, it is evident

the presence of standing waves that determine a non homogeneous distribution of sound pressure on the panel at 100 Hz.

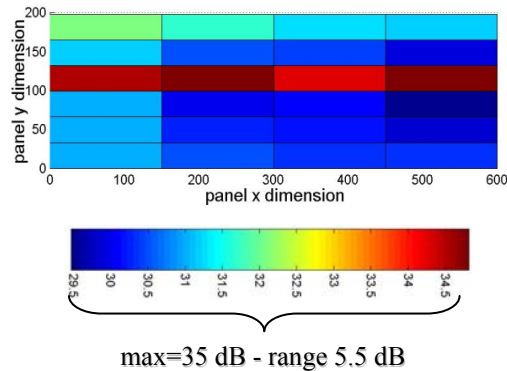


Figure 3.18 – Spatial distribution of the acoustic load on the panel at 100 Hz

In the high frequency region, instead, higher levels are obtained and the differences between positions are less than 1 dB, as it can be seen from the Figure 3.19.

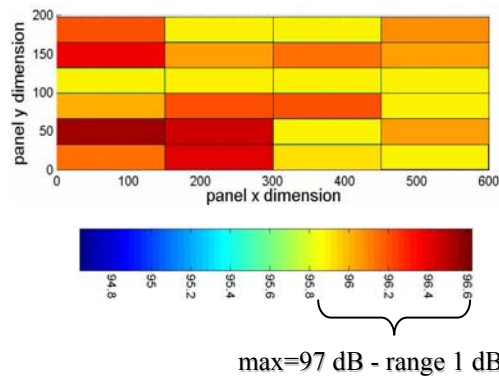


Figure 3.19 – Spatial distribution of the acoustic load on the panel at 4000 Hz

3.3.6 Reverberation Time calculation

One of the most important parameters in the calculation of sound transmission loss is the reverberation time T_{60} , from which the equivalent absorption area A of the receiving room can be derived. Once A is known, the TL can be estimated starting from Noise Reduction measurements.

When a sound source operates in an empty enclosed space, neglecting the absorption of the air, the level to which reverberant sound builds up, and the subsequent decay of reverberant sound when the source is stopped, are governed by the sound absorbing characteristics of the boundary surface of the enclosure.

As already seen, the Sabine's formula relates the absorption characteristics of a volume to its reverberation time via an inverse proportional law.

ISO 354 standard defines reverberation time as the necessary time to allow the acoustic pressure to decrease by of 60 dB after the source has stopped and presents two possible approaches for T_{60} estimation, the interrupted noise methods and the integrated impulse response method.

The decay curve obtained with the interrupted noise method is the result of a statistical process, and averaging several decay curves or reverberation times measured with different combinations of microphone/loudspeaker position is mandatory in order to obtain a suitable repeatability.

The integrated impulse response method is deterministic and not suffers by statistical deviations neither any averaging is necessary. Nevertheless, because it requires more sophisticated instrumentation and data processing with respect to the interrupted noise method, it is less used.

The reverberation time of the SMARF receiving room has been estimated applying the interrupted noise method.

A loudspeaker emitting a sound with flat frequency spectrum (white noise) in the frequency range 0-12800 Hz has been positioned in two different locations in the receiving chamber taking care that the excitation signal was long enough to produce a steady-state sound pressure level in all frequency bands of interest, i.e. one third octave bands between 250 and 10000 Hz, before it was switched off.

A typical time signal recorded is illustrated in the following Figure 3.20

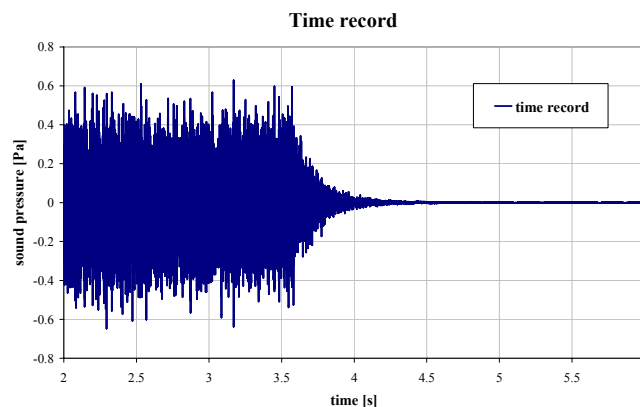


Figure 3.20 – Time signal recorded for reverberation time calculations

Microphones have been placed in 6 different positions in the chamber and sound pressure, as a function of time, has been recorded, ensuring that time signal duration could allow for later decay estimates.

Two approaches have been used for processing measured data.

The first approach has been implemented through a MATHCAD code that splits the time signal in several time blocks.

Each time block contains a part of the pressure decay curve. Operating the Fast Fourier Transform (*FFT*) on each block, it is possible to individuate the time decay and the T_{60} per each frequency band. The final reverberation time can be estimated averaging on each frequency band the reverberation times obtained, see Figure 3.21.

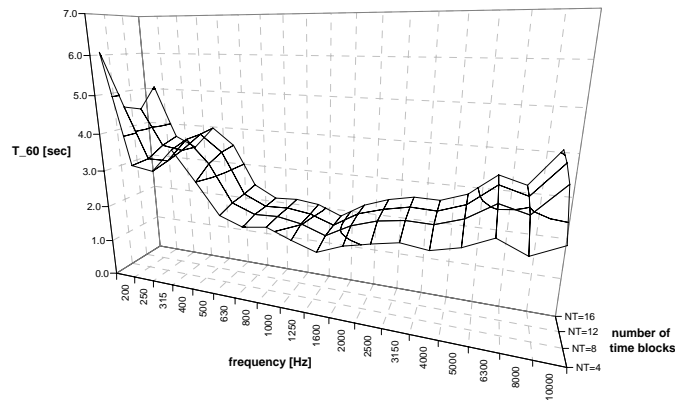


Figure 3.21 – Calculated T_{60} as function of number of time blocks, NT

This method presents some limits, related to the use of a constant bandwidth *FFT*. The frequency resolution Δf of the *FFT* is related to the time length T of each block. To increase the number of block, that is to increase the accuracy of the reverberation time estimate, means to decrease their time length that causes a lower frequency resolution of the performed analysis.

Thus, this method works well at high frequency, where the bandwidth of each one-third octave band is higher, but it estimates the reverberation time using very few samples in the low frequency bands.

The other approach is based on a MATLAB procedure that implements a one-third octave bands filter bank. The filters used are Butterworth passband filters, designed according to the Order-N specification of the ANSI S1.11 standard (Specifications for Octave-Band and Fractional-Octave-Band Analog and Digital Filters, 2004).

The measured time signal is given input to the filter bank, whose output are M time traces (M is the number of bands used for the analysis) each having frequency content only in a single one-third octaves band.

In the following Figure 3.22 are depicted some of the implemented one-third octave passband filters.

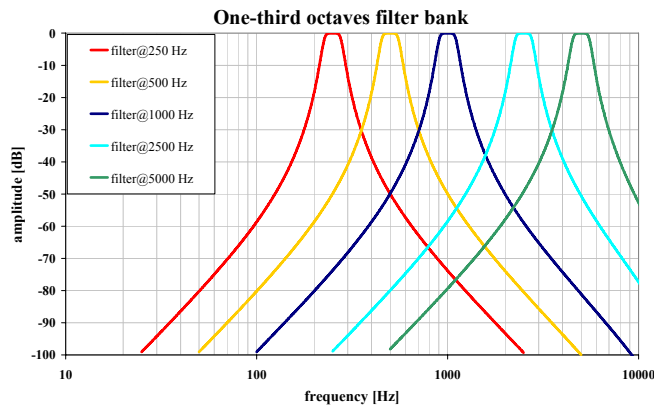


Figure 3.22 – One-third octave filter bank complying ANSI S1.1-1986

As example, in the Figure 3.23 the plot of a time signal filtered with a passband one third octave filter centred at 1000 Hz is drawn.

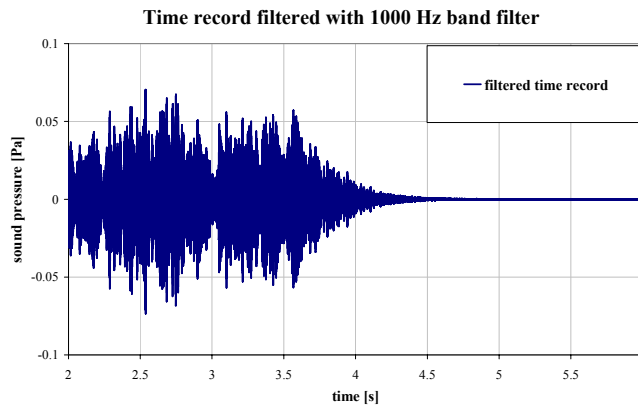


Figure 3.23 – Time signal filtered with 1000 Hz band filter

For each filtered trace the reverberation time T_{60} in the band is estimated from the decay rate achieved by means of an Hilbert transform of the trace (see Figure 3.24).

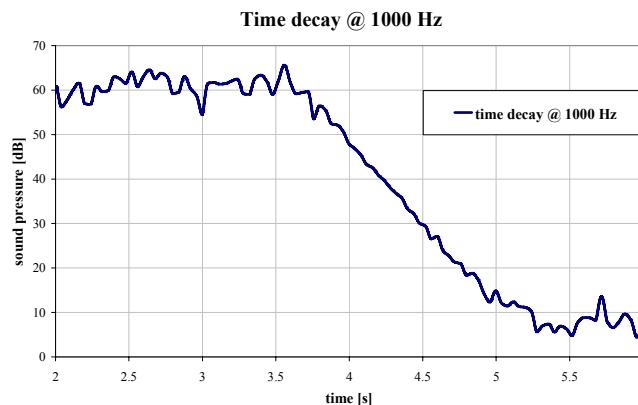


Figure 3.24 – Time decay at 1000 Hz

Details on use of Hilbert transform can be found, for example, in Thrane et alii (1994). An Application of this transform to damping prediction in the high frequency

region, where high modal density do not allow for modal techniques, can be found in Velotto Romano et alii (2005).

The latter method looks to be more reliable of the previous one also for T_{60} estimates in the low frequency band.

In the Figure 3.25 average reverberation time assessed is bounded by minimum and maximum values of its 95% confidence interval.

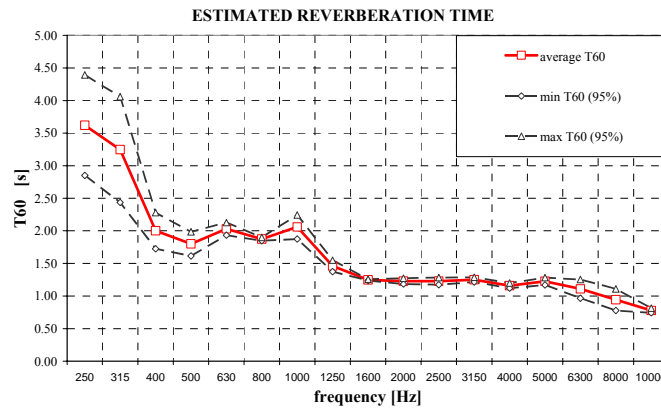


Figure 3.25 – Comparison between T_{60} estimates

On the basis of T_{60} , the equivalent absorption area of the receiving room, A , and then the correction factor, $10\log(S/A)$, needed to obtain the TL from measured Noise Reduction, as defined in equation (3.17), have been calculated for each one-third band (Figure 3.26).

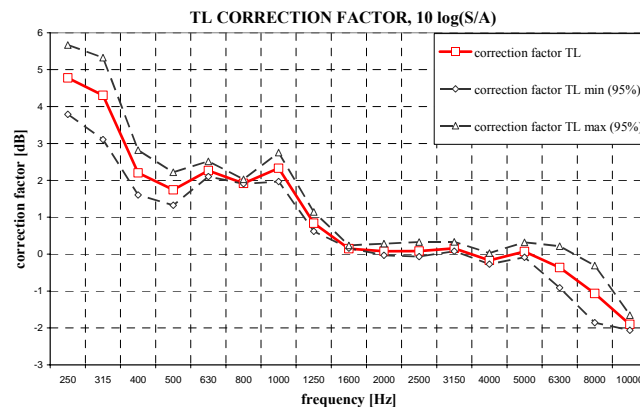


Figure 3.26 – Correction factor for calculate TL from NR measurements

3.4 Test procedure

The excitation system consists of a mobile loudspeaker, type RCF D5076, that can generate white or pink noise in the frequency range 0-25600 Hz. In order to reduce the effect on measurements of the direct field radiated from the loudspeaker, it is usually

located into a corner of the source room. The acquisition has been made using Brüel&Kjær's 1/2" externally polarized microphones, type 4190, whose operative frequency range is 31.5-20000 Hz.



Figure 3.27 – Loudspeaker and microphones used for the acquisition

One microphone has been placed in the source chamber, to measure the acoustical load on the panel, so that the incident pressure level can be estimated. This microphone has been placed in correspondence of the centre of the test panel, at a distance of 200 mm from its surface and at a height of 350 mm from the source chamber's ground. The choice to have a single microphone is related to the lack in the source chamber of a microphone positioning system that could be driven without open the facility. However, as already shown, the standard deviation of the SPL in the source chamber is low (less than 1.5 dB for one-third octave frequency bands above 400 Hz)

In the first phase of the test campaign, in order to assess variability of the sound field in the receiving room in test conditions, measurements have been made using three microphones at two distance from the panel, 190 mm and 300 mm, and at seven different heights, i.e. each 60 mm between 150 and 510 mm from the chamber's ground surface, as depicted in the following Figure 3.28, (Marulo, Polito, Paonessa, 2006).

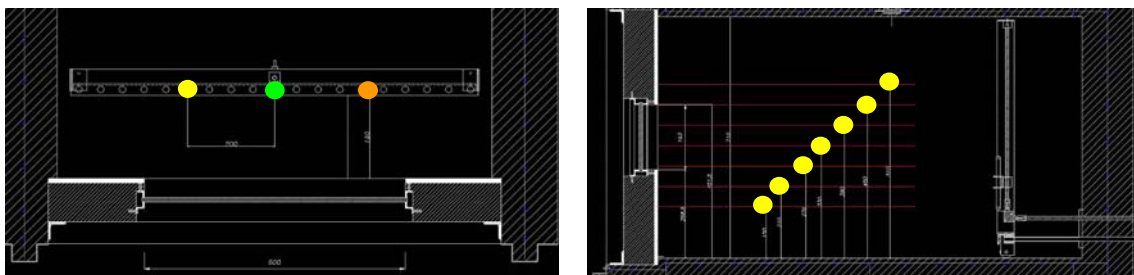


Figure 3.28 – Microphones positions in receiving room

In this configuration, pressure data in $2 \times 3 \times 7 = 42$ measurement positions were acquired. However, 95% confidence intervals calculated on achieved Noise Reduction showed to be very narrow, less than 1 dB, that induced to perform a sensitivity analysis about the possibility to reduce measurements positions. With this approach the final number of measurements positions that have been identified to be used for the later tests

has been fixed equal to 8. In fact, two microphones have been used and positioned at 2 different distances from the panel's surface, 190 mm and 300 mm, and at 2 different heights, respectively 330 mm and 390 mm. By using the reduced number of sensor, the 95% confidence interval achieved is lower than 2 dB, that confirm the repeatability of the test procedure and the diffuseness of the sound field in the receiving room in the medium-high frequency range. The NR calculated on the base of pressure measurements performed at different positions has a small scattering.

In the following Figure 3.29, 95% confidence intervals achieved respectively with 42 an 8 measurement positions for a generic panel tested are presented.

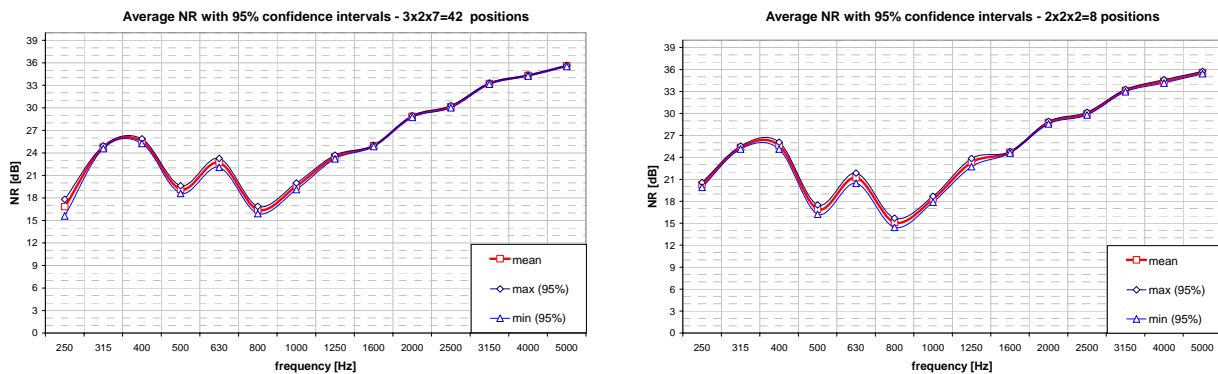


Figure 3.29 – 95% confidence intervals on NR calculated on 42 (a) and 8 (b) positions

In the phase of validation and assessment of SMARF behaviour, the analysis frequency range was fixed in 0-6400 Hz for signal generation and 250-5000 Hz, in one third octave bands, for signal acquisition. Later tests have been performed by generating in the source chamber white noise with frequency content in the range 0-12800 Hz and measuring the NR for in the one-third octave bands belonging to the interval 250-10000 Hz. Typical results obtained are presented in Figure 3.30.

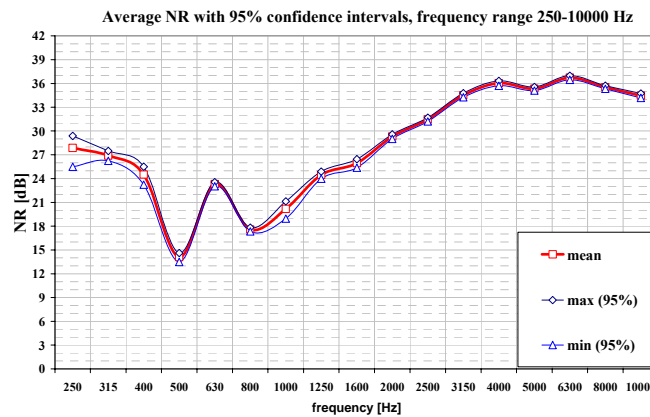


Figure 3.30 – 95% confidence intervals on NR in the range 250-10000 Hz

3.5 Experimental Results

Noise Reduction measurements have been conducted on a series of aluminium alloy and composite aerospace panels, whose approximate dimensions were 600x200 mm. Some of the composite panels testes had a layer of a different viscoelastic material embedded in the middle of their stacking sequence.

The idea to cocuring viscoelastic damping materials in the composite material structure to increase the damping and acoustic performance of the structure is, in fact, one of the solutions that are actually investigated with the aim to increase acoustical performances of composites. In this hybrid approach, the dominant mechanism of damping is the shear induced between the damping layer and the fibre reinforced composite layers. The trade-offs in using damping layers are a slight reduction in stiffness and a small increase in the weight of the composite system. It is required to balance the amount of damping capacity needed, and the penalties in stiffness that can be allowed.

In the following Table 3.7 geometrical and mass characteristics of the tests panels are presented. Preliminary results of the test campaign were presented in Polito et alii, 2007. It is worth to notice that composite panels average weight is 490 g, close to the weight of the aluminium panel 1.5 mm thick.

This is particular important in order to be able to compare acoustic performances of solutions having the same surface density.

Test Panel	Dimensions [mm]	Thickness [mm]	Weight [g]
Aluminum	610 x 203	0.5	170
Aluminum	609 x 203	1.0	345
Aluminum	610 x 203	1.5	511
Aluminum	609 x 203	2	681
CFRP 1	610 x 204	2.4	460
CFRP 2	609 x 203	2.6	486
CFRP 3 (*)	610 x 203	2.6	490
CFRP 4 (*)	610 x 201	2.6	485
CFRP 5 (*)	610 x 203	2.6	482
CFRP 6 (*)	610 x 203	2.6	490
CFRP 7 (*)	609 x 203	2.9	494
Table 3.7 – Test panels characteristics			

The panel CFRP 1 is a bare composite panel, all the other CFRP panels have a layer of a different viscoelastic material embedded.

The layer thickness is 0.2 mm for all these panels except CFRP 7 that has been realized with a thicker damping layer (0.5 mm).

The symbol (*) in the Table 3.7 represents the fact that for each of the indicated configurations, three nominally identical panels have been realized and tested. These panels, being obtained from the same large laminate, should not suffer of any manufacturing difference due to the production process.

In the Figure 3.31 measured Noise Reduction behaviour in the frequency range 250-10000 Hz is presented for all the aluminium panels tested.

In the Figure 3.32 is depicted the NR (average NR, in case of more samples available) of the composite panels obtained in the same frequency range.

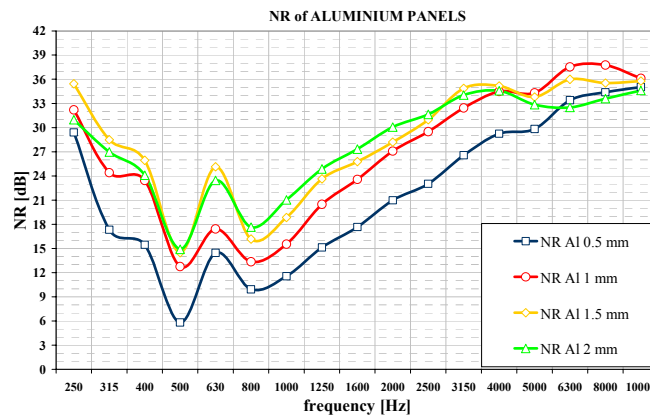


Figure 3.31 – Average NR of Aluminium panels

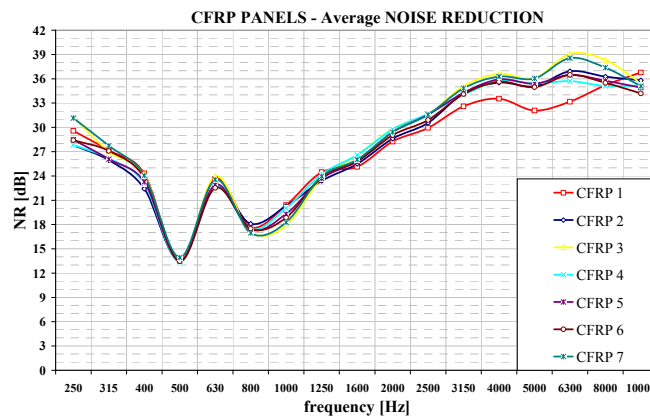


Figure 3.32 – Average NR of Composite panels

From the previous graph it can be seen that major differences between bare composite panel, CFRP 1, and damped ones occur for frequencies above 2500 Hz but it is not simple to appreciate measured differences at lower frequencies.

For the sake of clarity it must be said that damping materials tested are designed for aerospace applications, thus their effectiveness at ambient temperature is low, as it can be seen from Figure 3.33.

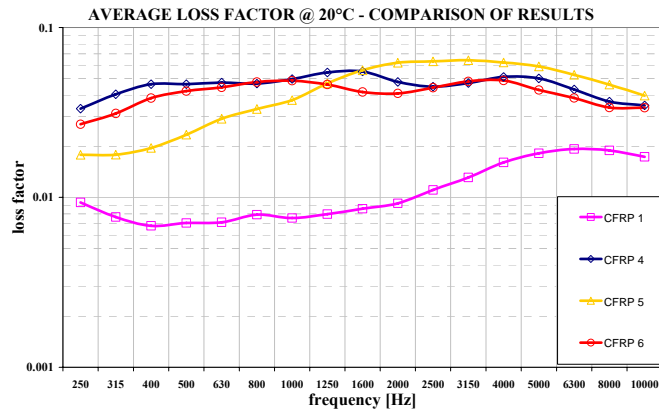


Figure 3.33 –Average Loss Factor @ 20°C

In the Figure 3.34 the Noise Reduction measured for the three different samples available for panel CFRP 7 are compared. It can be seen that the curves are very close, that indirectly confirms the repeatability of the tests performed in the SMARF.

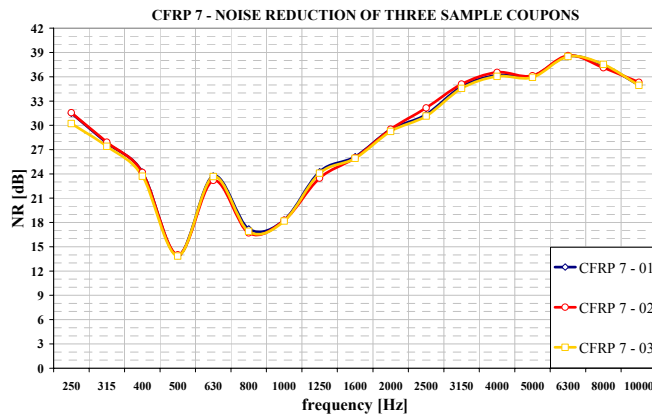


Figure 3.34 –NR of the three CFRP 7 samples coupon

In the following Figure 3.35 and Figure 3.36 results achieved from NR measurements performed with a lapse of time (8 months) on the same test articles (respectively CFRP 5 and CFRP 6) are compared.

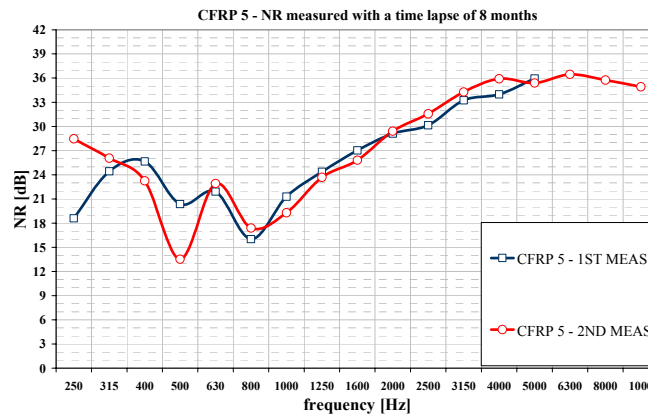


Figure 3.35 –NR measured on CFRP 5 with a lapse of time of 8 months

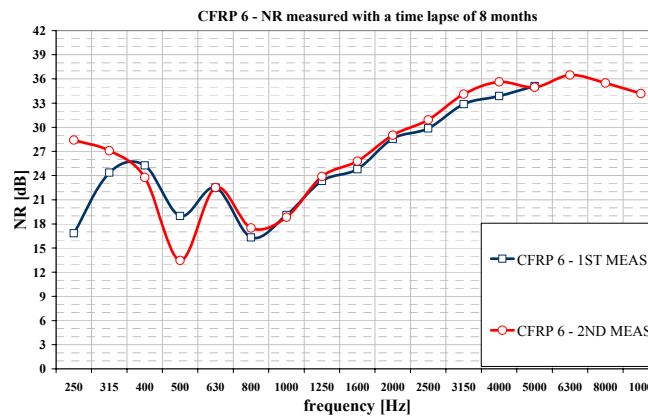


Figure 3.36 –NR measured on CFRP 6 with a lapse of time of 8 months

It has to be noted that former measurements were performed in the frequency range 250-5000 Hz.

Some differences in the low frequency range can be appreciated for both panels. These can be addressed to the mounting system of the panel in the TL window that has been improved during the time elapsed and to the damping mounts introduced in the receiving chamber of the SMARF.

The transmission loss of the panels can be achieved from measured Noise Reduction levels adding the correction factor $10\log(S/A)$, calculated on the base of reverberation time measurements.

In the Figure 3.37 the TL obtained for the Aluminium panels 0.5, 1 and 2 mm thick is presented.

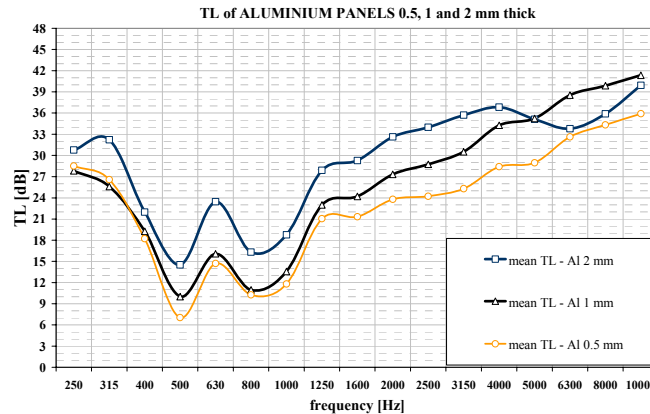


Figure 3.37 – Average TL of Aluminium panels

It can be noted that in the low frequency range, as expected, sound field is not adequately diffuse, so that measurements are strongly influenced by modal behaviour of the acoustical volumes, characterized from the presence of standing waves.

In the medium frequency range, for frequencies above 1000 Hz, the Transmission Loss follows the mass law, having a linear behaviour with a slope of 6 dB per octave. The Figure 3.38 illustrates the results obtained for 1 and 2 mm thick aluminium panels compared with mass law calculated under the hypothesis of diffuse incidence.

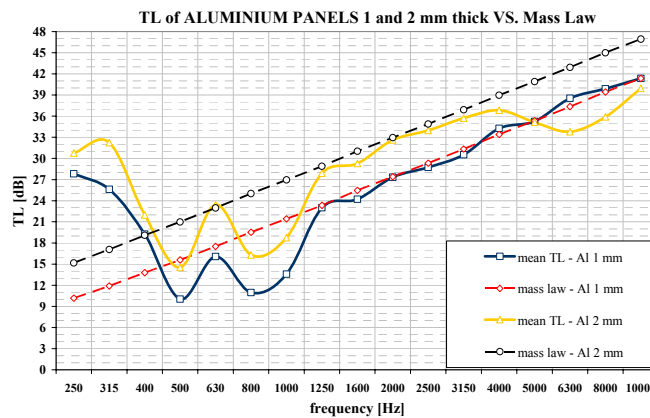


Figure 3.38 – Average TL of Aluminium panels 1 and 2 mm thick with mass law

The 2 mm thick panel shows a decrement of the TL in the 6300 Hz one third octave band. This results is theoretically justified with the occurrence of the critical frequency, f_c , where velocity of free bending vibration of the panel equals speed of sound. At this frequency, the panel is transparent to the acoustic radiation: all the incident sound is transmitted through the panel.

For an aluminium panel 2 mm thick, the critical frequency results to occur around 6000 Hz:

$$f_c = \frac{c}{2\pi} \sqrt{\frac{\rho h}{D}} \approx 6000 \text{ Hz} \quad (3.25)$$

where c is the speed of sound, ρ is the density of the panel, h is the thickness and D is the bending stiffness.

The TL behaviour of the 1 mm panel, instead, is increasing in all the frequency range of analysis, being its critical frequency at 12000 Hz.

It can be found that analogue behaviour is followed by the 1.5 mm thick panel, whose f_c is around 8000 Hz, whereas the 0.5 mm panel's one is at 24000 Hz, well beyond the analysis frequency range, see Figure 3.39.

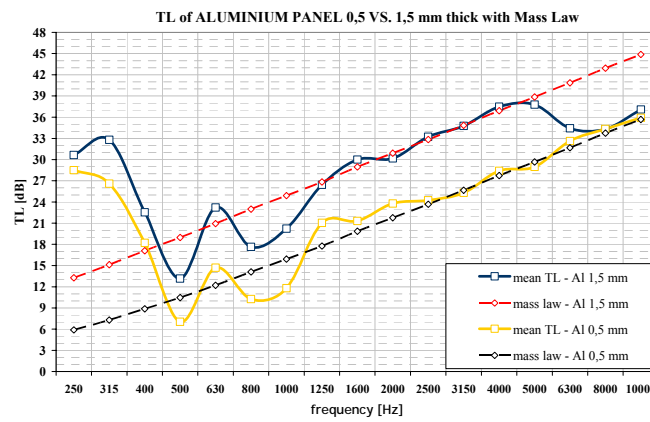


Figure 3.39 – Average TL of Aluminium panels 0.5 and 1.5 mm thick with mass law

4 Numerical Models

The present chapter deals with the FE models built in order to simulate the vibroacoustic behaviour of aerospace structures. Two types of FE models have been realized, that is flat metallic and composite panels and flat panels coupled to acoustic enclosures. Some of the composite panels have been modelled with a damping layer embedded in the centre of their stacking sequence.

The modelling choices made are discussed in the following paragraphs.

4.1 FEM models mesh sizing

The use of composite materials for aerospace structures poses some questions regarding FE modelling issues.

It is well known that the first task in a frequency response analysis using finite element is the correct sizing of the mesh.

A rule of thumb might be:

$$\Delta \leq \frac{\lambda}{4} \quad (4.1)$$

with Δ being the minimum length of the mesh element and λ the smallest wavelength of the propagating wave, which depends on the highest frequency considered.

4.1.1 Isotropic plates

For an isotropic material and a uniform plate, there are always three types of propagating waves, that is extensional, shear and flexural wave (see, for example, Cremer and Heckle, 1988).

Extensional waves are pure longitudinal waves in which the direction of the particle displacements coincides with the direction of the wave propagation.

The propagation velocity c_l of such waves is constant and can be found from the relation:

$$c_l = \sqrt{\frac{E}{\rho}} \quad (4.2)$$

where E is the Young modulus that represents the longitudinal stiffness of the material, ρ is the density and the subscript “ l ” indicates the longitudinal character of this type of wave. This velocity increases with increasing stiffness, decreases with increasing density and do not depend by the frequency.

In solids bodies, because of their characteristic to be able to resist to changes in shape, shear stresses are present. Because of shear stress, transverse wave motion can occur, where the direction of propagation is perpendicular to the direction of the displacement.

The propagation velocity c_t of such waves is similar to the one of extensional waves, with the difference that the shear stiffness G replaces the extensional stiffness E .

The two quantities, E and G , are related by the Poisson modulus ν .

$$c_t = \sqrt{\frac{G}{\rho}} = \sqrt{\frac{E}{2\rho(1+\nu)}} \quad (4.3)$$

Flexural or bending waves are the most responsible for sound radiation. They are quite different from the previous ones as regards their formulation that involves a fourth order partial differential equation. Furthermore, the bending wave velocity is not only dependent on the material (like longitudinal and shear waves) but also on the thickness of the plate and on the frequency. Higher-frequency waves travel faster than lower-frequency waves. These differences in speed cause spreading or dispersion of wave packets. In other words, for flexural waves the group velocity, that is the speed of the wavepacket and the phase velocity, that is the speed of the individual waves, are different.

The phase velocity of a bending wave can be expressed in a mathematical form by the following relation (already introduced in chapter 2):

$$c_b = \sqrt[4]{\frac{\omega^2 D}{\rho_s}} \quad (4.4)$$

where D is the flexural stiffness and ρ_s is the surface density.

Being spatial variations of waves better represented in terms of phase change per unit distance, it is often useful to think in terms of wavenumber $k=\omega/c$ and to express the dispersion phenomenon in terms of dispersion curves $k=f(\omega)$.

By substituting $k=\omega/c$ in the equations (4.2)-(4.4) it results that for an homogeneous material:

$$k_l^2 = \frac{\rho\omega^2}{E}; k_s^2 = \frac{2\rho(1+\nu)\omega^2}{E}; k_b^2 = \sqrt{\frac{12\rho(1-\nu^2)\omega^2}{Eh^2}} \quad (4.5)$$

4.1.2 Orthotropic plates

For a laminate of orthotropic thin layers these formulas are no longer valid, because it is necessary to introduce more engineering constants and the plate it is not uniform. Moreover, new types of propagating wave may cut-off or appear at certain frequencies.

Shorter (2004) formulated a spectral finite-element method to calculate the dispersion properties of the first few wave types of a given laminate. A one-dimensional finite-element mesh is used to describe the through-thickness deformation of the laminate, and the dispersion equation for plane-wave propagation is formulated as a linear algebraic eigenvalue problem in wave number at each frequency of interest.

Barbieri and his co-authors (2007) extended the Shorter's approach introducing the use of a three-dimensional orthotropic stress-strain relationship according to generalized Hooke's law and considering a reference transformation of the arbitrary orientation of a single lamina.

With the described approach, wavelength curves can be readily obtained from dispersion curves, so at maximum frequency of interest the correct sizing of numerical mesh for modelling composite materials can be found.

In the following Figure 4.1 are illustrated the wavelength curves achieved for the composite panel modelled. Once fixed the maximum frequency of interest, from this graph the smaller wavelength at that frequency can be calculated and consequently it is possible to size the mesh using the criterion (4.1).

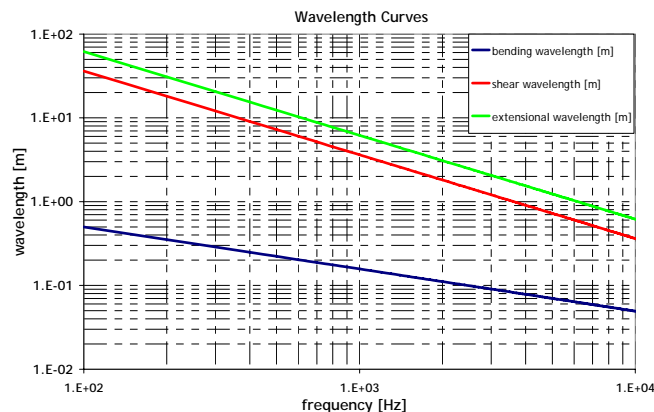


Figure 4.1 – wavelength curves for the composite panel modelled

As discussed in chapter 2, a very important frequency in assessing the acoustic behaviour of a panel is the critical frequency, at which the bending wave phase velocity equals the speed of sound in the propagation medium.

For an homogeneous panel, f_{crit} can be calculated from the equation (2.4).

The results achieved on dispersion curves, instead, can be used to calculate the critical frequency of a given composite panel.

The speed of sound, once known the medium and the temperature, can be considered constant (e.g. in air, at $20^{\circ}C$, it results $c=343\text{ m/s}$), thus, the sound wavelength can be easily achieved as $\lambda_{sound} = c/f$ and plotted in the same graph as the structural wavelength curves.

Looking at the intersection between the curve of the sound wavelength with the one of the structural propagation mode with lower phase velocity, the critical frequency can be assessed. For the modelled composite panel, it results: $f_{crit}=4100\text{ Hz}$.

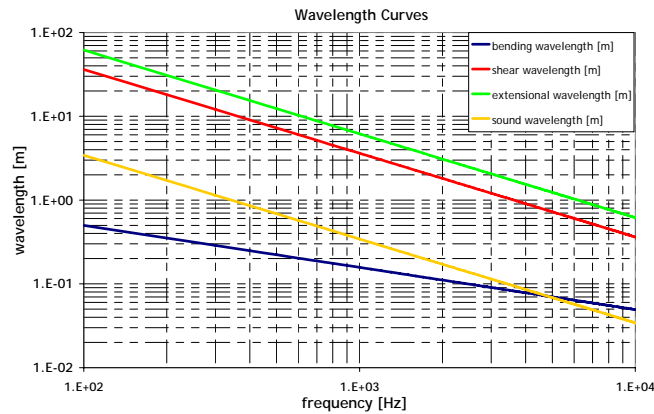


Figure 4.2 – wavelength curves to determine the panel’s critical frequency

4.2 FEM modelling approaches for damping treatments

FE modelling of constrained or embedded damping treatments poses some threats. The classical laminated plate theory, in fact, does not allow a proper representation of boundary conditions of the viscoelastic and the constraining (upper) layer and provides a constant shear stress through the plate thickness (Plouin and Balmes, 1999).

To better represent the shear stress behaviour, two main strategies have been considered in last years: building higher order shell models or connecting multiple elements accounting for the spatial distribution of the damping treatment.

The main problem with the higher order element approach is that developing good shell elements is very difficult so that most developments for sandwiches will not perform as well as state of the art shell elements. The multiple element strategy is also the only available for immediate implementation into commercial FEM software.

In literature, the spatial modelling of the treatment has been approached using three methods, all based on a layered assembly of shell and brick conventional finite elements. All these models use a solid element for the viscoelastic core whereas the skin plates are modelled using shell or brick elements (Moreira and Rodrigues, 2004).

Lu and his co-authors in 1979 developed a model where the translational degrees of freedom of the plate were connected to the brick one by means of rigid links, Figure 4.3, model 1.

Johnson and Kienholz, in their cited work, imposed an offset of half of the plate thickness to the plane in contact with the solid elements, instead of remaining in the standard mid-plane, Figure 4.3, model 2. This results in coincident nodes and degree of freedom for the plate and the adjacent face of the solid element.

It has to be noted that model 1 allows to easily simulate debonding effects and is useful to model curve plates, where it is more difficult to introduce the offset needed in model 2, but for flat plates leads to results identical to those achieved with model 2. During matrix assembly process, in fact, the slave degrees of freedom of the rigid links (RBE elements in MSC.Nastran) are eliminated and replaced by the corresponding master ones, thus leading to the same number of degrees of freedom of the model 2.

In the third model of Figure 4.3, both skin and viscoelastic core are modelled with solid elements. When using this approach, care has to be taken in order to avoid shear locking problems.

Liguore and Kosmatka, in fact, demonstrated that for the elastic skins the shear locking can occur for aspect ratios higher than 100:1, whereas for the viscoelastic core an aspect ratio of 5000:1 is still acceptable. In fact, the viscoelastic core is much less stiff than skins and this attenuates the locking effects in the global stiffness matrix.

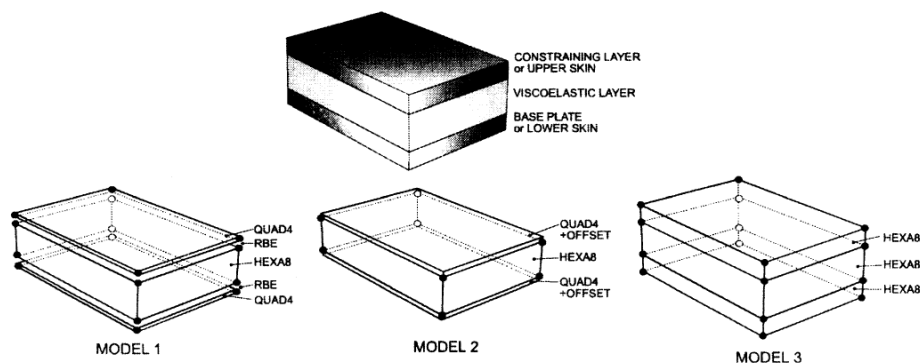


Figure 4.3 –Finite element models of viscoelastic damping

For the FE models of composite panels with damping layers embedded developed in the present work, model 2 representation has been preferred.

4.3 Structural-acoustic coupling

The problem in which a flexible structure interacts with an acoustic fluid, both from the point of view of the vibrating structure inducing pressure waves in a connecting acoustic fluid and the opposite case of acoustic pressure waves inducing structural vibrations has been deeply analysed (see, for example, the books from Cremer and Heckl or Fahy).

The two connecting domains, the flexible structure and the enclosed acoustic cavity, can be strongly coupled and, in that case, the structure-acoustic system must be studied as a coupled system to evaluate the natural frequencies and the response to dynamic excitation.

For complex shape structures, analytical solutions as ones proposed from Dowel (1963), Pretlove (1966), Guy (1979) and other authors are no longer available and numerical methods must be used.

Wolf and Nefske in 1975 first applied the FE code NASTRAN to model two dimensional acoustic cavities bounded by rigid and elastic walls.

The capability of this code have been later (1996) evaluated for fully coupled structure-acoustic problems and compared with analytical results by Fernholz and Robinson.

A review of the formulation of coupled structure-acoustic problems using the finite element method is described, for example in the work of Everstine, (1997), where approaches based on Finite Element (FE), Boundary Element (BE) and Infinite Element (IFE) are presented.

4.3.1 Structural domain equations

In the structural domain, the primary variable is displacement.

The discretized equation of motion for the structure can be written as:

$$[M_s]\{\ddot{x}\} + [D_s]\{\dot{x}\} + [K_s]\{x\} = \{F_s(t)\} \quad (4.6)$$

where $\{x\}$ is the structural displacement vector and $[M_s]$, $[D_s]$ and $[K_s]$ are respectively the mass, damping and stiffness matrix for the structure.

The loading term can be expressed as:

$$\{F_s\} = \{L_s^e\} + \{L_f\} \quad (4.7)$$

where:

$\{L_s^e\}$ is the vector of the external forces acting on the structure

$\{L_f\}$ is the vector of the fluid's load on the structure.

4.3.2 Fluid domain equations

For the fluid domain, several different primary variables can be used to describe the motion. Using the fluid displacement as the primary variable, i.e. the acoustic pressure, fluid both the structural and fluid domains can be described with the same type of solid elements.

The basic equations governing the coupling between an acoustic volume and the structure are herein simply recalled.

Fluid dynamics is described by equation of continuity, equation of motion and constitutive equation that, under the hypothesis of:

- small displacements
- absence of viscosity
- absence of convective phenomena
- locally linear dependence between pressure and density

can be expressed as:

$$\frac{\partial \rho}{\partial t} + \rho \nabla \cdot v = q \quad (4.8)$$

$$\rho \frac{\partial v}{\partial t} + \nabla p = b - q(v - v_q) \quad (4.9)$$

$$p = c^2 \rho \quad (4.10)$$

where ρ is the density, v is the fluid velocity field, q is the added fluid mass per unit volume and time, p is the pressure, b are the external forces per unit mass, c is the speed of sound and v_q is the velocity of the added fluid mass.

By combining the previous equations, the inhomogeneous linearized wave equation can be obtained:

$$\frac{\partial^2 p}{\partial t^2} = c^2 \nabla^2 p - c^2 \rho \nabla \cdot b + c^2 \frac{\partial q}{\partial t} \quad (4.11)$$

The body forces b can be associated to a potential:

$$b = \nabla \varphi \quad (4.12)$$

thus, substituting the (4.12) in the (4.11):

$$\frac{\partial^2 p}{\partial t^2} = c^2 \nabla^2 (p - \rho \varphi) + c^2 \frac{\partial q}{\partial t} \quad (4.13)$$

where the term $\rho \varphi$ can be interpreted as a prescribed pressure quantity applied inside the fluid domain.

4.3.3 Coupled domain equations

For a complete understanding of sound propagation processes it is obviously not sufficient to investigate the field equations for sound propagation. Additionally, boundary conditions have to be considered.

At the fluid-structure interface, and, in general, for an elastic boundary surface, the boundary conditions to be satisfied are from both the fluid and the structure side. The fluid acts as a pressure force on the structure and the structure transfer its mass acceleration to the fluid. This results in the following equation for respecting the boundary conditions:

$$\frac{\partial p}{\partial n} = -\rho \ddot{x}_n \quad (4.14)$$

where n is the direction of the outward normal and x_n is the structural displacement in the direction of n .

Considering the equilibrium of forces at the interface nodes and converting the previous equation in a “finite element form“, one can write the equation of motion for the fluid in a form similar to the (4.6):

$$[M_f] \{\ddot{p}\} + [D_f] \{\dot{p}\} + [K_f] \{p\} = \{F_f(t)\} \quad (4.15)$$

where $\{p\}$ is the vector of the unknown nodal values of the pressure, and $[M_f]$, $[D_f]$ and $[K_f]$ are respectively the mass, damping and stiffness matrix for the fluid.

The loading term can be expressed as:

$$\{F_f\} = \{L_{ff}\} - \{L_s\} \quad (4.16)$$

where:

$\{L_{ff}\}$ is the vector of the external forces acting on the fluid.

$\{L_s\}$ is the vector of the structure’s load on the fluid.

The terms L_f in equation (4.6) and L_s in equation (4.16) account for the structural-acoustic coupling. L_f , in fact, depends from the fluid pressure and L_s depends from the structural displacements.

They can be expressed as:

$$\{L_f\} = [K_c]\{p\} \quad (4.17)$$

$$\{L_s\} = [M_c]\{\ddot{x}\} \quad (4.18)$$

When substituting the (4.17) in the (4.6) and the (4.18) in the (4.15), it results:

$$[M_s]\{\ddot{x}\} + [D_s]\{\dot{x}\} + [K_s]\{x\} = \{L_s^e\} - [K_c]\{p\} \quad (4.19)$$

$$[M_f]\{\ddot{p}\} + [D_f]\{\dot{p}\} + [K_f]\{p\} = \{L_{ff}\} - [M_c]\{\ddot{x}\} \quad (4.20)$$

These two equations can be assembled and written as:

$$\begin{bmatrix} M_s & 0 \\ M_c & M_f \end{bmatrix} \begin{Bmatrix} \ddot{x} \\ \ddot{p} \end{Bmatrix} + \begin{bmatrix} D_s & 0 \\ 0 & D_f \end{bmatrix} \begin{Bmatrix} \dot{x} \\ \dot{p} \end{Bmatrix} + \begin{bmatrix} K_s & -K_c \\ 0 & K_f \end{bmatrix} \begin{Bmatrix} x \\ p \end{Bmatrix} = \begin{Bmatrix} L_s^e \\ L_{ff} \end{Bmatrix} \quad (4.21)$$

It can be showed that $M_c = c^2 \rho K_c^T$. If the second row of the equation (4.21) is multiplied by the factor $1/B$, where $B = \rho c^2$ is the bulk modulus of the fluid, another form of the equation (4.21) can be obtained where, for the sake of brevity, the same notation for the matrices and the load vectors involved is used:

$$\begin{bmatrix} M_s & 0 \\ -A^T & M_f \end{bmatrix} \begin{Bmatrix} \ddot{x} \\ \ddot{p} \end{Bmatrix} + \begin{bmatrix} D_s & 0 \\ 0 & D_f \end{bmatrix} \begin{Bmatrix} \dot{x} \\ \dot{p} \end{Bmatrix} + \begin{bmatrix} K_s & A \\ 0 & K_f \end{bmatrix} \begin{Bmatrix} x \\ p \end{Bmatrix} = \begin{Bmatrix} L_s^e \\ L_{ff} \end{Bmatrix} \quad (4.22)$$

where A (Coupling Matrix) is the matrix $-K_c$ from equation (4.21).

This equation is non-symmetric and being costly to solve, makes difficult to obtain eigenvalues for large systems. It can be shown that the eigenvalues of the coupled system are real.

Many methods have been developed with the aim to obtain a symmetric formulation of the equation (4.22), here is discussed the method proposed by Everstine (1981), that is also the one implemented in the code MSC.Nastran.

A symmetric version of the equation (4.22) can be derived with the following procedure:

1. Define the fluid velocity potential q as $p = \dot{q}$.
2. Substitute \dot{q} for p in the structure equation and replace the vector terms with their derivative equivalents in the fluid equation.
3. Multiply the fluid equation by -1 and integrate with respect to time.
4. Recombine the achieved relations.

$$\begin{bmatrix} M_s & 0 \\ 0 & M_f \end{bmatrix} \begin{Bmatrix} \ddot{x} \\ \ddot{q} \end{Bmatrix} + \begin{bmatrix} D_s & A^T \\ A & -D_f \end{bmatrix} \begin{Bmatrix} \dot{x} \\ \dot{q} \end{Bmatrix} + \begin{bmatrix} K_s & 0 \\ 0 & -K_f \end{bmatrix} \begin{Bmatrix} x \\ q \end{Bmatrix} = \begin{Bmatrix} L_s^e \\ -G \end{Bmatrix} \quad (4.23)$$

where G is defined as:

$$G = -\int_0^t L_{ff}(\tau) d\tau \quad (4.24)$$

4.4 Transmission Loss calculations

The proposed methodology for transmission loss calculation in discrete coordinates, that led to the expression (2.102), has been applied in the present work to predict aluminium alloy and composite panels acoustic behaviour.

A MATLAB code has been written that implements the necessary equations and reads the results of performed FE structural modal analysis in terms of eigenvalues and eigenvectors from MSC.Nastran punch (.pch) files.

Furthermore, the structure-acoustic coupling matrix and the subsequent mechanical force vector are obtained from a FE static analysis of the panel subjected to an uniform pressure load with the Nastran command OLOAD(PUNCH)=ALL.

The TL in the frequency range 0-3000 Hz, with a frequency resolution of 3 Hz, so that a vector of 1001 TL values is obtained, has been calculated using structure's modes up to 4500 Hz.

Results achieved for a 600x200 mm aluminium panel 1.5 mm thick have been compared with ones obtained for a composite panel with approximately the same weight as the metallic one and for a composite panel with a generic damping treatment 0.2 mm thick embedded (see Figure 4.4).

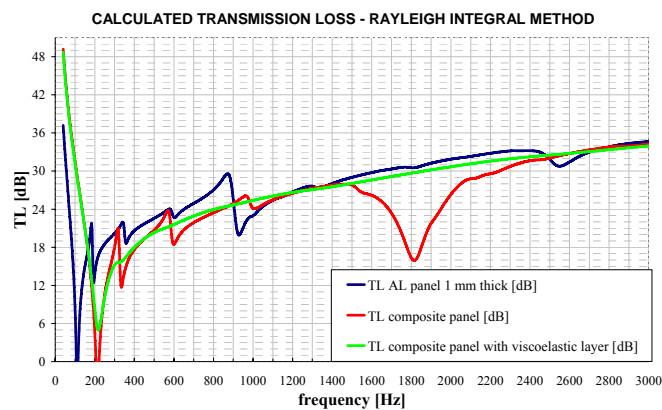


Figure 4.4 – Transmission Loss numerical results

It can be noted that the higher stiffness to weight ratio of the composite panel causes an higher TL at very low frequencies (stiffness driven frequency range) and an higher frequency of occurrence of the first panel's mode.

The composite panel calculated transmission loss presents a drop around 1800 Hz, it could be due to the presence of two acoustically efficient panel modes that occur close to that frequency, as it can be seen from the following Figure 4.5.

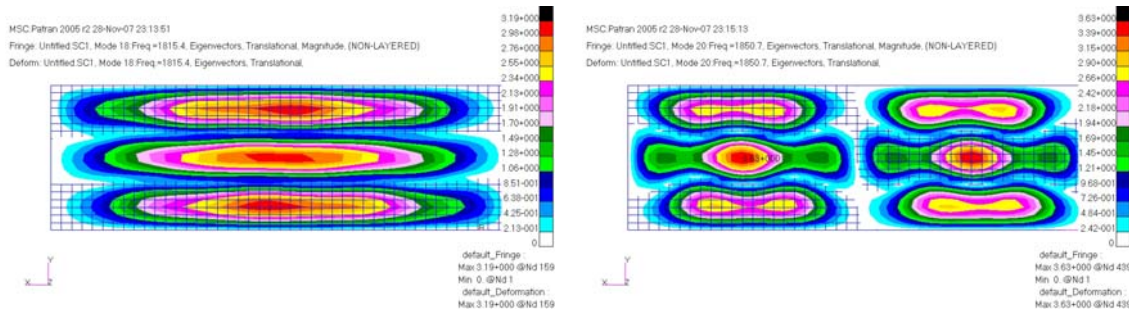


Figure 4.5 – Composite panel modes (1,3)@1815.4 Hz and (2,3)@1850.7 Hz

At higher frequencies, the main differences are related to the damping introduced in the model, being the mass of the aluminium and composite panels comparable. The critical frequency for both panels, respectively 6000 Hz for the aluminium one and 4100 Hz for the composite one, in fact, is well beyond frequency range of analysis.

Experimental Transmission Loss behaviours are often expressed in one-third octave bands. Thus, numerical results obtained have been transformed from narrow band ($df=3$ Hz) to one-third octave using ANSI standard bands limits (Figure 4.6).

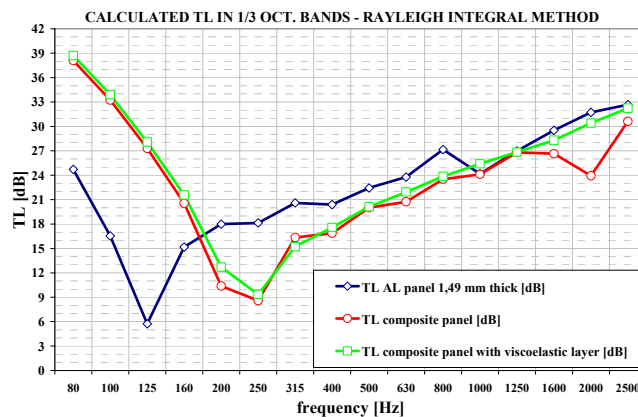


Figure 4.6 – Transmission Loss numerical results in 1/3 octave bands

5 Uncertainty and Variability

Real physical systems display both systematic and random variations. These random variations might arise from a variety of sources including the geometry of the problem, material properties, boundary conditions, initial conditions, or excitations imposed on the system. As a result, depending on the source of these variations, the behaviour of a system, or of a collection of nominally identical systems, will vary from one realization to another. While these realizations are individually deterministic, their effects in the collective are not; consequently, nondeterministic methods are needed to assess trends in the behaviour of this collection of responses.

Another aspect to stress is that in last years “virtual testing” have played key roles in the engineering development of advanced aerospace and flight systems. This is because some qualification tests simply cannot be performed (or it is absurd to do so); e.g. to launch a satellite to see whether it will survive launch. Other tests can be performed but are not because a completely test-based approach would be prohibitively expensive. Therefore, to some extent, nearly all advanced engineering systems rely on computational simulations to not only improve designs but also to qualify, i. e. ensure the satisfactory performance of, the system hardware and design. For this reason, validation of the computational simulations is key to ensuring the performance, safety and reliability of these systems.

Traditional simulation techniques, such as the finite element method, are deterministic, i.e. it is implicitly assumed that all parameters are precisely known and that the manufacturing process produces identical structure. Thus, it is fundamental to overcome this limitation and to be able to include uncertainties and their effects in simulations.

5.1 Source of Uncertainties in composite structures

In last years more and more interest has been given to composite materials to be used in aircraft primary structure because of their good mechanical properties and low weight. Although composite structures have significant advantages, they have some less favourable properties.

For composite materials, damping is taken to be any process within the body of the material in which energy is dissipated. The principal processes are associated with hysteretic losses within each of the constituent materials and interfacial effects at the

fibre-matrix interfaces. An aspect to highlight is related to the use of bonded joints instead of the riveted or bolted ones used for metallic structures. The friction in the joints, in fact, is one of the main causes of structural damping in aerospace structures, so their absence makes that damping is generally lower for composite structures. One of the possible solutions to increase composite damping consists in cocuring viscoelastic materials in the composite material structure to increase the damping and acoustic performance. This approach allows a high design flexibility since the viscoelastic layer can be placed in the most effective configuration. A possible drawback is that the viscoelastic layer must be incorporated into the laminate when it is cured, whereas with other damping application methods (such as free or constraining layer) the damping layer can be added after the part is made.

Besides the analysis of the vibration properties of composite constructions as structural elements, a study of their acoustical properties must also be taken into account in the initial design stages of aircrafts, automobiles and ships. For example, composite high stiffness-to-weight ratio causes that skin panels critical frequency is lower than the one for metallic panels and occurs where human hear is more sensitive to noise. In addition, because composite panels are generally orthotropic, the critical frequencies, unlike those of metals, are actually situated in a frequency band instead of at one particular frequency. These features usually result in poor sound transmission loss over a wider frequency range.

This is necessary that the weight saving advantages produced by composites are not compromised by high noise transmission, which would require heavy add-on acoustical treatments in later design stages. In many applications, it is important to know the sound transmission characteristics of the composite panels used in order to minimize the sound transmission from the exterior sources (engines, airframe) into the cabin.

Another aspect to take into account when dealing with composite structures design is the scattering of their mechanical and geometrical properties due to manufacturing and assembling process.

For example, variability of some composite properties such as elastic modulus and density can be addressed to (see Figure 5.1):

- fibres not uniformly distributed
- presence of voids in the matrix;

- random fibres interruptions;
- fibres interruption plus matrix absence;
- fibres cut;
- fibres interruption plus matrix absence plus delamination.

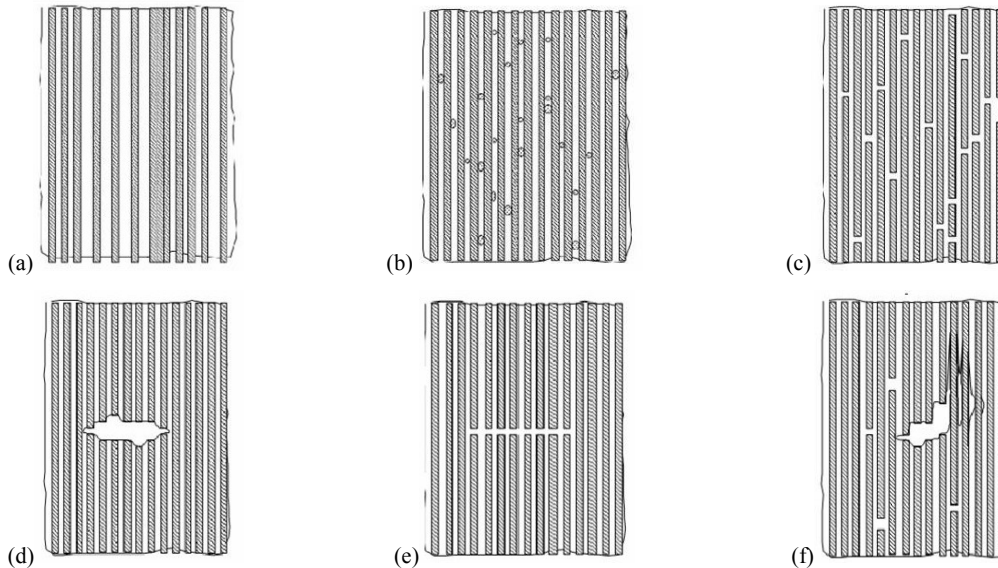


Figure 5.1 - Causes of uncertainties in the composite material.

Fibers not uniformly distributed (a); presence of voids in the matrix (b); random fibers interruptions (c); fibers interruption plus matrix absence (d); fibers cut (e); fibers interruption plus matrix absence plus delamination (f).

Structural analysis techniques based on deterministic methods (such as finite element method) are well suited for metallic structures, that show minimal dispersion around their nominal values, but are not able to take into account the uncertainties and the variabilities that characterize composite properties.

5.2 Taxonomy of non-deterministic terms

Examining the literature in many fields that deal with nondeterministic systems (e.g., operations research, structural dynamics, and solid mechanics) one finds that most authors do not carefully distinguish between what they mean by variability, uncertainty, and error, or worse, their definitions contradict one another.

Then, the first topic to assess is about taxonomy of non-deterministic terms.

In the present work, the classification introduced by Oberkampf (1999) and later integrated by Moens and Vandepitte (2005) is used.

An uncertainty, also known as reducible or epistemic uncertainty, can be defined as a potential deficiency, in any phase or activity of the modelling process, that is due to lack

of knowledge. The word potential stresses that the deficiency may or may not occur. This definition basically states that uncertainty is caused by incomplete information resulting from either vagueness, nonspecificity or dissonance.

Vagueness characterises information which is imprecisely defined, unclear or indistinct. It is typically the result of human opinion on unknown quantities ("the density of this material is around x"). Nonspecificity refers to the availability of a number of different models that describe the same phenomenon. The larger the number of alternatives, the larger the nonspecificity. Dissonance refers to the existence of conflicting evidence of the described phenomenon, for instance when there is evidence that a quantity belongs to disjoint sets.

For instance, the form of the constitutive model of a joint connecting two members of a complex structural system is not known; this uncertainty results from a lack of information about the joint's behaviour. Another example of epistemic uncertainty is the related situation where the constitutive model for the joint is known, but sufficient data to fully characterize the uncertainty in the model's parameters is not available. Reducible uncertainties can be further categorized as either modelling uncertainties (uncertainties in the errors of models of physical phenomena) or statistical uncertainties (uncertainties in probabilistic models).

The other branch of the taxonomy involves variability, elsewhere called irreducible or aleatory uncertainty. The term variability covers the variation which is inherent to the modelled physical system or the environment under consideration, consisting of fluctuations that are intrinsic to the problem being studied. Generally, the variability is described by a distributed quantity defined over a range of possible values. The exact value is known to be within this range, but it will vary from unit to unit or from time to time. Irreducible uncertainties cannot be reduced even if more information on the problem is collected. For instance, turbulent fluctuations of a flow field around an airplane wing, or, in a case related to the two just mentioned, sufficient data does exist to fully characterize a known joint model's parameters in a statistical manner. This is accomplished by specifying probability distributions for the parameters. This irreducible, parametric uncertainty is manifested in the uncertainty of the response of the complex structural system.

The success of engineering design depends significantly on whether the most appropriate model of uncertainty has been identified and used. A model used for design that overlooks uncertainty might cause severe consequences. On the other hand, a design based on a model that overestimates uncertainty will waste resources.

Analysis and prediction under uncertainty depend on representation of what is known about the uncertain phenomenon. Mathematical tools such as intervals, the probability theory, convex and fuzzy sets can be used to represent uncertainty, the choice of a model of uncertainty depends on the type and quantity of information available.

Probability models describe frequency of recurrence of events, or, equivalently, subjective degrees of belief of these likelihoods. Fuzzy models portray linguistic ambiguities as well as assessments of possibility or necessity of occurrence. Interval models are very conservative and are used to prevent the possibility of extreme events. Information-gap (info-gap) models of uncertainty quantify the disparity between what is known and what needs to be known in order to make an optimal decision.

The most common approach used to deal with non deterministic problems has been the probabilistic one. If enough information are available, the most direct approach consists in attempting to derive the statistics of the system response (and therefore the failure probability) from a knowledge of the statistical properties of the system and the applied loads.

5.3 Possibilistic approaches

However, traditional probabilistic modelling techniques cannot handle situations with incomplete or little information on which to evaluate a probability, or when that information is nonspecific, ambiguous, or conflicting (Walley, 1991; Ferson and Ginzburg, 1996).

Many generalized models of uncertainty have been developed to treat such situations, including fuzzy sets and possibility theory (Zadeh, 1978), probability bounds (Berleant, 1993), imprecise probabilities (Walley, 1991), info-gap models (Ben-Haim and Elishakoff, 1990, Ben-Haim 2006), and others.

5.3.1 Interval analysis

These generalized models of uncertainty have a variety of mathematical descriptions, but they are all closely connected with interval analysis (Moore, 1966), in which imprecision is described by an interval (or, more generally, a set).

When no objective or subjective information about properties distribution is available, in fact, uncertainty can be represented by intervals, whereby all parameters and response variables are bounded. Interval representation is particularly useful to prevent the possibility of extreme events. For example, when proving the response lies within an admissible range. Although interval arithmetic can be carried out for virtually any expression that can be evaluated using class arithmetic, a simple replacement of classical arithmetic by interval arithmetic will fail to produce adequately narrow bounds. Interval arithmetic, in fact, is sub-distributive and although addition or multiplication of intervals is commutative and associative, the distributive laws do not hold. This phenomena invariably reflects as an overestimation of the resulting interval width. And, if care is not taken, the interval width overestimation can grow to extremely large values (when compared to the mean), rendering the resulting intervals useless. Therefore, most numerical algorithms need to be modified for interval arithmetic.

5.3.2 Fuzzy analysis

A fuzzy number can be viewed as a nested collection of intervals corresponding to different levels of confidence α and the mathematical analysis associated with fuzzy set theory can be performed as interval analysis on different α -levels. Fuzzy sets model uncertainties through vague definition rather than by chance. A conventional (crisp) set either contains an element, or not. However, fuzzy sets define a series of intermediary belonging states between these two statements, introducing a degree of membership, represented by the membership function. This membership function describes the grade of membership to the fuzzy set for each element in the domain. The membership function can be considered as a possibility distribution function, providing information on the values that the described quantity can adopt. More generally, the possibility is defined as a subjective measure that expresses the degree to which the analyst considers that an event can occur. It provides in a system of defining intermediate possibilities between strictly impossible and strictly possible events. Through this interpretation, the fuzzy concept has become a tool to model subjective knowledge numerically in a non-probabilistic concept.

5.3.3 Information-gap analysis

An alternative technique is based on the theory of information-gap, that represents the disparity between what is known and what needs to be known in order to make a

reliable and responsible decision. Unlike other theories developed to represent uncertainty, information-gap does not assume probability density functions, which the theory of probability does, or membership functions, which fuzzy logic does. It is therefore appropriate in cases where limited data sets are available.

Uncertainty may be either pernicious or propitious. That is, uncertain variations may be either adverse or favourable. Adversity entails the possibility of failure, while favourability is the opportunity for sweeping success. Info-gap decision theory is based on quantifying these two aspects of uncertainty, and choosing an action which addresses one or the other or both of them simultaneously. The pernicious and propitious aspects of uncertainty are quantified by two "immunity functions": the robustness function and the opportuneness function.

The robustness function expresses the greatest level of uncertainty at which failure cannot occur. Robustness is a function of the decision variables, and one is inclined to prefer more robust designs over less robust designs. However, a basic theorem of info-gap theory establishes an irrevocable trade-off between robustness to uncertainty, and the quality of outcome: aspirations for quality entail loss of robustness. This trade-off is quantified by the robustness function.

The second design function is the opportuneness function which expresses the least uncertainty which entails the possibility of sweeping success. Uncertainty may be propitious, and the opportuneness function evaluates a design's propensity to exploit favourable uncertainty and to lead to outcomes far better than anticipated.

The main disadvantage of information-gap is that the efficiency of sampling techniques cannot be exploited because no probability structure is assumed. Instead, the robustness of a decision with respect to uncertainty is studied by solving a sequence of optimization problems, which becomes computationally expensive as the number of decision and uncertainty variables increases.

5.4 Probabilistic approach

In the classical frequentist application of the probabilistic concept, the goal of a numerical property description is to define a domain of possible values this property can adopt, and to give information on the frequency of occurrence of the numerical values in this domain. This is typically done by defining a probability density function over the domain of possible values.

Extensive literature exists on the subject of probability theory, treating a vast variety of PDFs and their applicability for description of random quantities. An overview of these can be found in the books of Miller and Freund (1985) or in Haldar and Mahadevan (2000).

It is clear that the probabilistic concept is most appropriate to represent variabilities, since in the frequentist interpretation, the probabilistic description using a PDF is completely consistent with the definition of a variability given in the previous paragraphs.

The information on the range and the likelihood of a certain variability can be unambiguously incorporated in the PDF. Furthermore, the probabilistic outcome of the analysis will give an indication of the actual expected frequency of occurrence of the analysed phenomenon. It is, however, important that all information is available in order for the model to realistically represent the variability. For instance, if more than one variable property is present in the model, the correlation between the different variabilities might play an important role in the probabilistic analysis.

In a probabilistic structural analysis the design parameters are treated as variables and the basic result from the analysis is a statistical distribution of the requested response and statistical sensitivities measuring the relative importance of the random variables involved.

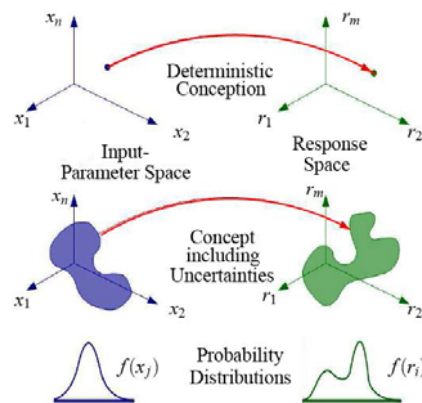


Figure 5.2 – Deterministic VS Probabilistic design approach (from Schuëller, 2007)
 The general approach to be used when dealing with this kind of problems can be summarized in the following steps (Long and Narciso, 1999):

1. Develop the functional relationships that define the model
2. Define the random variable inputs

3. Define the numerical models needed in the functional relationship
4. Choose the method that fits better the problem under study
5. Perform the probabilistic analysis
6. Analyze the results.

Typical probabilistic analyses can involve analytical as well as numerical models,

When performing probabilistic analysis using a finite element model, a realization of a random variable must be reflected in the numerical model's input. The variable may be a random variable or a computed variable from another code or analytical equation. In general, the variable can map to a single value in the code's input or to a vector of values such as nodal coordinates in the finite element model (Rihaet alii, 2001).

If $X=(X_1, \dots, X_n)$ represents a vector of n random variables, a limit state function $g(X)$ can be defined by the equation $g(X) = Z(X) - z_0 = 0$, where $Z(X)$ is a model response (so called performance function) and z_0 is a particular response value. The limit state function represents a hypersurface in n -dimensional random variable space that separates the space into failure and non-failure regions.

If the g -function is known, the probability of failure, p_f , can be expressed as the integral of the joint probability density function (JPDF) of the X variables, $f_X(X)$, over the failure region, identified by the condition $g(X) < 0$.

$$p_f = \Pr[g(X) < 0] = \int_{g(X) < 0} \dots \int f_X(X) dX \quad (5.1)$$

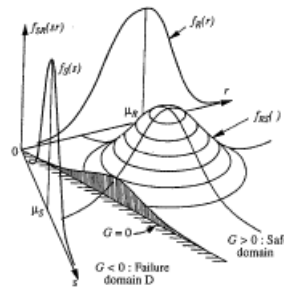


Figure 5.3 – Two random variables JPDF f_{rs} , marginal density functions f_r and f_s and failure domain D

In order to estimate the cumulative distribution function (CDF) one should compute the probability of failure $p_f = \Pr[g(X) < 0] = \Pr[Z(X) < z_0]$ for all values $z_0 \in [0, 1]$.

Except in very restricted cases, the integral in equation (5.1) is analytically intractable and needs to be evaluated numerically. One approach could be to compute the integral using a standard Monte Carlo (MC) procedure but, in many practical cases, mainly when the probability is small or the calculation of Z is expensive (e.g. output of a FE analysis with thousands of degrees of freedom), the MC method would lead to a very large computational time. For this reason importance sampling methods and Fast Probability Integration (FPI) techniques have been developed. These are based on a change of variables: a nonlinear transformation is made which converts the vector (X_1, \dots, X_n) into a vector (U_1, \dots, U_n) where the components have independent Gaussian distributions. The change of variables is usually performed applying a Rosenblatt or a Nataf transformation.

The limit surface $g(X)=0$ is converted into a surface $g(U)=0$, and the integral of interest becomes:

$$p_f = \Pr[g(U) < 0] = \int_{g(U) < 0} \dots \int f_U(U_1, \dots, U_n) dU_1 \dots dU_n \quad (5.2)$$

Now, although the integrand has factored into a sequence of univariate Gaussians, the domain of integration ($g(U) < 0$) is usually very complicated and the integral is still analytically impossible.

Thus, approximate methods have been developed that replace the limit surface $g(U)=0$ by a hyperplane (first order methods) or by a quadratic hypersurface (second order methods).

5.4.1 Monte Carlo and other Sampling Methods

The Monte Carlo method (Ulam et alii, 1947; Metropolis and Ulam, 1949) provides approximate solutions to a variety of mathematical problems by performing statistical sampling experiments on a computer.

Remarkably, the method applies to problems with absolutely no probabilistic content as well as to those with inherent probabilistic structure. This alone does not give the Monte Carlo method an advantage over other methods of approximation. However, among all numerical methods that rely on N -point evaluations in M -dimensional space to produce an approximate solution, the Monte Carlo method has absolute error of estimate that decreases as $N^{-1/2}$ whereas, in the absence of exploitable special structure, all others have errors that decrease as $N^{-1/M}$ at best. This property gives the Monte Carlo

method a considerable edge in computational efficiency as M , the size of the problem, increases.

Monte Carlo simulation techniques involve random sampling of the input variables to simulate artificially a large number of experiments and to observe the result (see, for example the books of Melchers or Madsen). In the case of analysis for structural reliability, this means, in the simplest approach, sampling each random variable X_i randomly to give a sample value X . The limit state function $g(X)$ is then checked. If the limit state is violated (i.e. $g(X) < 0$), the structure or structural element has “failed”. The experiment is repeated many times, each time with a randomly chosen vector X of X_i values. If N trials are conducted, the probability of failure p_f may be expressed as:

$$p_f = J = \int \dots \int I[g(X) < 0] f_X(X) dX \quad (5.3)$$

Where $I[\cdot]$ is an indicator function which equals 1 if $[\cdot]$ is “true” and 0 if $[\cdot]$ is “false”. Thus the indicator function identifies the integration domain. The previous equation (5.3) can be seen as representative of the expected value of $I[\cdot]$. If X_j is the j -th vector of random observation from $f_X(\cdot)$, it follows directly from sample statistics that:

$$p_f \approx J_1 = \frac{1}{N} \sum_{j=1}^N I[g(X) < 0] \quad (5.4)$$

is an unbiased estimator of J . Thus, the ratio:

$$p_f = \frac{N_f}{N} \quad (5.5)$$

where N_f is the number of samples that satisfy the relationship $g(X) < 0$, provides a direct estimate of the probability of failure.

The achieved results can also be represented fitting them on a cumulative distribution function (CDF), see Figure 5.4.

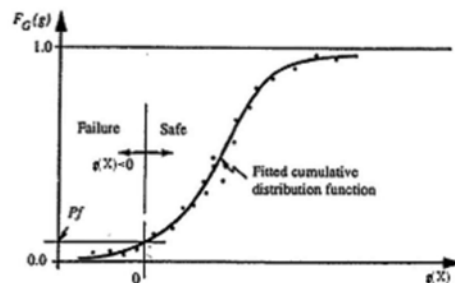


Figure 5.4 – Use of fitted CDF to estimate p_f

In exploiting this procedure, three matters are of interest: how to extract most information from the simulation points, how many simulation points are needed for a given accuracy, or conversely, how to improve the sampling technique to obtain greater accuracy for the same or fewer sample points. These matters will be considered below.

An estimate of the number of simulations required for a given confidence level may be made as follows. Since $g(X)$ is a random variable in X , the indicator function $I[g(X) < 0]$ is also a random variable, albeit with only two possible outcomes. It follows from the central limit theorem that the distribution of J , given by the sum of independent sample functions, approaches a normal distribution as $N \rightarrow \infty$. The mean of this distribution is:

$$E(J_1) = \sum_{i=1}^N \frac{1}{N} E[I(g(X) < 0)] = E[I(g < 0)] = J \quad (5.6)$$

whereas the variance is given by:

$$\sigma_{J_1}^2 = \sum_{i=1}^N \frac{1}{N^2} \text{var}[I(g(X) < 0)] = \frac{\sigma_{I(g < 0)}^2}{N} \quad (5.7)$$

From the relation (5.7) descends that the variance of the Monte Carlo estimates varies directly with the variance of $I[g(X) < 0]$ and inversely with $N^{1/2}$.

To calculate confidence levels, an estimate of the variance σ_J^2 is required. This can be done considering that:

$$\text{var}[I(\cdot)] = \int \dots \int [I(g(X) < 0)]^2 dX - J^2 \quad (5.8)$$

So that the sample variance can be expressed as

$$S_{I(g < 0)}^2 = \frac{1}{N-1} \left(\left\{ \sum_{j=1}^N I^2[g(X_j) < 0] \right\} - N \left\{ \frac{1}{N} \sum_{j=1}^N I[g(X_j) < 0] \right\}^2 \right) \quad (5.9)$$

Where the last $\{\cdot\}$ term is simply the mean (5.6) or, by equation (5.4), the estimate J_I for p_f .

The application of the Central limit theorem that states that many independent and identically-distributed random variables will tend to be distributed as a Gaussian, allows to write the following relation for J_I .

$$P(-k\sigma < J_1 - \mu < k\sigma) = C \quad (5.10)$$

Where μ is the expected value of J_I given by the (5.6) and σ is the standard deviation expressed in the (5.7). An a priori estimation for σ could not be obtained from the

sample estimate given in (5.9) because this relation uses the results of the MC simulations. According with Shooman (1968), mean and standard deviation can be estimated by the binomial parameters $\sigma = [Np(1-p)]^{1/2}$ and $\mu = Np$, where p is the probability of the binomial distribution, according that $Np \geq 5$ when $p \leq 0.5$.

By substituting the binomial parameters in the equation (5.10) it is achieved:

$$P\left(-k[Np(1-p)]^{1/2} < J_1 - Np < k[Np(1-p)]^{1/2}\right) = C \quad (5.11)$$

The Monte Carlo methods allows for an estimation of the error committed. In fact, if the error between the actual value of J_1 and the observed value is defined as $\varepsilon = (J_1 - Np)/Np$ and this is substituted in the (5.11), it results:

$$\varepsilon = k[(1-p)/Np]^{1/2} \quad (5.12)$$

For a confidence interval $C=95\%$ ($1-\alpha=0.95$), from the standard normal tables it results $k = \Phi^{-1}(1-\alpha/2) = 1.96$, where Φ is the CDF of the normal standard distribution.

If in the previous equation p is substituted with the probability of failure p_f , it results:

$$\%error = 100 \cdot \Phi^{-1}\left(1 - \frac{\alpha}{2}\right) \sqrt{\frac{1-p_f}{N \cdot p_f}} \quad (5.13)$$

Inverse form of this expression allows for estimate the number of MC simulations required in order to achieve results within prescribed error bounds:

$$N = \frac{1 - P_f}{P_f} \cdot \left(\frac{\%error}{100 \cdot \Phi^{-1}\left(1 - \frac{\alpha}{2}\right)} \right)^{-2} \quad (5.14)$$

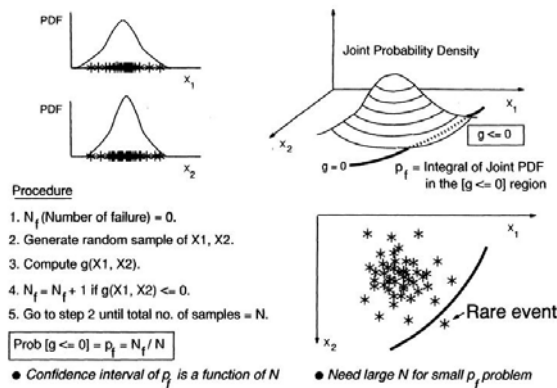


Figure 5.5 – Reliability Analysis by Monte Carlo Simulation (NESSUS Manual, 2001)

Every integral evaluation problem amenable to the Monte Carlo method comes with an explicit or implicit sampling plan usually dictated by the context in which the problem arises. If the cost of using this plan to achieve the desired statistical accuracy for the estimate of Z falls within the available computing budget, then no need exists to consider alternative plans. This circumstance often holds when the cost of computer time is low. When the cost of the original sampling plan exceeds the available budget, then selecting an alternative sampling plan that meets the budget constraint is an essential first step in the application of the Monte Carlo method. Because it results that the sampling plan that induces the smallest variance per replication leads to the smallest sample size N required to achieve a specified absolute error criterion, it makes sense to search for sampling plans that reduce variance in order to increase efficiency of Monte Carlo experiments.

Methods aimed to improve efficiency of the Monte Carlo have been developed based on a modified sampling space that can be defined only on the basis of an a priori information about the problem to be solved. In other words, if the sampling is made only in a specified sub-region of the definition domain of the JPDF of the random variables, the same accuracy level of the “raw” Monte Carlo can be obtained with a reduced number of samples.

From the mathematical point of view, the equation (5.3) can be written as:

$$p_f = J = \int \dots \int I[g(X) < 0] \frac{f_X(X)}{h_v(X)} h_v(X) dX \quad (5.15)$$

Where $h_v(\cdot)$ is the so called importance sampling density function.

The principal objective of an importance sampling approach is to minimize the choice of samples in the safe region. Thus, the most obvious choice for the reduced sampling domain is the region in which it results that $g(X) < 0$ with an high probability level. This region can be identified as the sub-domain in the failure region closest to the so called maximum likelihood point X^* that is the point belonging to the limit state surface $g(X) = 0$ having the largest probability. This point, also known as Most Probable Point (MPP), in alternative way can be defined in the standard normal space (u -space) as the point that defines the minimum distance β , from the origin ($u=0$)

to the limit-state surface $g(u)=0$. In most cases, the MPP can be found by the direct application of numerical maximization techniques.

Once X^* has been identified, the simplest choice for choosing h_v is to shift the distribution $f_X(X)$, so that its mean is in X^* .

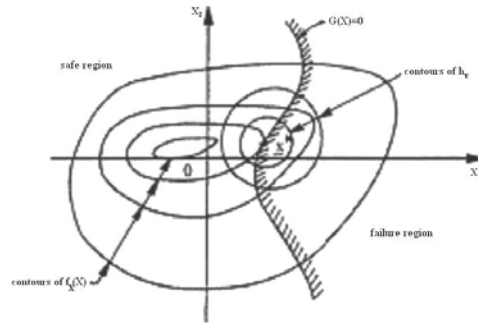


Figure 5.6 – Importance sampling function in X space

As it can be seen from the Figure 5.6, the shape of the limit state function has small weight on the effectiveness of the importance sampling approach that can be used also if $g(X)=0$ is sharp or non linear. On the other side, as well as for other methods based on MPP that will be discussed later, the choice of X^* is crucial. It can happen, in fact, that the MPP is not unique or that the MPP search algorithm is not able to correctly identify the absolute maximum of the distribution $f_X(X)$.

The Adaptive Importance Sampling (AIS) methods minimize sampling in the safe region by adaptively and automatically adjusting the sampling space from an initial approximation of the failure region. The sampling space is defined using a limit-state surface (boundary). The performance of AIS depends on the quality of the initial failure region approximation. Even though the AIS method cannot totally replace the standard Monte Carlo method, it provides efficient accuracy improvement and can be used to check correctness of results obtained with the MPP-based approximation methods (FORM, SORM, AMV+). In fact, these latter methods, that will be discussed in the following paragraphs, do not allow for an error estimate.

5.4.2 Response Surface Approximation Method

For complex structures, the performance function is not available as an explicit function of the random design variables. The performance (or response) of the structure can only be evaluated numerically at the end of a (often time-consuming) structural analysis procedure such as the finite element method. The goal of the response surface

methodology (RSM) is to find a predictive equation relating a response to a number of input variables. Once accomplished this, the equation can be used to determine the response, once given the values of input variables, without the need to repeatedly run the time-consuming deterministic structural analysis (see, for example, Myers and Montgomery, 1995).

The response surface thus represents the result (or output) of the structural analysis encompassing (in theory) every reasonable combination of all input variables.

Starting from an achieved response surface, it is possible to create (via simulation) thousands of combinations of all design variables, and perform a pseudo structural analysis for each variable set, by simply looking up (via interpolation) the corresponding surface value. Each approximation of structural analysis output is thus generated in a matter of milliseconds. The end result is the creation of the probability distribution function (PDF) of the performance function. Once the response PDFs are defined, other methods (numerical integration, Monte Carlo, limit state approximation) can be used to determine the probability of failure. The general steps, shown graphically in Figure 5.7, to use the RSM are as follows:

1. Perform the deterministic analysis (e.g., FEM) at strategically predetermined values of the random variables.
2. Using the results of step 1, construct an approximate closed-form expression for the response variable (could be stress, strength, acceleration, etc.) in terms of the design variables, using regression techniques.
3. Create a response (e.g., applied stress) PDF from simulation of the design variables using the regression equation.
4. Find the probability of failure from the response PDFs using numerical integration, Monte Carlo simulation or approximation methods.

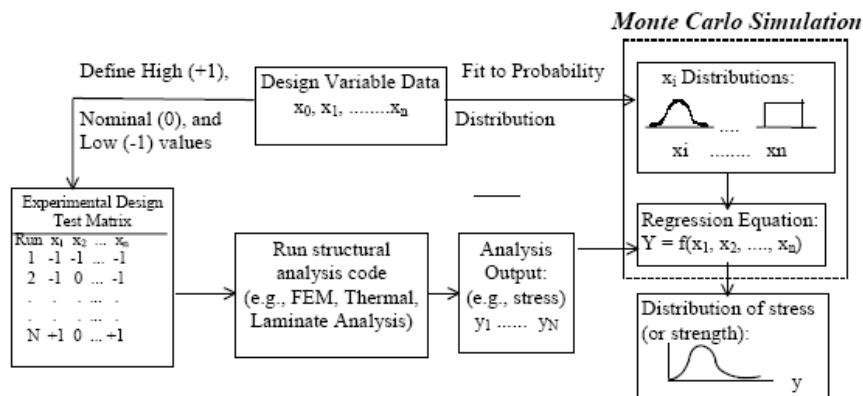


Figure 5.7 – RSM procedure using 3 levels of N design variables

5.4.2.1 Step 1: Analyze Structure at Chosen Values

The challenge is to define representative combinations of the design variables to produce a representative output (response). Statistical design-of-experiments techniques can be used to select these representative combinations and systematically simulate the structural analysis. These are analogous to Monte Carlo simulation, but by using experimental design methods, strategic combinations of design variable values are employed to attempt to create an envelope containing all possible (within engineering reason) output values. In general, in a Design of Experiment (DOE), the experiments are set up in such a way that a maximum amount of information is obtained in a minimum amount of computation time.

The selection of a DOE method depends on the available computational power and the expected order (linear, quadratic with/without cross terms, ...) of the RS model that is required to accurately represent the actual functional performances.

There are many experimental designs and sampling methods which address the issue of adequate and representative sample selection. However, all of these methods can be classified in two main categories: orthogonal designs and random designs.

The orthogonality of the designs means that the model parameters are statistically independent, in the sense that the factors in an experiment are uncorrelated and can be varied independently one of each other. A popular scheme is the full (or $2N$) factorial DOE scheme. For a problem with N input parameters, all $2N$ possible combinations of parameter extrema (a_i, b_i) are evaluated.

Widely used methods are fractional and full-factorial designs, Central Composite and Box-Behnken designs.

In random designs the value of parameters of the model chosen for the experiments are based on a random process. The most common random design is the Latin hypercube sampling.

In the following paragraphs some details on Central Composite and Box-Behnken design and Latin hypercube sampling are given.

5.4.2.1.1 Central Composite design

A Box-Wilson Central Composite Design, commonly called central composite (CC) design, contains an imbedded factorial or fractional factorial design with centre points that is augmented with a group of “star points” that allow estimation of curvature. If the distance from the centre of the design space to a factorial point is ± 1 unit for each factor, the distance from the centre of the design space to a star point is $\pm\alpha$ with $|\alpha| > 1$. The precise value of α depends on certain properties desired for the design and on the number of factors involved.

It is possible to individuate three types of points:

- axial points: $2n$ points created by a Screening Analysis, where one of the parameters has the minimum or maximum value and all other parameters have their nominal value.
- cube points: 2^n points come from a Full Factorial design, where sample points have all possible combinations of the minimum and maximum values of the control parameters.
- centre point: a single point in the centre is created by a Nominal design, where all control parameters are set to their nominal values.

There are three types of CC designs, (Central Composite Circumscribed (CCC), Central Composite Inscribed (CCI), and Central Composite Face-centered (CCF)), having all the structure shown in Figure 5.8 but with different values for a_i and b_i .

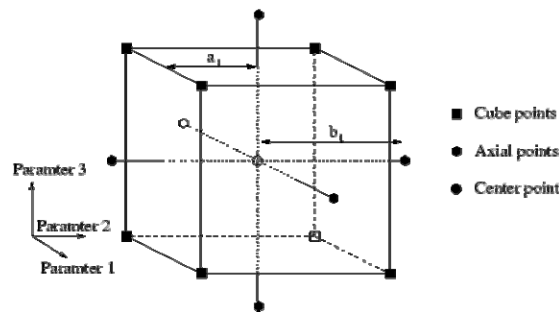


Figure 5.8 – The example points of a Central Composite Circumscribed design with three input parameters

These values of the three CC designs are listed in Table 5.1.

	b_i/a_i	$range_i$
CCC	\sqrt{n}	$2 a_i$
CCI	\sqrt{n}	$2 b_i$
CCF	1	$2 a_i = 2 b_i$

Table 5.1 - Factors a and b for Central Composite designs with full

Two of these designs - CCC and CCI - have a special characteristic; they are rotatable. A design is said to be rotatable, if upon rotating the design points about the centre point the moments of the distribution of the design remain unchanged.

5.4.2.1.2 Box-Behnken design

The Box-Behnken method is an independent quadratic design that can be graphically explained thinking about a cube whose volume represents all possible combinations of three continuous input variables. The centre of this cube would correspond to the input variables at their nominal values. The corner points represent the eight possible combinations of the three input variables at their extreme values: *(Low, Low, Low)*, *(Low, Low, High)*, ... *(High, High, High)*.

The Box-Behnken Matrix method does not evaluate the response variable for the eight corner points of this cube. Instead, it considers those 12 points where two of the input variables are at extreme values and the other is at nominal, corresponding to the midpoints of the 12 edges comprising the cube. It also considers the centre point of the cube, thus bringing the total number of deterministic evaluations to 13 (Figure 5.9).

In the following Table 5.2, the 13 tests that would be performed in the hypothesis of $n=3$ random variables are presented.

Test Run No.	Variable 1	Variable 2	Variable 3
1	low	low	nominal
2	low	high	nominal
3	high	low	nominal
4	high	high	nominal
5	low	nominal	low
6	low	nominal	high
7	high	nominal	low
8	high	nominal	high
9	nominal	low	low
10	nominal	low	high
11	nominal	high	low
12	nominal	high	high
13	nominal	nominal	nominal

Table 5.2 - Box-Behnken experimental design matrix

In general, for n random variables, the Box-Behnken method requires $2n(n-1)+1$ deterministic evaluations.

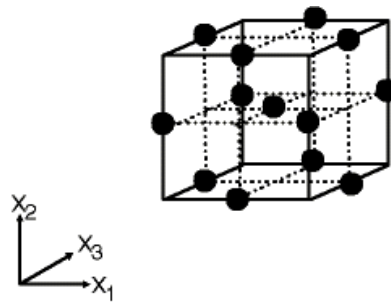


Figure 5.9 – Box-Behnken design cube

5.4.2.1.3 Latin hypercube sampling method

Another widely used method for experimental design, originally developed by McKay, Conover, and Beckman in late Seventies, is known as Latin hypercube sampling.

This method selects k different values from each of n variables X_1, \dots, X_n in the following manner. The range of each variable is divided into k non-overlapping intervals on the basis of equal probability. One value from each interval is selected at random with respect to the probability density in the interval. The k values thus obtained for X_1 are paired in a random manner (equally likely combinations) with the k values of X_2 . These k pairs are combined in a random manner with the k values of X_3 to form k triplets, and so on, until k n -tuplets are formed. These k n -tuplets are the same as the k n -dimensional input vectors that can be obtained as output of a Monte Carlo simulation based on k samples. This is the Latin hypercube sample. It is convenient to think of this sample (or any random sample of size n) as forming a $[k \times n]$ matrix of input where the i -th row contains specific values of each of the n input variables to be used on the i -th run of the finite element model.

To help clarify how intervals are determined in the Latin hypercube sample, a simple example can be considered where it is desired to generate a Latin hypercube sample of size $n = 5$ with two input variables, X_1 and X_2 . If it is assumed that the first random variable X_1 has a normal distribution with mean μ and variance σ^2 , the endpoints that limit the five intervals on X_1 can be estimated from the relations:

$$\begin{aligned} \Pr(-\infty < X_1 \leq A) &= \Pr(A \leq X_1 \leq B) = \Pr(B \leq X_1 \leq C) = \\ &= \Pr(C \leq X_1 \leq D) = \Pr(D \leq X_1 < +\infty) = 0.2 \end{aligned} \quad (5.16)$$

Thus each of the five intervals corresponds to a 20% probability (Figure 5.10).

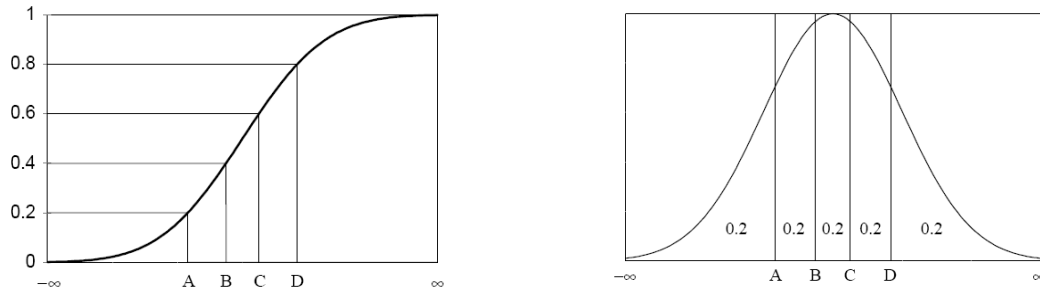


Figure 5.10 – CDF and PDF of a Latin hypercube sample for a Normal variable, $n=5$

In a similar manner, if the second random variable, X_2 , has a uniform distribution on the interval from G to L , the corresponding intervals used in the Latin hypercube sample for X_2 can be easily computed. These intervals are given in Figure 5.11 in terms of both cumulative and the density functions.

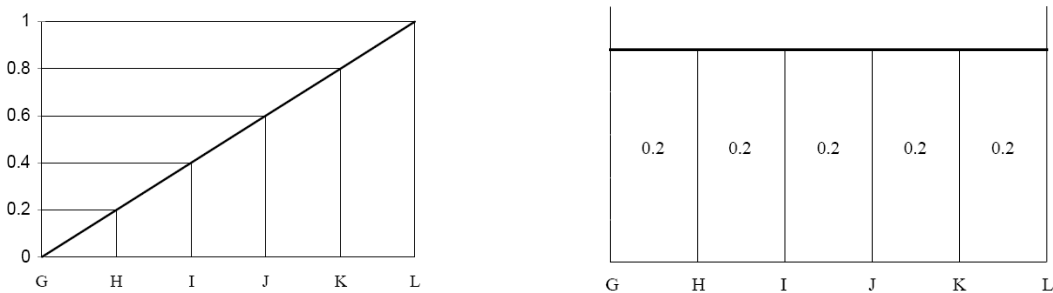


Figure 5.11 – CDF and PDF of a Latin hypercube sample for a Uniform variable, $n=5$

The next step in obtaining the Latin hypercube sample is to pick specific values of X_1 and X_2 in each of their five respective intervals. This selection must be done in a random manner with respect to the density in each interval; that is, the selection must reflect the height of the density across the interval.

For example, in the $(-\infty, A)$ interval for X_1 , values close to A will have a higher probability of selection than those values in the tail of the distribution that extends towards $-\infty$.

Next, the selected values of X_1 and X_2 are randomly paired to form the five required two-dimensional input vectors.

The fact of combining the permutations of the levels in a random way ensures that each level is present in the design and the number of levels is maximized.

Latin hypercube designs do not suffer the collapse problem, because if one or more of the factors appear not to be important, every point in the design still gives information about influence of the other factors on the response. In this way none of the time-consuming computer experiments become useless.

5.4.2.2 Step 2: Develop regression equations

Once all FEM runs having as input variables vectors determined on the base of one design of experiments procedure, a linear regression equation relating the design variable or performance function, Z , to the variables X_1, \dots, X_n can be obtained. In the case of the Box-Behnken design developed for fitting second-order response surfaces, the regression equation that can be estimated is of the form:

$$Z = \beta_0 + \sum_{i=1}^n \beta_i X_{k,i} + \sum_{i=1}^n \beta_{n+i} X_{k,i}^2 + \sum_{i=1}^{n-1} \left(\sum_{j=i+1}^n \beta_{(i,j)} X_{k,i} X_{k,j} \right) \quad (5.17)$$

where β are the unknown coefficients, n is number of random variables in input and the index k takes into account the deterministic analyses performed.

It is assumed that the regression equation will produce accurate estimates for the variable Z as long as the values for all the design variables are somewhere between their low and high values. That is, the regression model should not be extrapolated. One goal in regression analysis is to not have excessive terms in the equation, as the model is being forced to twist and turn through too many data points, thereby misrepresenting the nature of the response surface. To obtain the best small model, the first step is to eliminate those terms that, being based on physically meaningless combinations of variables, do not make physical sense.

5.4.2.3 Step 3: Develop Response Variable PDF

Once the regression equation using all the design variables is developed, Monte Carlo simulation is used to generate a distribution for the response variable. A random draw is made from each design variable probability distribution, as shown in Figure 5.7, and then a single response value associated with the set of chosen design variable values is calculated via interpolation. The result is a series of response values which can then be fit to a probability distribution or used to create a discrete distribution if a continuous distribution does not provide an adequate fit.

5.4.2.4 Step 4: Evaluate Probability of Failure

Once that performance function distribution has been achieved, probability of failure can be calculated either with a numerical integration procedure or by applying Monte Carlo or limit state approximation methods.

Several important notes regarding the response surface methodology:

- Probability distributions for the input variables must be accurate.

- Regression equations must fit analysis results well and since they are only quadratic in nature, should only be used in situations where there are no abrupt changes in the response for moderate changes of input variables.
- Monte Carlo simulation must be run enough times to get an accurate depiction of the response variable's probability distribution.

5.4.3 Limit State Approximation Methods

As already stated, Monte Carlo simulation for complex structural analysis codes is impractical from an execution time point of view, especially for low failure probabilities. Applying one of the discussed techniques such as the response surface method or importance sampling, to reduce the amount of structural analyses (e.g., FEM) required, is one way of approaching the problem.

Another approach to solving the multivariable integral is to employ limit state approximation methods. These methods, especially useful for analyzing computationally demanding numerical models, allow for quick estimations of the CDF, trying to approximate the original *g-functions* by simple linear or quadratic functions. The limit state approximation methods, also referred to as point expansion methods in the literature, can be divided into two groups:

- Mean Value methods
- Most Probable Point and Advanced Mean Value methods.

5.4.3.1 Mean Value methods

To the first group belong the simplest, least-expensive reliability methods in that they estimate the response means, standard deviations, and all CDF response-probability-reliability levels from a single evaluation of response functions and their gradients at the uncertain variable means.

This approximation can have acceptable accuracy when the response functions are nearly linear and their distributions are approximately Gaussian, but has been shown to be potentially inaccurate for high reliability (low probability of failure, 10^{-5} or below) calculations, as well as for highly nonlinear performance functions.

Mean Value First Order (MVFO) and Mean Value First-Order Second-Moment (MVFOSM) methods are based on a Taylor's series expansions of the *Z-function* at the mean value:

$$Z(X) = Z(\mu) + \sum_{i=1}^n \left(\frac{\partial Z}{\partial X_i} \right) (X_i - \mu_i) + H(X) = a_0 + \sum_{i=1}^n a_i X_i + H(X) = Z_{MV}(X) + H(X) \quad (5.18)$$

where the derivatives are evaluated at the mean values. Z_{MV} , that is the Mean Value First Order (MVFO abbreviated also as MV), is a random variable representing the sum of first order terms and $H(X)$ represents the higher order terms. There are several ways of obtaining a_i coefficients, for user-defined g-functions they can be computed by numerical differentiation method whereas for user-defined data sets the least-squares method can be applied. The minimum required number of *Z-function* evaluations is $(n+1)$.

When probability distributions of X_i are defined, the CDF of the first order terms, Z_{MV} , is completely defined. In general the MV solution is not enough accurate and it could be possible to improve accuracy just taking into account higher order terms in Taylor's series expansion. The method that is based on the truncation of the expansion at second order terms is known as Mean Value Second Order method. However, the higher-order approach, especially in case of to implicit *Z-functions* and large number of random variables, becomes difficult and inefficient and causes again an excessive increase of the computational time.

More efficient first-order methods have been developed that can improve accuracy without increasing complexity.

5.4.3.2 Most Probable Point Methods

There are several methods in this group, the main ones being First-Order Reliability Method (FORM), the Second-Order Reliability Method (SORM) and the Advanced Mean Value Methods (AMV and AMV+).

The common approach to these methods consists in to transform the integral above to an approximately equal integral that can be efficiently evaluated. This can be done by the following steps:

1. Transform the design variable distributions into standard normal distributions. That is, transform $g(X) = 0$ into $g(u) = 0$ where u is a vector of standardized, independent Gaussian variables. This is usually made by applying Rosenblatt transformation.
2. Identify the most probable point (MPP), or design point. For a given limit state function, the main contribution to failure probability comes from the

region where g is closest to the origin in the transformed design variable space (u -space).

3. Develop a polynomial approximation to the performance function around the MPP. Thus the g -function is approximated by a simply defined (quadratic) surface through that point (MPP). Compute probability of failure using the newly defined g -function and the transformed variables.

The various steps necessary for the implementation of MPP based methods can be summarized in graphical form as in the following Figure 5.12.

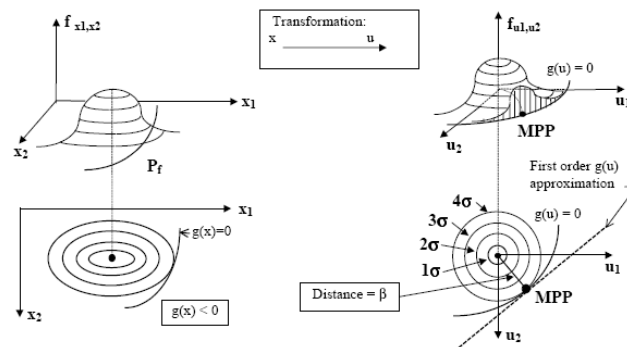


Figure 5.12 – MPP based methods application procedure

In general the MPP based methods are well developed for problems with single, well-behaved (monotonic and continuously differentiable) limit states functions.

5.4.3.2.1 Step 1: Evaluate Probability of Failure

MPP based reliability approximations are carried out in the space of a set of standard, uncorrelated normal variables U , obtained by transforming the basic variables X . This transformation is dependent on the form of the probability distribution of each variable. The advantage of doing this probability transformation is to be able to exploit the superior properties of standard normal space. In the u -space, in fact, the JPDF of the response is rotationally symmetric around the origin and decays exponentially with the square of the distance from the origin. Thus, the minimum distance point is the Most Probable Point, as it can be appreciated from the graph in Figure 5.13.

The drawback is that the involved transformation might significantly distort the g -function such that an originally flat surface becomes highly curved.

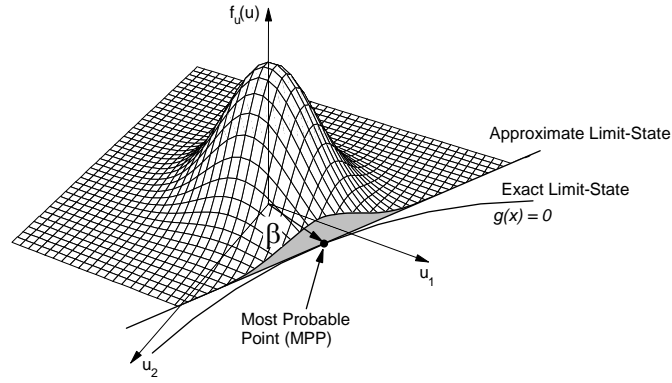


Figure 5.13 – JPDF and MPP for Two Random Variables

The transformation can be made in several ways. The most accepted methods to transform a set of correlated, non-normal variables $X = (X_1, \dots, X_n)$ to the space of uncorrelated standard normal variables $U = (U_1, \dots, U_n)$ are the Rosenblatt and the Nataf transformations. The Rosenblatt transformation (Rosenblatt, 1952) is based on the conditional distribution of the random variables:

$$\begin{aligned}
 U_1 &= \Phi^{-1} [F_1(X_1)] \\
 U_2 &= \Phi^{-1} [F_2(X_2 | X_1)] \\
 &\dots \\
 U_n &= \Phi^{-1} [F_n(X_n | X_1, X_2, \dots, X_{n-1})]
 \end{aligned} \tag{5.19}$$

where $F_i(X_i)$ is the CDF of X_i , $F_i(X_i | X_j)$ is the conditional CDF, and Φ^{-1} is the inverse CDF of a standardized normal random variable.

If the variables X are uncorrelated, then $F_i(X_i | X_j) = F_i(X_i)$ and the Rosenblatt transformation can be written as:

$$U = \Phi^{-1} [F_X(X)] \tag{5.20}$$

or, in inverse form:

$$X = F_X^{-1} [\Phi(U)] \tag{5.21}$$

Using the above transformation, the entire $g(X)$ -function can be transformed to $g(u)$ and allow the probabilistic analysis to be performed in the u -space. Numerically, however, the X -to- u or u -to- X transformations are needed only at points required to find the MPP, construct polynomials, and perform importance sampling.

The Rosenblatt transformation for dependent random variables may be impractical because the available data is often insufficient to establish the joint and the conditional probability distribution.

In case of correlated random variables, if only marginal probability distributions and correlation data are available, even for non-normal random variables, the Nataf transformation may be applied to give a set of independent normal random variables.

The Nataf method (Nataf, 1962) transforms each correlated, non-normal random variable into a normal variable and generates a new set of correlation coefficients for the transformed normal variables. The generated normal variables are then assumed to have a Gaussian joint normal density function (which is generally not true) and the correlation coefficients are used to generate a set of independent normal random variables. The inputs required for the second option include only the marginal distributions and the correlation coefficients

This transformation is performed in two steps. To transform between the original correlated X -space variables and correlated standard normals (“ Z -space”), the CDF matching condition is used:

$$\Phi(Z_i) = F(X_i) \quad (5.22)$$

Then, to transform between correlated Z -space variables and uncorrelated U -space variables, the factor L , obtained by Cholesky decomposition of the correlation matrix R , such that $R=LL^T$ is used:

$$Z = LU \quad (5.23)$$

where the original correlation matrix for non-normals variables in X -space has been modified to represent the corresponding correlation in Z -space. The Cholesky decomposition is possible provided that the covariance matrix is positive definite, which is the case as long as the random variables are not linearly dependent.

5.4.3.2.2 Step 2: Identify Most Probable Point

Once transformed random variables in the U -space, the MPP can be identified as the point on the limit state surface at the shortest distance, β , from the origin (Hasofer and Lind, 1974) or as the point that in the standard normal space has the highest probability of producing the value of limit-state function $g(U)$ (Wu, 1990). β is also referred to as the safety index in reliability analysis and the MPP becomes the critical design point.

In general, the identification of the MPP can be formulated as a standard optimization problem (i.e., find the minimum distance point subject to $g=0$) and can be solved by many optimization methods. The most widely used between them are the modified method of feasible directions (MMFD), sequential linear programming (SLP),

and sequential quadratic programming (SQP). Some have also been developed specifically for probabilistic analysis such as the Rackwitz-Feissler (1978) method (RF), that provides a convergence check based on the safety index β :

$$\frac{|\beta_i - \beta_{i-1}|}{\beta_{i-1}} \leq 0.01 \quad (5.24)$$

The RF is a Newton based method and is not guaranteed to converge. However, when the RF method converges it generally converges in far fewer function evaluations than other optimization algorithms such as SQP.

One source of numerical algorithm error in the probabilistic solution is the inability of the algorithm to locate the correct MPP. This can result for a variety of reasons such as locating a local minimum when a global minimum exists, the presence of multiple minimums, and violations of the assumptions of a smooth and continuous response surface. The challenging aspect of this error is that the problem may arise after transformation to the standard normal space. If the mapping from original to standard normal space is highly nonlinear, ill-behaved failure surfaces can be generated and can not be recognized by the analyst.

5.4.3.2.3 Step 3: Develop g-Function and Determine Failure Probability

The function $g(U)$ is approximated by a polynomial in the vicinity of the MPP.

The first-order reliability method (FORM) estimate is based on the linearization of the g-function at the MPP $U^* = (U_1^*, U_2^*, \dots, U_n^*)$ in the U -space:

$$g_1(U) = a_0 + \sum_{i=1}^n a_i (U_i - U_i^*) \quad (5.25)$$

Given $g_1(U)$, the probability of failure p_f is a function of the minimum distance β to the plane defined by g , in the u -space:

$$p_f = \Pr(g(U) < 0) = \Phi(-\beta) \quad (5.26)$$

where β is given by the relation:

$$\beta = \frac{\mu_g}{\sigma_g} = \frac{a_0 + \sum_{i=1}^n a_i \mu_i}{\sqrt{\sum_{i=1}^n a_i^2 \sigma_i^2}} \quad (5.27)$$

which is allowed to take negative values. A negative β means the origin is in the failure region (i.e., for the $p_f > 0.5$ case) and the a vector is positive from the MPP to the origin.

The above equation provides an easy correspondence between the probability estimate and the safety index. If $g(U)$ is nonlinear, a good approximation can still be obtained by the above equation, provided that the magnitude of the principal curvatures of the limit-state surface in the u space at the MPP is not too large.

If the limit-state function is highly nonlinear, the second order reliability method (SORM), based on a second-order approximation of the limit state function at the MPP can be used, which takes into account the curvature of the limit-state surface around the MPP.

$$g_2(U) = a_0 + \sum_{i=1}^n a_i (U_i - U_i^*) + \sum_{i=1}^n b_i (U_i - U_i^*)^2 + \sum_{i=1}^n \sum_{j=1}^{i-1} c_{ij} (U_i - U_i^*)(U_j - U_j^*) \quad (5.28)$$

The second order coefficient are usually computed by numerical differentiation. A special case of $g_2(U)$ is a parabola which has an exact integral solution for p_f .

The simplest of the SORM approximations $g_2(U)$, that consists in a paraboloid fitting, is due to Breitung (1984). With this approach, based on an asymptotic formula valid for large β , the probability of failure is expressed as:

$$p_f = \Pr(g(U) < 0) \approx \Phi(-\beta) \prod_{i=1}^{n-1} (1 + \beta \kappa_i)^{-1/2} \quad (5.29)$$

where κ_i denotes the i -th principal curvature of the limit state at the minimum distance point, calculated as in Figure 5.14.

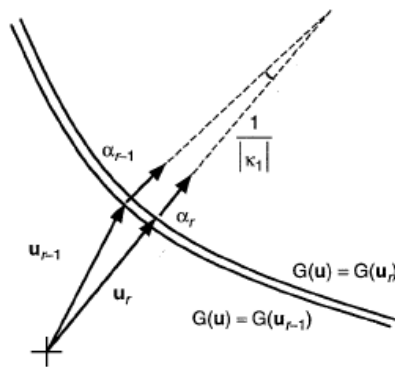


Figure 5.14 – Geometry for computing the principal curvature

In the following Figure 5.15, the procedure to obtain approximate g -functions with FORM and SORM approaches is graphically illustrated.

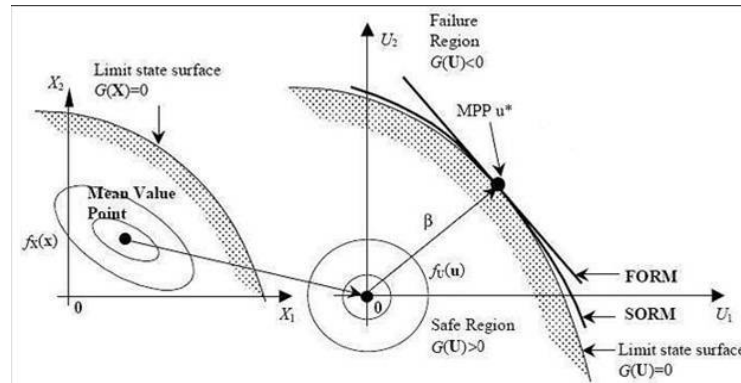


Figure 5.15 – FORM and SORM approximations of the limit state function

The FORM approach is not accurate for limit state functions with large curvature at the MPP.

SORM approaches are more accurate than FORM, but are more complex mathematically and require more failure function calculations, which may be costly.

Other first order MPP based methods are the Advanced Mean Value method (AMV) and the Advanced Mean Value method with iterations (AMV+), both developed with the aim to increase the accuracy of the rough MV estimates without introducing a too high complexity.

The AMV method improves the MV by substituting the MPP values of the random variables into $Z(X)$ and calculating an updated response.

$$Z_{AMV} = Z_{MV} + H(Z_{MV}) \quad (5.30)$$

where $H(Z_{MV})$ is the difference between the values of Z_{MV} and Z calculated at the locus of the MPPs of Z_{MV} for different z values (Wu, 1990). The Figure 5.16 presents an illustration of the AMV method.

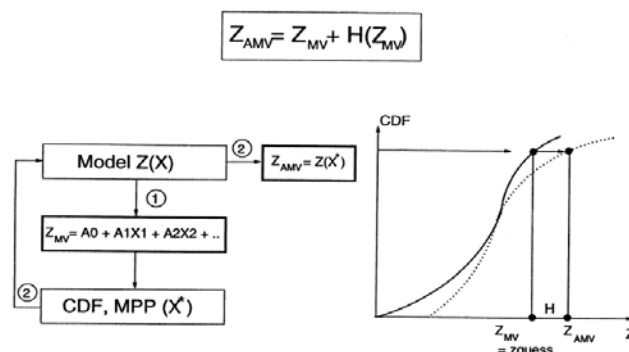


Figure 5.16 – Illustration of the AMV method

Ideally, the $H(Z_{MV})$ function should be based on the exact most-probable-point locus (MPPL) of the Z -function to optimize the truncation error. The AMV procedure

simplifies this procedure by using the MPPL of Z_{MV} . As a result of this approximation, the truncation error is not optimum; however, because the Z -function correction points are generally "close" to the exact most probable points, the AMV solution provides a reasonably good CDF estimation for many engineering application problems.

The computational steps for a point CDF analysis are:

1. Based on Z_{MV} , compute the MPP, X^* , for a selected CDF value
2. Compute $Z(X^*)$ to update z for the selected CDF value. Given the MV model, the required number of Z -function calculations equals the number of selected CDF values. The above steps require the construction of the Z_{MV} -function only once for all the CDF levels. Assuming that a numerical differentiation scheme is used to define the Z_{MV} -function, the required number of the Z -function evaluations is $(n+1+m)$, where n is the number of random variables and m is the number of CDF levels.

The AMV solution can be further improved by changing in iterative way the expansion point. The AMV+ method continues from the AMV step by iteratively recreating the approximate function about the predicted MPP until convergence (Wu, 1993):

$$Z_{AMV+} = Z(X^*) + \sum_{i=1}^n \left(\frac{\partial Z}{\partial X_i} \right) \bigg|_{X^*} (X_i - X_i^*) = b_0 + \sum_{i=1}^n b_i X_i \quad (5.31)$$

where X^* is the converged MPP for $Z = z_0$.

It is important to note that the variables X_i are generally non-normal and dependent, therefore the above AMV+ model, which is linear in the X -space, is different from the first-order reliability method (FORM) model, which is linear in the u -space.

Based on the AMV results, iteration algorithms can be used to improve the CDF estimates.

One of them, that allows to estimate CDF at specified probability level, implemented in the research code NESSUS, has been used for the probabilistic calculations based on AMV+ applications in the present work (see Figure 5.17). It derives from the standard Rackwitz-Feissler method already discussed for MPP search, but introduces further convergence checks on the variations, calculated from the last two iterations, undergone by the response Z and by the angle between the MPPs (Riha et alii, 2004; Thacker et alii, 2004).

It consists of the following steps:

- Construct a linear mean based z -function, Z_I , and search for z_0 such that $P[Z_I < z_0] = \text{fixed probability level}$.
- Use MPP of $Z_I = z_0$ and compute Z again.
- Obtain the new Z_I -function around the MPP of $Z_I = z_0$.
- Repeat the above steps until z_0 converges.

The convergence is reached when:

- The relative change in Z is less than a default (0.01) or a user defined value

z_tol

$$\frac{|Z_i - Z_{i-1}|}{Z_{i-1}} \leq z_tol \quad (5.32)$$

AND

- The measure of the angle between the MPPs from the last two iterations, θ , is less than a maximum allowable ε .

θ is defined as:

$$\theta = \cos^{-1}(\alpha_i \cdot \alpha_{i-1}) \leq \varepsilon \quad (5.33)$$

where α_i are the direction cosines to the MPP from iteration i .

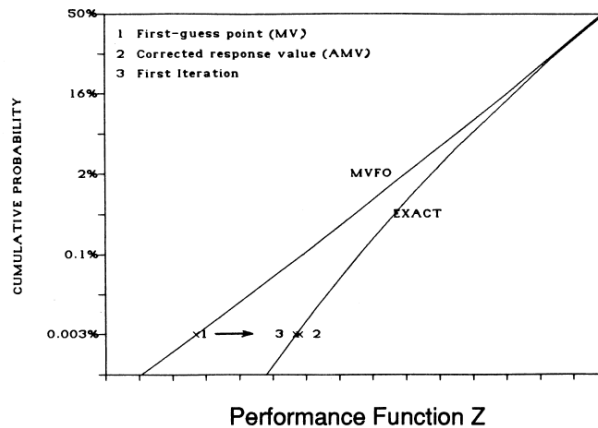


Figure 5.17 – AMV+ Iteration Algorithm for a Specified probability level (NESSUS manual, 2001)

Of course, the accuracy of these methods founded on g -function approximations depends on how well the approximate g -function represents the exact g -function (Thacker et alii, 2001). It should be cautioned that some nonlinear functions (e.g., a sine wave function) cannot be approximated well by low-order polynomials. In practice,

when a performance function is implicitly defined and is highly nonlinear, it is difficult to assess the error introduced by the polynomial approximation. Therefore, for any new type of *g-functions*, the approximate solutions should be checked using other more accurate methods ().

In Figure 5.18 two typical cases are shown for which application of linear approximation methods could lead to serious errors. On the left it is the case of a limit state function with a large curvature at the MPP: the first order method overestimates dramatically the probability of failure. In the plot on the right, the case of a non continuous performance function is presented, where the entire failure region on the top left is not considered in the determination of the p_f that results to be underestimated.

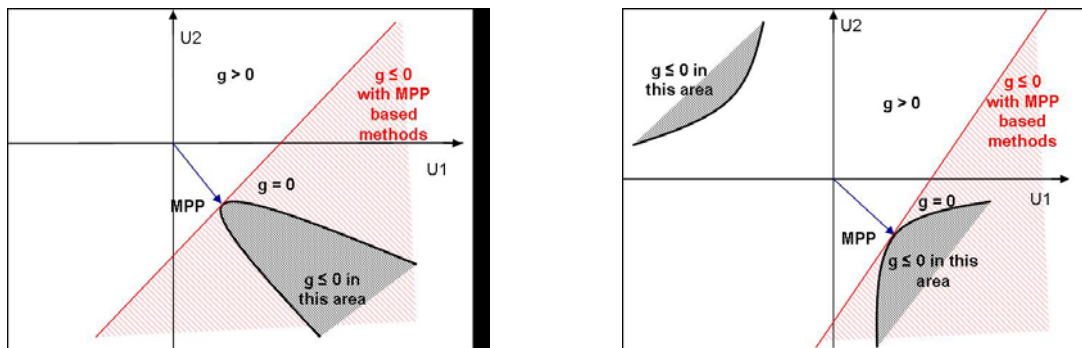


Figure 5.18 – First Order methods limits for *g*-functions not smooth and/or continuous

5.5 Reliability-based Design Optimization

In engineering design, the traditional deterministic design optimization model has been successfully applied to systematically improve the system design process, yielding a reduction of the costs and an improvement of the final quality of the products.

However, the presence of uncertainties calls for different optimization models that can yield not only an improvement in the design, but also a higher level of confidence.

A reliability-based design optimization (RBDO) model for robust and cost-effective designs can be defined using mean values of the random system parameters as design variables and optimizing the cost subject to prescribed probabilistic constraints (e.g. a maximum on the allowed probability of failure) by solving a mathematically nonlinear programming problem.

The general RBDO model can be defined as:

$$\begin{cases} \min_d \{Cost[d(\mu_x)]\} \\ \text{subject to } P_{f,j} = P(G_j(x) < 0) \leq \bar{P}_{f,j} \text{ with } j = 1 \dots m \end{cases} \quad (5.34)$$

where:

- the cost function can be any function of the mean values μ_x of the input parameters
- $\bar{P}_{f,j}$ is the probabilistic constraint that can be defined for each failure mode and needs to be satisfied.

To go in details of available robust optimization techniques is beyond the objective of the present work. however, it is just the case to underline that as a result, the RBDO solution provides not only an improved design but also a higher level of confidence in the design (Figure 5.19).

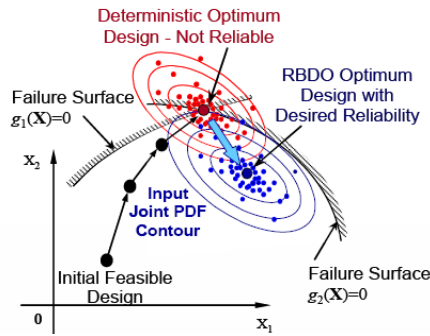


Figure 5.19 – Deterministic VS. Reliability Based Optimum

In the RBDO approach, the probability of failure for a particular design can be estimated using a methodology based on reliability analysis and design optimization through probabilistic models of relevant design parameters.

When using this optimization approach, in fact, the constraint definitions are expressed in terms of probability distributions and thus need to be evaluated, for each optimization step, within the probability framework. Thus, a reliability-based design optimization (RBDO) model for robust and cost effective designs can be defined using mean values of the random system parameters as design variables and optimizing the cost subject to prescribed probabilistic constraints (e.g. a maximum on the allowed probability of failure) by solving a mathematically nonlinear programming problem.

If the statistical distributions of the input random variables are well established (i.e. when all uncertainties or variabilities are reducible (or expected)) then all of the

uncertainties have been counted for in the design process and the result of reliability-based design would be robust in the sense that is least sensitive to the change in the statistics of the input random variables (such as the mean, standard deviation and type of a distribution) within acceptable range of cost.

6 Applications

The present Chapter deals with the application of the illustrated probabilistic methods to vibroacoustic test cases.

In the first two test examples, a probabilistic approach has been used to describe dynamic behaviour of the finite element model of a composite panel coupled to an acoustic volume. Statistical distribution of sound pressure field radiated by the panel inside the chamber in the frequency range 100-900 Hz has been evaluated once given variability of some panel's material and geometrical characteristics.

In particular, the first example shows an application of the probabilistic code NESSUS, Numerical Evaluation of Stochastic Structures Under Stress, developed by Southwest Research Institute, and illustrates opportunity and limits of the code when dealing with dynamic analysis.

The second activity concerns with the application of a Reliability-based Design Optimization procedure (RBDO) to address the variability modelling issues of the same vibroacoustic problem within the design process loop. In the RBDO approach, the probability of failure for a particular design can be estimated using a methodology based on reliability analysis and design optimization through probabilistic models of relevant design parameters. The commercial code LMS.Optimus has been used, whose opportunities and limits are here discussed.

For the last two activities, the analyzed problem has been the effect of the variabilities respectively of boundary conditions and damping material on sound transmission loss, calculated with the discrete coordinates approach discussed earlier.

The probabilistic model has been implemented in an in-house developed code, opportunely interfaced with the FE solver MSC.Nastran in order to satisfy the necessity to overcome limitation to perform analyses at fixed frequency or with time consuming methods imposed by the commercial codes.

Monte Carlo method and Advanced Mean Value methods have been applied and achieved results compared.

6.1 Analysis using NESSUS

In the first application, AMV+ and MC methods have been applied to the FE model of a composite panel coupled at an acoustic volume with anechoic properties.

The software used, NESSUS, has been originally developed by a team led by Southwest Research Institute (SwRI) as part of the NASA project entitled “Probabilistic Structural Analysis Methods (PSAM) for Select Space Propulsion Components”, that allow to effort analytical as well as finite element statistical analyses, being interfaced with many finite element commercial solvers, such MSC.Nastran. NESSUS stands for Numerical Evaluation of Stochastic Structures Under Stress but actually the code can be used to simulate uncertainties in loads, geometry, material behaviour, and other user-defined random variables to predict the probabilistic response.

Statistical distribution such as Normal, Lognormal or Weibull can be assigned to the input random variables. Many efficient probabilistic analysis methods have been devised to alleviate the need for MC (Monte Carlo) simulation, which is impractical for large-scale high-fidelity problems. The traditional methods include, for example, the first and second-order reliability methods (FORM and SORM), the response surface method (RSM), and Latin hypercube simulation (LHS). Methods tailored for complex probabilistic finite element analysis include, for example, the mean value family of methods (MV, AMV, AMV+) and adaptive importance sampling (AIS).

The aim of this application was to evaluate the statistical distribution of the sound pressure level inside the chamber due to a plane wave impinging on the panel. The plane wave has been simulated as concentrated forces spatially and uniformly distributed, in the frequency range 100-900 Hz. In the first analyses, sound pressure levels have been computed at 7 different fluid points and the spatially average value of SPL has been used as performance function for the following probabilistic analysis.

The panel dimensions were 0.600 m x 0.200 m and the panel lay-up consisted of 12 composite layers 0.24 mm thick each. The composite laminates was represented in the finite element model by 1200 CQUAD4 plate elements having 2D-orthotropic material characteristics and PCOMP element properties. The anechoic chamber dimensions were 1.400x1.000x0.700 m. The fluid inside the chamber was air and it has been represented in the finite element model by 7840 CHEXA six-sided solid elements with 3D-isotropic material properties and PSOLID element properties. PFLUID has been used in FCTN field of PSOLID properties in order to define material properties for fluid elements in coupled fluid-structural analysis.

Anechoicity condition has been simulated, rather than introducing acoustic absorbing elements included in the NASTRAN libraries, imposing an average loss factor to the acoustic fluid. This loss factor has been calculated from the following equation:

$$\eta_{fluid} = \frac{2.2}{f T_{60}} \quad (6.1)$$

where the reverberation time T_{60} can be achieved from the Sabine equation (2.112) by imposing unitary absorption on the cavity walls.

Furthermore, coincident nodes of the both fluid model and structure model were equivalenced to remove redundant nodes at the junction points. The simulations have been carried out with simply supported boundary conditions on the panel edges.

6.1.1 Complex Modal Analysis results

For the coupled system (panel plus fluid), a direct complex eigenvalue analysis has been performed in the frequency range 100-900 Hz using MSC.Nastran solution 107 and, for the panel only, a normal mode analysis has been performed in the same frequency range, using MSC.Nastran solution 103. Analysis results are shown in Table 6.1 where the influence of fluid-structure interaction on natural modes can be noted.

Achieved results have been later used to identify frequencies where to carry out probabilistic calculations.

Panel Mode	SOL 103, Panel Frequency [Hz]	SOL 107, Coupled System Frequency [Hz]
1,1	169.19	166.68
2,1	218.43	215.99
3,1	308.06	305.35
4,1	439.48	434.71
5,1	611.44	607.84
6,1	752.79	738.86

Table 6.1 - Panel and coupled system natural modes in the frequency range 100-900 Hz.

6.1.2 Frequency Response Analysis results

In order to perform a frequency response analysis of the panel, a dynamic load has been applied at all nodes in direction orthogonal to the panel surface. Response in terms of sound pressure levels has been evaluated at fluid nodes candidates for the subsequent probabilistic analysis. A flat input in the range 100-900 Hz has been obtained using the RLOAD2 MSC.Nastran entry. The chosen fluid nodes, highlighted in the Figure 6.1(a) and summarized in the Table 6.2, were at the distance of 0.05m from the panel surface.

The Figure 6.1(b) illustrates the frequency responses evaluated at the same nodes in the range 100-900 Hz.

Due to the fact that a plane wave normal to the panel excites only odd panel's structural modes, it has been noted that panel displacements had a *plane-zx* symmetry, so 6 virtual nodes have been added to selected set to evaluate the average of sound pressure.

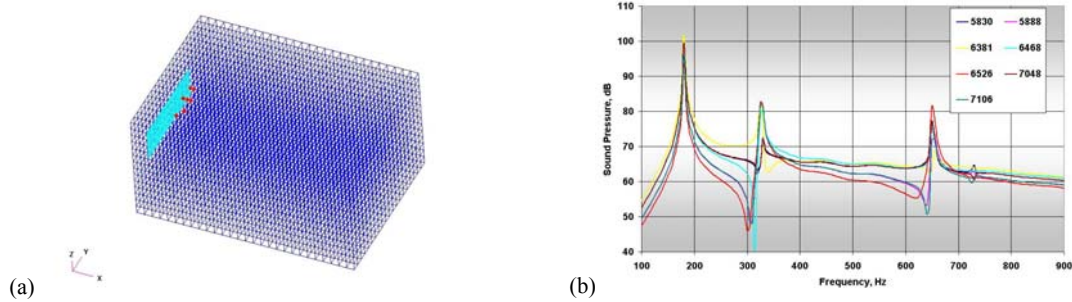


Figure 6.1 - System FE model (a) and Frequency Responses at the chosen nodes (b)

Node	x coordinate [m]	y coordinate [m]	z coordinate [m]
6381	0.05	0.50	0.35
6468	0.05	0.60	0.30
6526	0.05	0.75	0.35
5888	0.05	0.70	0.30
7106	0.05	0.70	0.40
5830	0.05	0.60	0.30
7048	0.05	0.60	0.40

Table 6.2 - Coordinates of the nodes used for frequency response analysis.

6.1.3 Probabilistic FE Analysis

The probabilistic analysis has been realized describing some of the material properties as random variables and assigning them a statistical distribution. The composite materials was composed by two types of ply: external ply was called “fabric” type and internal ply was called “tape” type.

Young modulus of composite material plies both along the fibre direction and in transverse direction, have been simulated as Normal distributed, with random variables named respectively E_{f1} and E_{f2} for “fabric” plies and E_{t1} and E_{t2} for “tape” plies. The shear modulus G_{12} and the density ρ for both types of plies has been described with a Normal distribution. The standard deviation for all the variables has been posed to be the 10% of the respective mean values.

“Tape” material properties variables have been considered to be correlated between themselves and the same considerations have been done for “fabric” material properties variables.

Instead, “fabric” and “tape” materials have been supposed separately produced, thus correlation coefficients between the different materials have been chosen equal to zero. In the following Table 6.3 the correlation matrix is summarized.

	E_{f1}	E_{f2}	G_{f12}	ρ_f	E_{t1}	E_{t2}	G_{t12}	ρ_t
E_{f1}	1							
E_{f2}	1	1						
G_{f12}	1	1	1					
ρ_f	0.5	0.5	0.5	1				
E_{t1}	0	0	0	0	1			
E_{t2}	0	0	0	0	1	1		
G_{t12}	0	0	0	0	1	1	1	
ρ_t	0	0	0	0	0.5	0.5	0.5	1

Table 6.3 – Correlation matrix

NESSUS, at least for MSC.Nastran interfaced analyses, allows to perform only analysis at single fixed frequency. Then, in order to calculate dynamic response at different frequencies and for different nodes, it has been chosen to perform a separate analysis for each frequency using as performance function the average sound pressure calculated on 13 nodes (7 real and 6 virtual nodes).

In order to investigate the applicability of MPP based methods, it has been verified if the performance function versus its variables was smooth and continuous.

It has been noted that if sound pressure levels are calculated at a frequency where in nominal conditions one of the panel resonances occur, the assumptions mentioned above are not verified (see Figure 6.2), whereas at frequencies far from panel resonances, the performance function has smoothness and continuity characteristics (see Figure 6.3)

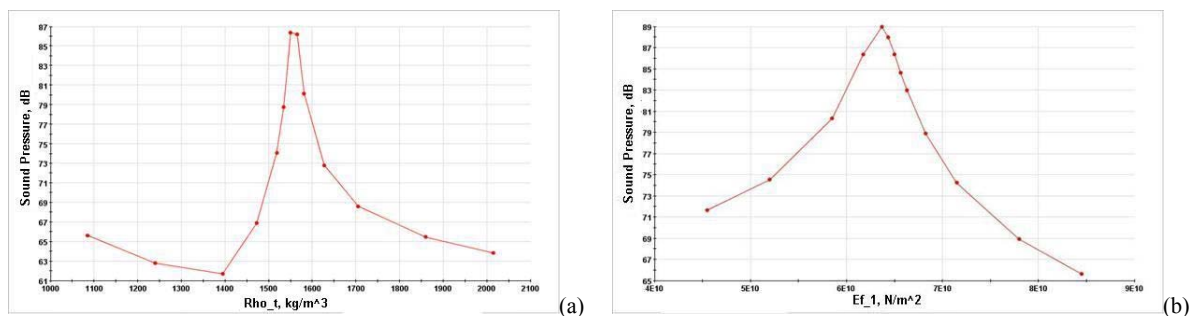


Figure 6.2 - Sound Pressure versus ρ_t (a) and E_{f1} (b) close to a system proper frequency

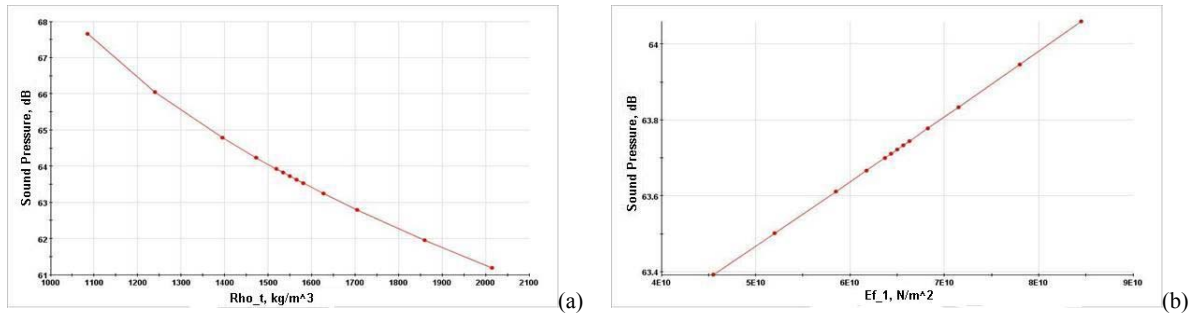


Figure 6.3 - Sound Pressure versus ρ_t (a) and E_{f1} (b) far from a system proper frequency

The highly non-linear behaviour of the sound pressure at frequencies close to the “resonances” can be explained with the fact that the analyses are performed at fixed frequencies, identified by the frequencies at which, in nominal conditions, panel’s modes in the coupled analysis occur. When a panel’s mode occur, the radiated sound pressure has a maximum. Now, if a parameter in the input model, for instance the panel’s density, is changed, the panel’s modes will have a frequency shift but the analysis will be carried out at the same frequency as before, at which the panel will not have anymore a vibrating mode. Its radiated pressure, then, will be much lower.

On the other hand, preliminary runs showed that, if correctly applicable, AMV+ method analysis constitutes a good compromise between accuracy and efficiency.

Trying to avoid performance function’s sharp behaviour, a subsequent analysis has been performed using as performance function the average sound pressure calculated on three values belonging to the same one-third octave band and chosen as far as possible from panel’s modes frequencies.

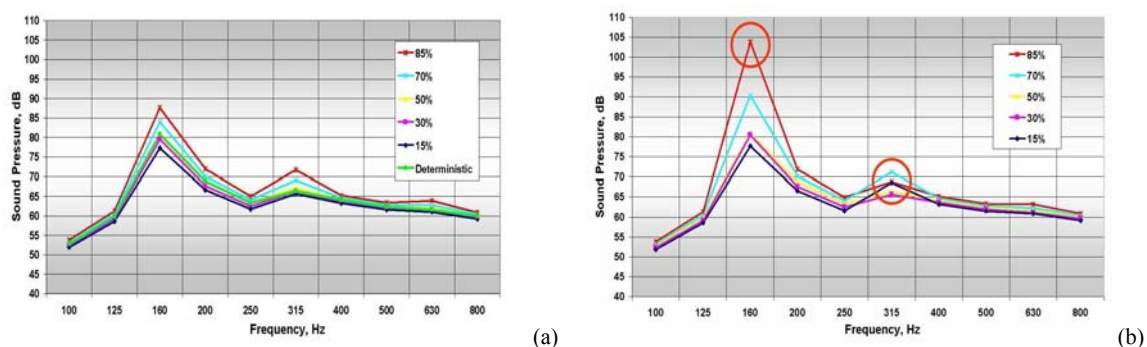


Figure 6.4 - Average sound pressure in third octave bands, MC (a) VS. AMV+ (b)

With this new aim, it has been tried to apply AMV+ method, comparing the achieved results with ones coming from application of the MC, Figure 6.4(a).

Even if selected frequencies were as far as possible from resonances, some bands were not large enough to choose frequencies far enough to obtain the AMV+ method

convergence, as it can be seen in Figure 6.4(b). In these cases, MC method has to be used. Comparing the results achieved by AMV+ and MC analyses in the one-third octave bands centred at 160 Hz and 315 Hz, it appears clear that AMV+ results are not reliable. In the 160 Hz band, in fact, the convergence was not reached whereas in the 315 Hz one-third octave band, CDF monotonicity property has been violated: the pressure value at 15th percentile must be absolutely less of values associated to higher percentages of probability.

Relative errors have been evaluated in the analyzed one-third octave bands for probability levels between 15% and 85%, to understand significant difference between two methods:

$$\varepsilon = 100 \cdot \frac{SPL_{AMV+} - SPL_{MC}}{SPL_{MC}} \quad (6.2)$$

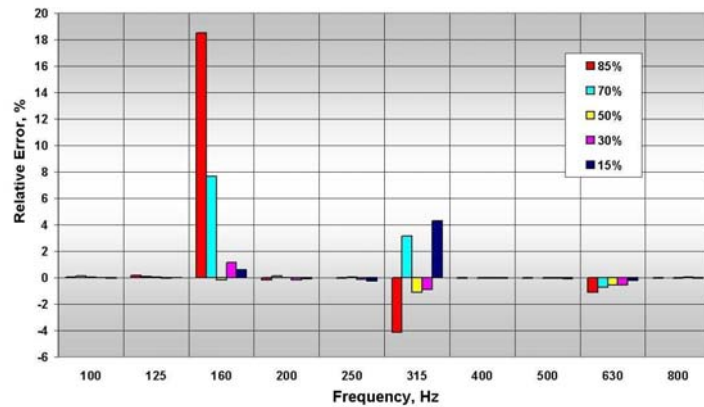


Figure 6.5 – Relative errors between AMV+ and MC evaluations

It is worth to notice that, as it was expected, maximum errors have been achieved in the third octave bands where a resonance frequency was present. In the bands where no panel resonance occur the errors are negligible. This fact allows to highlight that, for the present problem, it is possible to use AMV+ method, with good reliability, if and only if the frequency where to evaluate the response is not a resonance frequency or a frequency close to it.

In a more general context it seems that it is possible to integrate AMV+ results, achieved where performance function has smoothness and continuity properties, with results coming from application of MC method, obtaining in this way a trade-off between method predictions robustness and computational effort.

Integrating both AMV+ and MC methods results depicted in Figure 6.6 have been obtained. It is important to notice that, with a maximum error of 0.2%, using this hybrid method is possible to predict the same acoustic levels achieved by MC method.

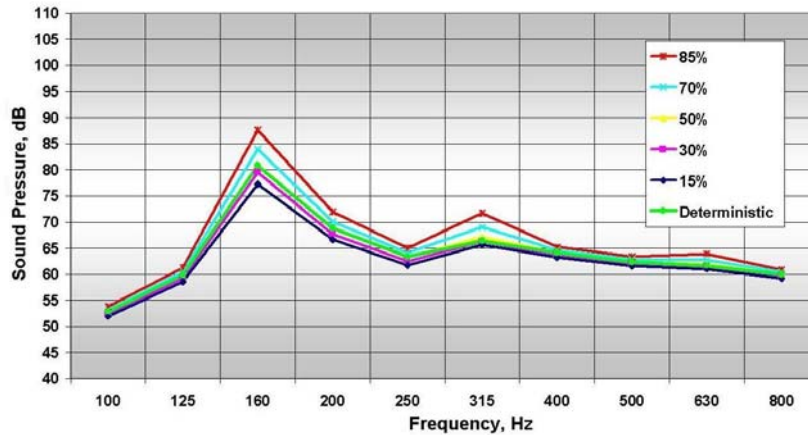


Figure 6.6 – Mixed AMV+ and MC probabilistic frequency response

The lesson learned from this first application of probabilistic methods to a vibroacoustic finite element model was that a similar approach allows to identify the range of variation of the dynamic response in function of possible values undertaken from the input variables. It could be also possible to predict maximum vibration as well as acoustic levels that can be reached in a given configuration. Some drawbacks of advanced mean value methods were highlighted, related to the fact that this methods do not give any information about the error and have to be used very carefully.

Furthermore, the NESSUS code, was not convenient to be used for frequency response analyses: a complete probabilistic analysis was requested for each frequency, so that computational time was increased by a factor depending by the number of frequencies at which analysis was performed., Besides, the need to take as performance function the sound pressure behaviour at single frequencies have made the analysis too strictly dependent from the frequency chosen.

6.2 Analysis using OPTIMUS

Next analysis project has been built around a finite element model of a composite aerospace panel with a viscoelastic damping layer embedded, simply supported along the edges and coupled to a model of an acoustic chamber (Polito et alii, 2007).

In this application, other than probabilistic analysis with a Response Surface approach, a reliability based optimization has been performed.

6.2.1 Deterministic analysis

The plate and the volume were meshed in order to model the relative wavelengths up to 1500 Hz. A frequency response analysis has been performed in the range 100-1000 Hz, considering a mechanical excitation that simulates a plane wave acting on the panel and evaluating radiated pressure in the fluid volume.

The panel dimensions were 24x8 inches and the lay-up is showed in Figure 6.7. Between the two main sub-panels, the presence of a viscoelastic layer 0.2 mm thick has been modelled.

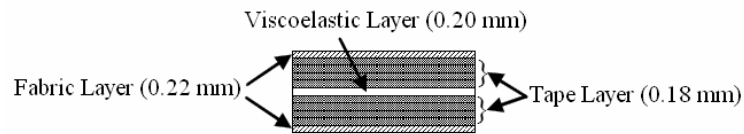


Figure 6.7 – Composite panel lay-up structure

The composite laminates on both sides have been modelled with 4800 CQUAD4 plate elements having 2D-orthotropic material characteristics and PCOMP element properties. The viscoelastic core consisted of 4800 CHEXA six-sided solid elements with 3D-isotropic material properties and PSOLID element properties.

A detailed view of the panel FE model is given in Figure 6.8.

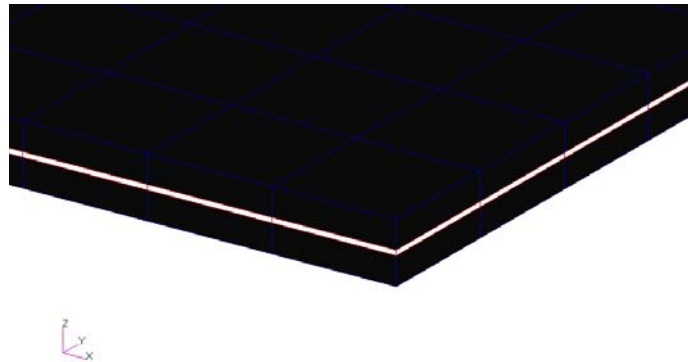


Figure 6.8 – Composite panel FE model: lay-up details

The use of solid element to simulate viscoelastic core is due to the fact that shell elements are not able to reproduce high shear that is present through the thickness. In fact, when a viscoelastic damping material layer is embedded in a sandwich structure, the difference in the extension of two stiff layers induces high shear levels in the viscoelastic layer.

The coupled model was assembled by using the capability of the MSC.Nastran of connecting non matching meshes for the structural-acoustic coupling (ACMODL card

with DIFF option). In the following Figure 6.9 a global view of the coupled model (a) and a detail of the non-matching structural-acoustic interface (b), are illustrated.

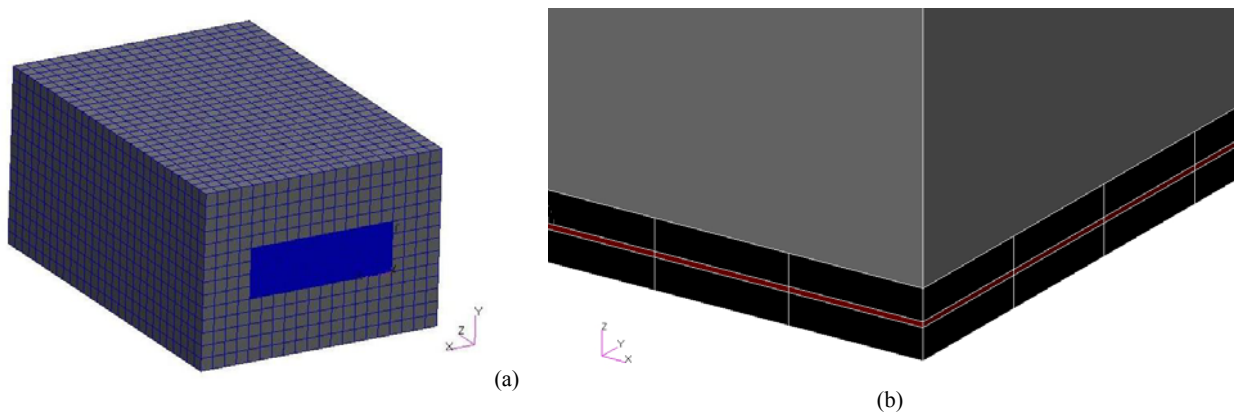


Figure 6.9 – Finite Element model of the composite panel and the anechoic chamber

In the frequency response analysis performed, several positions distributed on a plane at 50 mm from the panel have been chosen as target where to evaluate with probabilistic approaches, as it will be showed in the following, pressure levels and their frequency of occurrence.

Both the direct and the modal approaches for frequency analysis have been implemented. In both cases the highest pressure levels have been reached at the frequency where the first panel mode occurs.

The modal approach, where the frequency response is calculated starting from the complex eigenvalues and eigenvectors of the system, has been later preferred because of the much lower computational time.

The Figure 6.10 illustrates the sound field radiated from the vibrating panel in the cavity at two different frequencies.

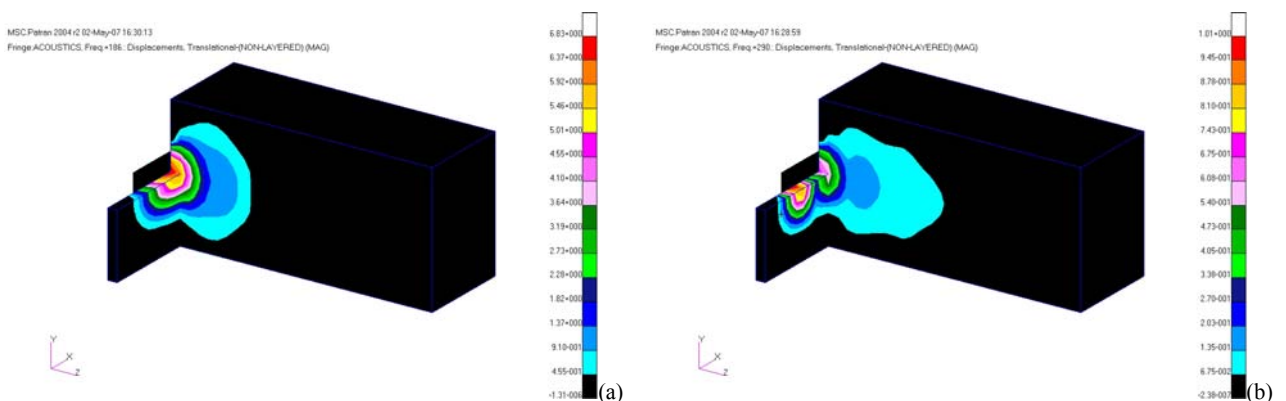


Figure 6.10 - Fringe acoustic plot of the acoustic pressure at 186 Hz (a) and 290 Hz (b)

6.2.2 Probabilistic FE Analysis

Physical variables have been modelled in the analysis project with probability distribution functions in order to characterize the variabilities concerned with the material properties of the various layers.

A total of 8 input parameters have been considered, as reported in the following Table 6.4.

Property	Distribution	Mean	Coeff. Of Variance
Tape E ₁	Normal	Undisclosed	10%
Tape E ₂	Normal	Undisclosed	10%
Tape Density ρ_T (rhoT)	Normal	Undisclosed	10%
Fabric E	Normal	Undisclosed	10%
Fabric Density ρ_F (rhoF)	Normal	Undisclosed	10%
Viscoelastic Material Shear Modulus G	Normal	Undisclosed	10%
Viscoelastic Material Density ρ_V	Normal	Undisclosed	10%
Viscoelastic Material Loss Factor η	Normal	Undisclosed	10%
Table 6.4 - Statistically characterized material properties for the composite panel			

The variability of the input parameters has been taken into account with a parameterization of the FE model. In fact, in order to perform a probabilistic characterization of the response of the system and reliability analysis and optimization procedures, the vibroacoustic analysis has been performed a number of times with different values of the input parameters.

The response of the system in terms of the acoustic pressure has been computed in the frequency range 100-1000 Hz for each point of the set of locations selected inside the anechoic chamber. A mean frequency response function (FRF) has been computed based on the FRFs of each point and, from this mean FRF, the maximum value of the acoustic pressure, P_{dB} , has been selected as representative of the performance of the system, that is, the performance function. Also, the frequency at which this maximum occurs has been taken into account.

Following the previous considerations, the choice of the limit state function is related to the selection of a threshold for P_{dB} . For this case, a value of 108 dB has been selected. The limit state function can then be written as:

$$G = 108 - P_{dB} \quad (6.3)$$

With this choice, the *G-function* is negative where P_{dB} is higher than 108 dB: to exceed the fixed sound pressure thresholds corresponds to a “failure”.

Also, a design exploration strategy has been adopted together with a response modelling approach to speed up the reliability analysis and optimization process. In fact, as significant computational effort is required for each vibroacoustic response evaluation, a hybrid meta-model/FE strategy has been used to limit the overall CPU time. Two DOE plans have been prepared and the necessary computations performed. These plans have been designed in order to explore the acoustic pressure response within the boundaries of interest. The first plan is a Central Composite Inscribed (CCI) that requires 273 experiments for the 8 input parameters. The second plan is a Latin Hypercube that samples the input parameters space with 250 experiments. Subsequently, a Response Surface (RS) model has been computed based on the DOE results. The obtained meta-model has then been used for a first reliability assessment and for the RBDO process.

The outline of the procedure used for the analysis has been as follows:

1. Compute the response of the structure with 2 DOE plans
 - a. Compute the Central Composite Inscribed DOE plan in the range $[-3\sigma, +3\sigma]$
 - b. Compute a Latin Hypercube DOE plan in the range $[-3\sigma, +3\sigma]$
2. Compute the least squares Response Model (using Taylor Approximation)
3. Perform a reliability assessment of the nominal design
4. Perform an RBDO loop using the RS model and obtain a first tentative optimum point.

It has to be noted that the optimization process implemented is a deterministic process with a probabilistic constraint. Thus the result is an optimum point that is also robust with respect to the required failure probability.

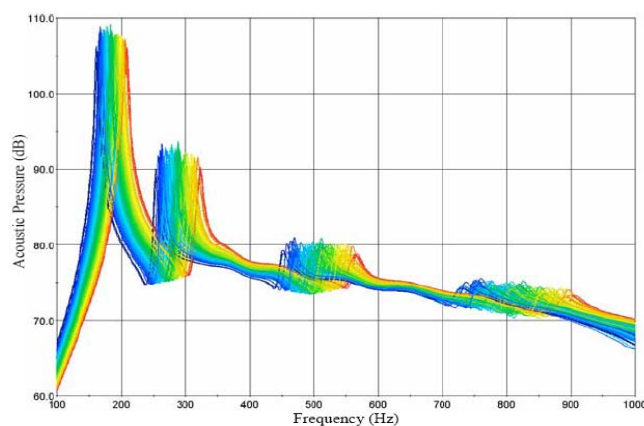


Figure 6.11 – FRF Variability for the explored range of variation of the input parameters

For each iteration of the reliability assessment and optimization processes, the evaluation of the performance function at specific values of the input parameters is required. Thus a sequence of vibroacoustic analysis (for the present case the MSC.Nastran FE solver has been used) is performed, together with results extraction and the identification for each evaluation of both the maximum acoustic pressure and its frequency.

Using the results of the DOE plan, two least squares cubic Taylor Response Surfaces (RS) have been computed to approximate the system responses. The first response surface approximates the maximum acoustic pressure in the frequency range of interest (Figure 6.12), while the second response surface approximates the frequency at which the maximum acoustic pressure occurs (Figure 6.13). The response surfaces have been used as meta-models for the reliability assessment.

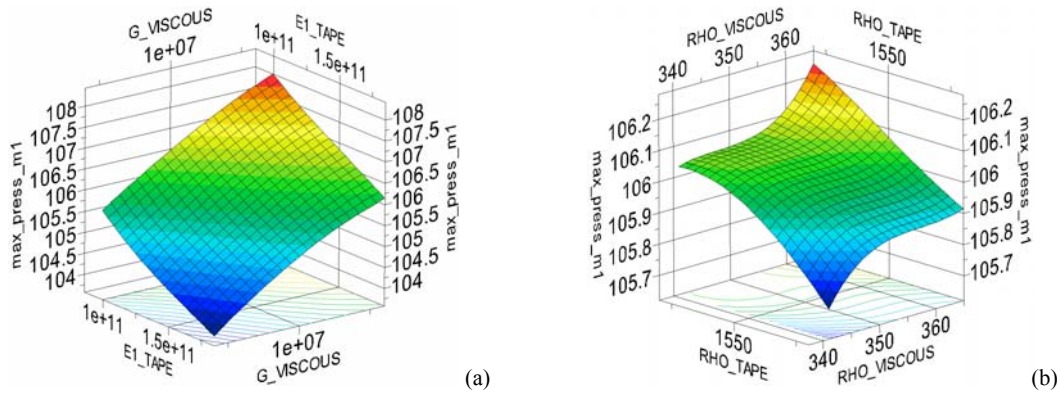


Figure 6.12 - Sections of Response Model (RM) for the Maximum Acoustic Pressure

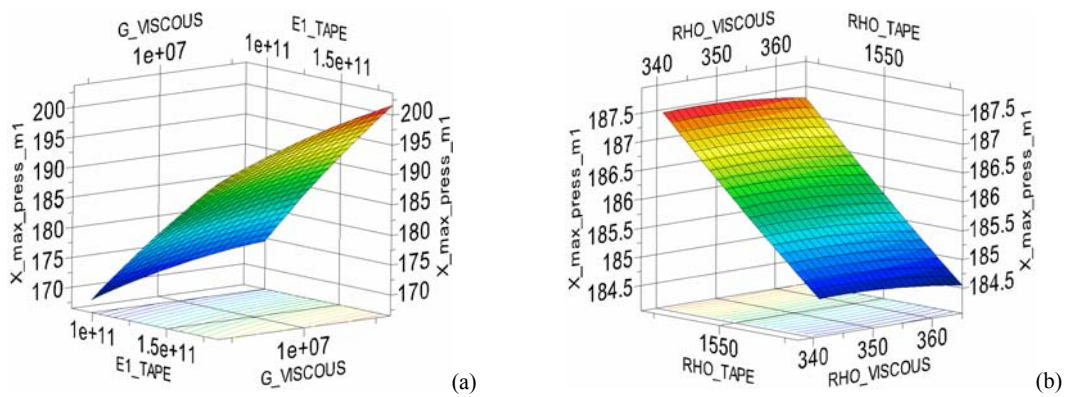


Figure 6.13 - Sections of RM for Max Acoustic Pressure's frequency of occurrence

For each response model, quality indexes have been computed to verify the fitting and prediction accuracy within the limits of the domain of definition of the models. In particular, three regression parameters have been computed: R^2 , R^2_{adj} and R^2_{press} . The values of the regression parameters are showed in Table 6.5.

	R^2	R^2_{adj}	R^2_{press}
Maximum Acoustic Pressure Model	0.9963	0.9946	0.9916
Frequency of Max Pressure Model	0.9995	0.9995	0.9994

Table 6.5 - Regression parameters for the two response model

Values of R^2 and of R^2_{adj} close to 1 mean that the model well fits the values of the simulation points. The third parameter, R^2_{press} indicates the predictive capability of the model. Basically it gives a measure of how good the model will predict values for points that were not simulated yet. If the value of R^2_{press} is close to 1, it indicates that the model will perform well for points that were not simulated. Further details on the use of these regression parameters can be found in (Myers and Montgomery, 1995).

Using the two response models, a probabilistic characterization of the maximum acoustic pressure and of its frequency has been carried out. For this purpose, a Monte Carlo simulation has been performed on the RS models using 50000 samples (Figure 6.14).

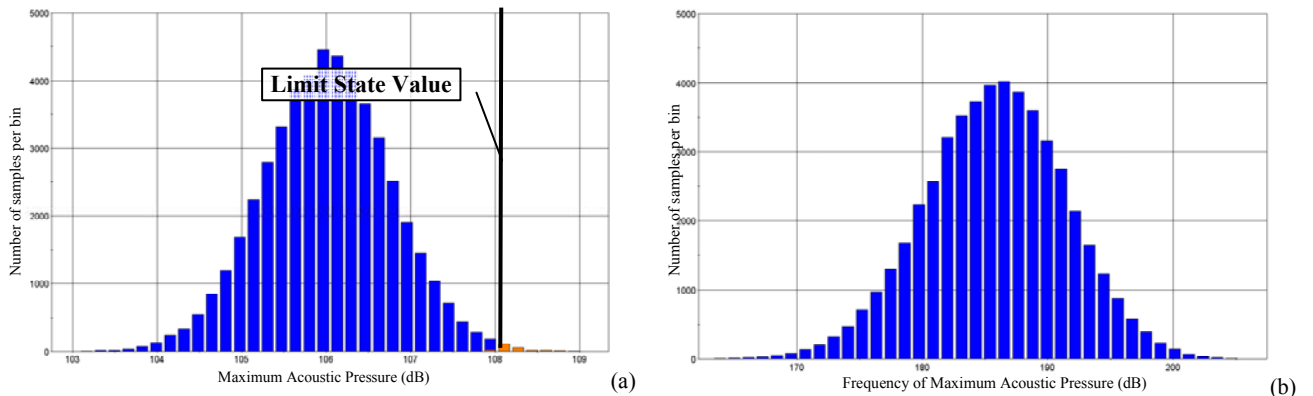


Figure 6.14 - Histograms of the Maximum Acoustic Pressure and of its frequency of occurrence

6.2.3 Robust optimization results

The target of the optimization process performed applying the RBDO method was to enforce a distance of 5σ from the limit state value of the acoustic pressure of 108dB (see equation (6.3)), meaning that the new design found will have, given the scatter in the input parameters, a probability of $2.8665 \cdot 10^{-7}$ of having a maximum mean acoustic pressure greater than 108dB.

In the approach used, the probabilistic constraint is enforced since the first optimization step. As a consequence, the probability of failure for each step of the optimization procedure has to be assessed in order to check that the probabilistic constraint is not violated.

The optimization process has been carried out using a sequential linear programming (SQP) algorithm and looking for a robust optimum point in the range $[-3\sigma, +3\sigma]$ for each parameter.

The results of the optimization are reported in Table 6.6 and are shown in Figure 6.15.

SQP Iteration	Start	1	2
Tape E1	0σ	0.4265σ	0.5753σ
Tape E2	0σ	-0.0717σ	-0.0781σ
Tape Density ρ_T (rhoT)	0σ	-0.1165σ	-0.1144σ
Fabric E	0σ	0.0752σ	0.0973σ
Fabric Density ρ_F (rhoF)	0σ	-0.0516σ	-0.0585σ
Viscous Material G	0σ	-0.4783σ	-0.6348σ
Viscous Material Density ρ_V (rhoV)	0σ	-0.0232σ	-0.0278σ
Viscous Material Damping Coefficient	0σ	1.9040σ	2.3352σ

Table 6.6 – RBDO results

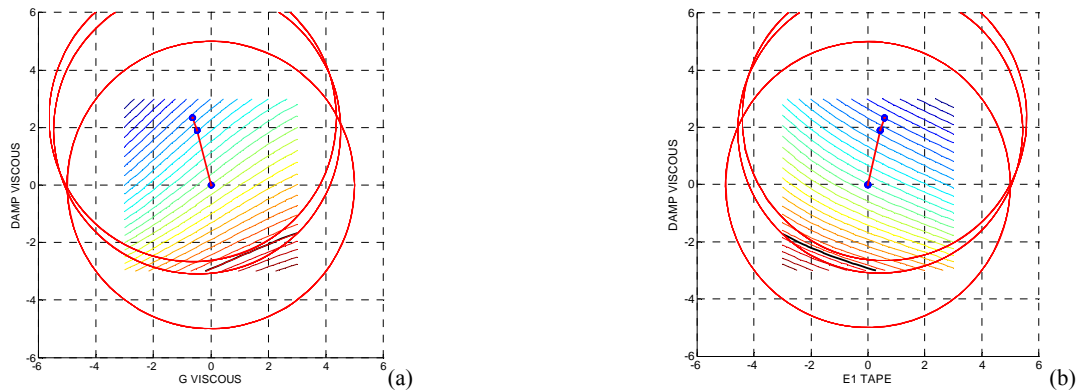


Figure 6.15 - Results of the Reliability-based Design Optimization in the standard normal space

6.3 Analysis using in-house developed code

From the discussed applications it appears that explored commercial codes present some drawbacks when applied to vibroacoustic test cases.

The NESSUS, in fact, implements many probabilistic methods but, being suited for other applications, allows only for analyses at fixed frequencies.

On the other hand, OPTIMUS as well as other commercial optimization codes implements only the time consuming Monte Carlo and other simple methods, such as the FORM and the Response Surface method applied in this work.

For these reasons, it came out the necessity to develop an in-house probabilistic code that could allow to overcome limitations imposed by commercial codes.

It has been written a MATLAB code that is interfaced with the finite element commercial solver MSC.Nastran.

The Monte Carlo method and more efficient Most Probable Point based methods, belonging to the advanced mean value family methods, have been implemented.

Depending from the type of analysis method chosen, the code generates a set of input files for the finite element external code (.bdf files for MSC.Nastran) based on different realizations of input random variables. Results in terms of displacements, stresses or natural frequencies can be directly read from each of the MSC.Nastran output files and used to perform probabilistic analysis.

Two applications are presented where a probabilistic analysis has been carried out to evaluate the effects of variabilities on calculated transmission loss of a panel.

In the examples discussed in this work, for each realization of the input variables, a FE normal mode analysis of the panel is performed. The results in terms of eigenvalue and eigenvectors are then used to calculate the sound transmission loss in discrete coordinates, as defined in section 2.2.

In the first test case, panel's boundary conditions variability has been simulated introducing a non infinite stiffness in the direction of the panel's normal. This with the aim to represent the real case in which the installation of the panel in the TL window is not perfectly reproducing theoretical simply supported conditions.

The second application deals with the prediction of the effects of variable stiffness and damping properties of a viscoelastic material, embedded in a composite panel, on acoustic performances of the sandwich.

Before going into details of the applications studied, it is important to evaluate which is the degree of correlation between experimental measurement performed in the SMARF and TL prediction method proposed.

6.3.1 TL numerical-experimental correlation

In order to validate discrete coordinate approach implemented for TL calculations, a FE model of the 1.5 mm thick aluminium panel, simply supported along its edges, has been realized. The plate was initially very fine meshed with 50x20 elements in order to model wavelengths up to 6000 Hz.

Applying the relation (4.1) for mesh sizing, in fact, it results:

$$\Delta_{x,y} \leq \frac{\lambda}{4} = \frac{c_b}{4 f_{\max}} = \frac{\sqrt{2\pi f_{\max}}}{4 f_{\max}} \sqrt[4]{\frac{Eh^2}{12\rho(1-\nu^2)}} \quad (6.4)$$

By substituting typical values of aluminium alloy elastic and mass properties, it results that $\Delta_{x,y} \leq 0.0123 \text{ m}$.

Thus, for a panel $0.600 \times 0.200 \text{ m}$, at least 49×16 elements must be used when performing analysis up to 6000 Hz .

A normal mode analysis has been carried out and achieved results used to calculate the sound transmission loss in the frequency range $0\text{-}4500 \text{ Hz}$.

Of course, a FE approach was not suitable to numerically predict the TL behaviour at higher frequencies, because of the need to overly increase the number of model's degrees of freedom.

In the following Figure 6.16, the numerical TL obtained, opportunely corrected to account for field incidence, is compared with experimental one.

To allow for comparison, numerical TL, calculated with a frequency resolution of 2 Hz , has been expressed in one-third octave bands.

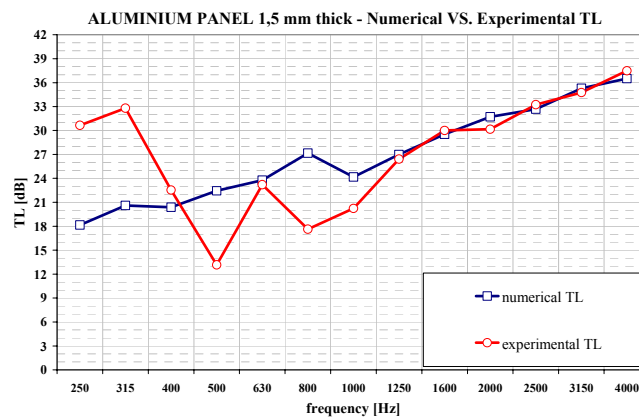


Figure 6.16 – Numerical VS. experimental TL in one-third octave bands, panel 1.5 mm

From the numerical-experimental correlation it can be observed that:

- In the low frequency range there is a discrepancy between the results being the sound field not enough diffuse
- Above 1000 Hz the numerical behaviour fit very well the experimental one
- No information is available for frequencies less than 250 Hz , that is the range where first panels modes occur

- No information is available for frequencies higher than 4000 Hz, considering that coincidence frequency for the analyzed 1.5 mm thick panel is around 8000 Hz.

6.3.2 Effects of boundary conditions variability on predicted TL

It's very common that TL numerical-experimental correlation problems in the low frequency range deal with panel's installation in the TL window.

Although measurement standards as ASTM E90 give specific indications about test specimen installation procedure, it can happen that experimental boundary conditions do not replicate ones as in the ideal case, that can have an effect on measured TL.

When the area of the test specimen, for example, is smaller than that of the normal test opening, the area of the test opening is usually reduced using an additional construction, a filler wall, that can be less stiff of the typical supporting frame. Furthermore, presence of gaps or fissures around the periphery of a specimen can occur. These are commonly sealed with clay or adhesives, that introduce uncertainties about the panel's operative boundary conditions.

During the experimental campaign discussed in the chapter 3, it occurred some discrepancies between expected and measured dynamic behaviour of an aluminium panel 2 mm thick.

The results of an experimental modal analysis performed on this panel installed in its test window showed to be bad correlated with numerical ones, achieved by a FE model of the panel itself with pinned boundaries. In this case, panel boundary conditions were far to be simply supported along the edges: some positions on the panel perimeter seemed to be not constraint at all to the fixture.

In Figure 6.17 the achieved first two experimental mode shapes are compared with numerical ones (a, b) and the calculated Modal Assurance Criterion (MAC) index for the first three modes is presented (c).

This latter index, defined in equation (6.5), represents a measure of the correlation between experimental and numerical mode shapes (see, for example, Ewins, 1984).

$$MAC(x, p) = 100 \cdot \frac{\left| \{\psi_x\}^T \{\psi_p\}^H \right|^2}{\left(\{\psi_x\}^T \{\psi_x\}^H \right) \left(\{\psi_p\}^T \{\psi_p\}^H \right)} \quad (6.5)$$

Where $\{\psi_x\}$ and $\{\psi_p\}$ respectively are the panel's experimental and numerical modes.

A MAC value of 100 stands for perfectly correlated mode shapes.

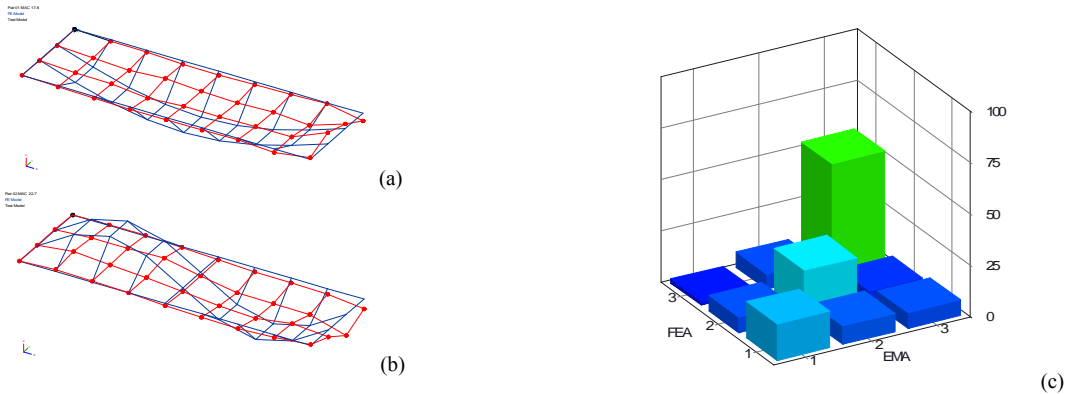


Figure 6.17 - Modal Analysis results, for the aluminium panel 2 mm thick

For other panels, instead, there was a good agreement between experimental and numerical modal analysis results in terms of mode frequencies, mode shapes and MAC index, as it can be seen from the Figure 6.18.

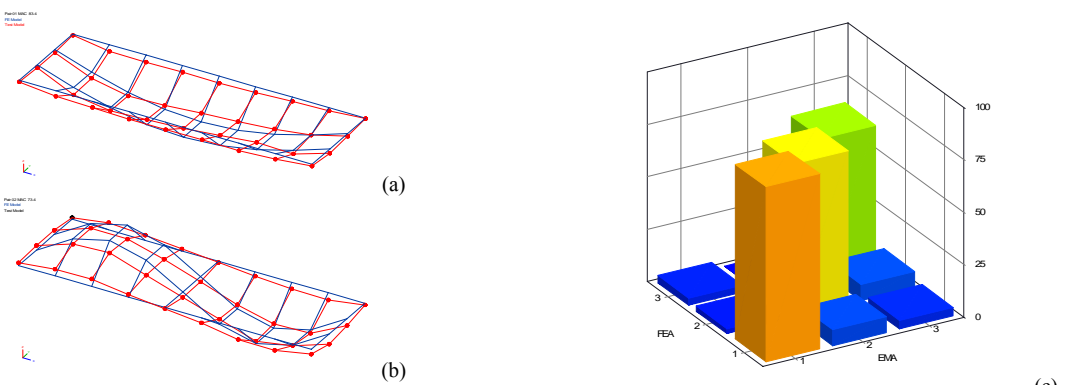


Figure 6.18 - Modal Analysis results, for the aluminium panel 1 mm thick.

The question that arises is about if it is possible to simulate the effect of variability in panel's boundary conditions on its acoustic behaviour, trying to address if weak constraints in direction of panel's normal can be responsible of discrepancies from expected results.

Aiming to assess how much the panel's boundary conditions can affect TL behaviour, it has been performed a probabilistic numerical simulation assuming the boundary conditions as stochastic variables (Polito, 2007)..

Monte Carlo and Mean Value Family methods have been applied to FE model of a 1 mm thick aluminium panel, calculating variation on TL due to parameters variability in the range 0-1000 Hz.

The model has been meshed with the aim to analyse panel's modal behaviour up to 1500 Hz. The choice of using a mesh coarser than the one discussed in the previous paragraph was due to computational requirements.

To allow for simulation of the experimentally evidenced boundary conditions, panel translations in the direction of its normal were not completely constrained. This has been implemented by introducing, in the panel FE model, spring elements along the edges. The springs have been divided in two different groups in order to simulate different constraint stiffness, see Figure 6.19.

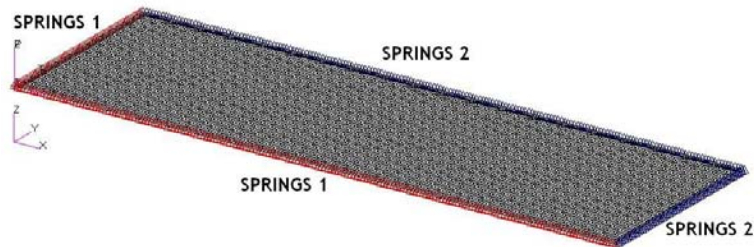


Figure 6.19 – FE model with springs along the edges

Being not known a priori the stiffness values to assign to the spring elements, these values have been chosen as random variables normal distributed. The simulations performed are summarized in the following Table 6.7.

The minimum value of transmission loss achieved in one-third octave bands in the frequency range 40-1000 Hz has been chosen as performance function.

Run	Method	$k_{1,2}$ =Mean Springs 1, 2 [N/m]	$s_{1,2}$ =Std Deviation Springs 1, 2 [%]
1	Monte Carlo	1.0 E+4, 1.0 E+4	5, 5
2	Monte Carlo	1.0 E+3, 1.0 E+3	5, 5
3	Monte Carlo	1.0 E+4, 1.0 E+3	5, 5
4	Monte Carlo	1.0 E+4, 1.0 E+3	5, 15
5	MV, AMV, AMV+	1.0 E+4, 1.0 E+4	5, 5
6	MV, AMV, AMV+	1.0 E+3, 1.0 E+3	5, 5
7	MV, AMV, AMV+	1.0 E+4, 1.0 E+3	5, 5
8	MV, AMV, AMV+	1.0 E+4, 1.0 E+3	5, 15

Table 6.7 - Probabilistic analysis performed

In the Figure 6.20, the transmission loss behaviours calculated with Monte Carlo method are presented. It can be seen that the variations in the TL values are below 2 dB, except in the case of the run 4 where the standard deviation for the spring 2 is very high.

These higher variations of the calculated TL are, in any case, limited in the very low frequency range ($f < 150$ Hz). For higher frequencies, the stiffness of the springs has a small effect on the radiated sound

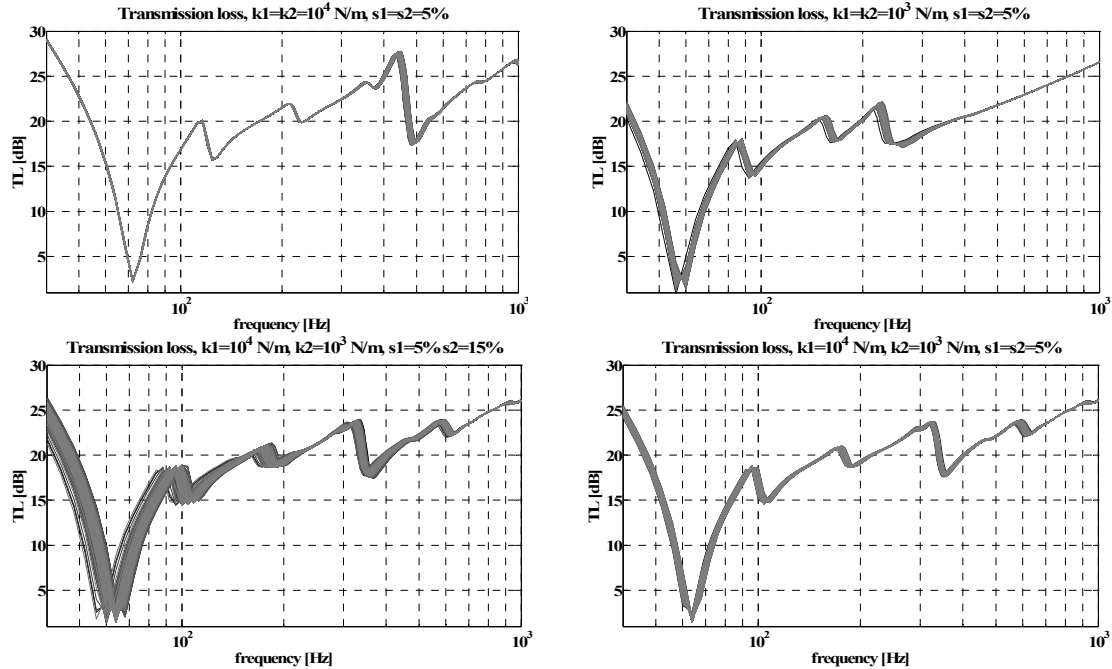


Figure 6.20 - TL results for the runs 1-4 (from the top left, clockwise)

Even lower are computed variations of the performance function, that, as already stated, is the minimum value of the transmission loss predicted in one-third octave bands (Figure 6.21)

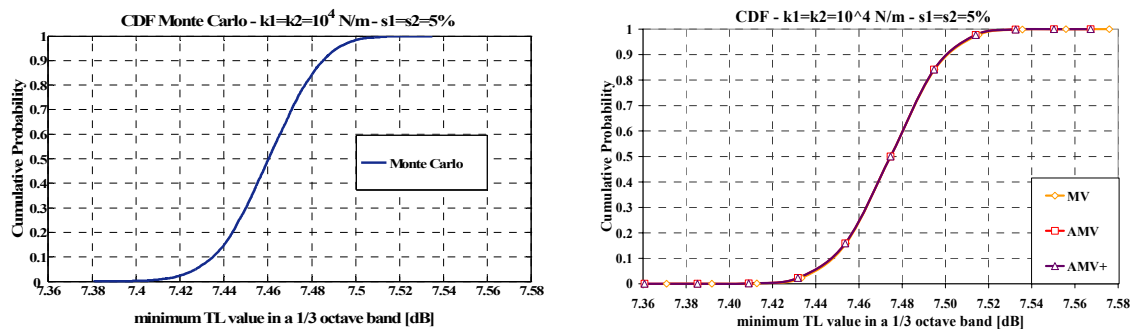


Figure 6.21 - Probabilistic results in terms of CDF, for the runs 1 (left) and 5 (right)

This is because the main effect of the stiffness variations seems to be a translation along the frequency axis of the TL curve more than an amplitude change of the minimum TL value.

The mean value based methods led to similar results with respect to MC, even if the first methods account for a lightly wider range of variation of the performance function, that can be due to an overestimate of performance function's distribution tails.

From achieved results it can be stated that variable boundary conditions due to non perfect installation of the test panel could have effects only at very low frequencies, where in any case it is not possible to perform reliable measurements with a small facility.

Discrepancies between measured and numerically predicted TL below 1000 Hz seem to be due to a modal behaviour of the acoustic chambers, related to a sound field not completely diffuse, rather than to the panel's constraints. In this frequency range the SMARF facility can be useful to perform comparison between different solutions (e.g. damping treatments) but it appears to be not suitable to calculate absolute quantities.

A much higher effect can have on the TL the variation of other panel's properties: in Figure 6.22 results obtained introducing as normal distributed random variables panel thickness ($\mu=0.001$ m, $\sigma=5\%$) and damping coefficient ($\mu=0.01$, $\sigma=5\%$) are presented.

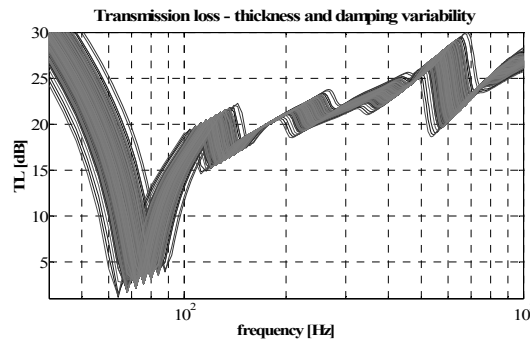


Figure 6.22 – TL behaviour with panel's thickness and damping variability

6.3.3 Effects of material properties variability on predicted TL

The variabilities introduced in the previous paragraph for thickness and damping properties are quite large for a metallic panel. Traditional metallic aerospace structures, in fact, have very small manufacturing tolerances and their geometrical and material's properties typically do not show an high scattering.

When composite materials are used, instead, their damping and stiffness characteristics depend on temperature and moisture variations. If viscoelastic layers are cocured in composite structures to increase the damping performance, the variability in manufacturing process increases as well as the lack of knowledge about the assembled structure properties.

Furthermore, the properties of the viscoelastic material itself are strongly dependant from operating temperature and frequency. In the Figure 6.23 the typical behaviour of shear modulus, G , and loss factor, η , with temperature, T , is shown.

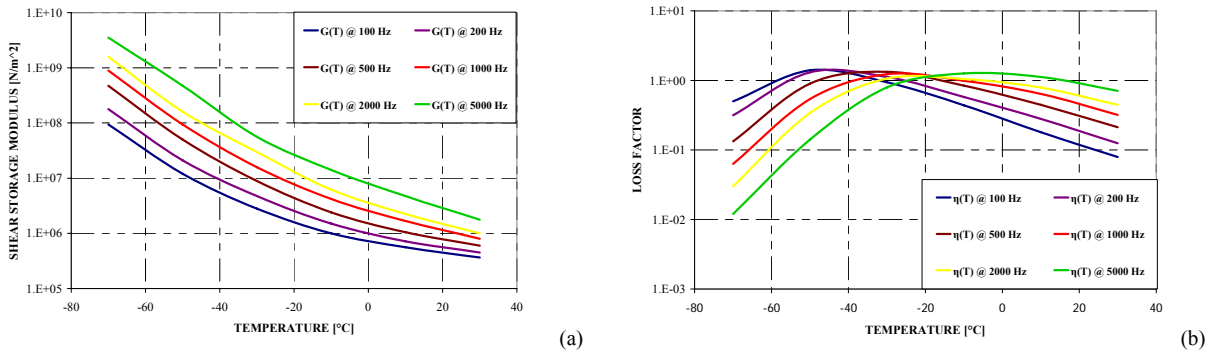


Figure 6.23 – Shear modulus and loss factor variability with T for a viscoelastic material

As it can be seen from the figure, it makes sense to analyze effects related to variability of viscoelastic material properties on transmission loss behaviour of layered damped composite panels.

With this aim, a FE model of a sandwich panel has been built with 12 composite layers and a viscoelastic layer 0.2 mm thick in the centre of the lamination sequence.

Panels dimensions were 600x200x2.57 mm and the FE mesh was suited to analyse panel's modal behaviour up to 4500 Hz, in order to predict TL in the range 40-3000 Hz.

The TL has been calculated with a frequency resolution of 2 Hz, applying the discrete coordinates approach.

In order to take into account damping effects, a complex modal analysis with complex Lanczos method (see MSC.Nastran Advanced Dynamic Analysis User's Guide) has been performed and complex eigenvalues and eigenvectors have been read from FE code output files and used for later processing.

In fact, the mode frequencies f and the modal damping η can be obtained from complex eigenvalues λ as:

$$f = \frac{1}{2\pi} \text{Im}\{\lambda\} ; \eta = -2 \frac{\text{Re}\{\lambda\}}{\text{Im}\{\lambda\}} \quad (6.6)$$

Shear modulus and loss factor of the viscoelastic materials have been introduced as random variable normally distributed, as in Table 6.8.

Property	Distribution	Mean	Coeff. Of Variance
Shear Modus G	Normal	1.0 E+7	10%
Loss Factor η	Normal	0.6	15%

Table 6.8 - Statistically characterized properties for the viscoelastic material

As performance function the minimum value of the transmission loss achieved in one third octave bands has been taken.

Monte Carlo, MV, AMV and AMV+ methods have been applied to evaluate the performance function distribution.

In the Figure 6.24 the results of different runs of analysis in terms of transmission loss are presented. The figure is referred to the frequency range 100-250 Hz.

It can be seen that the variability of the viscoelastic layer properties causes a strong variability of the predicted TL values, mainly in correspondence of the minimum value, at the frequency where the first panel's mode occur.

It seems there is almost no effect on the frequency of occurrence of this elastic mode, that is always around 216 Hz.

That can be explained with the fact that the damping layer contribution to mass and stiffness of the panel is quite low.

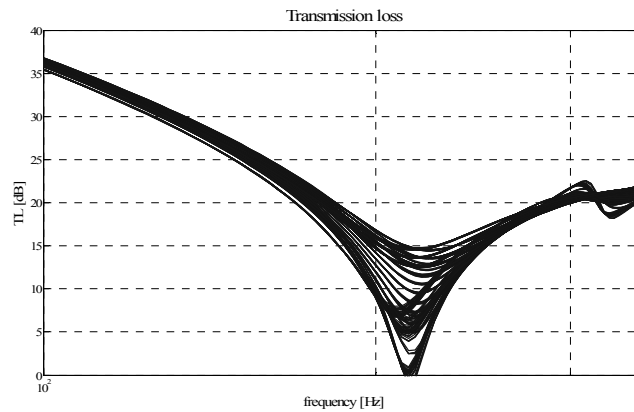


Figure 6.24 – TL behaviour with panel's thickness and damping variability

When looking at the performance function CDF, Figure 6.25, it can be appreciated that the range of variation of the minimum TL, is about 6 dB, a value that can make the difference between a good acoustic solution and a bad one.

Or, from another point of view, a lot of weight to be added on the aircraft in terms of soundproofing treatments.

Similar results are achieved from MC method, even if it have to be said that mean value and advanced mean value methods account for a lightly wider range of variation of the performance function, because of an overestimation of performance function distribution tails.

In the Figure 6.26 the distribution in the space of the random variables G and η of the 1000 samples generated for a Monte Carlo analysis is depicted, whereas in Figure 6.27

the results achieved by applying MC method with 200 and with 1000 samples are compared.

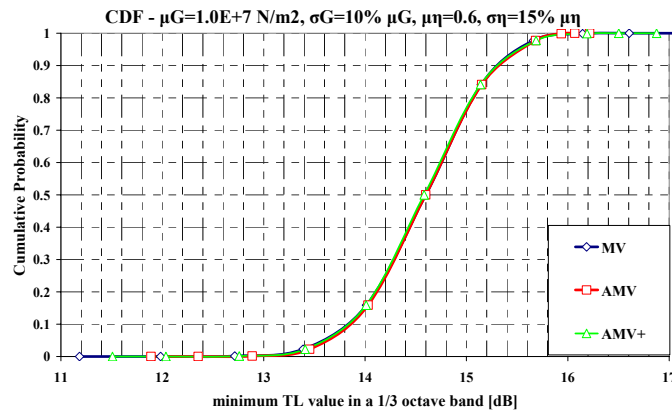


Figure 6.25 – CDF of the performance function, MV, AMV and AMV+

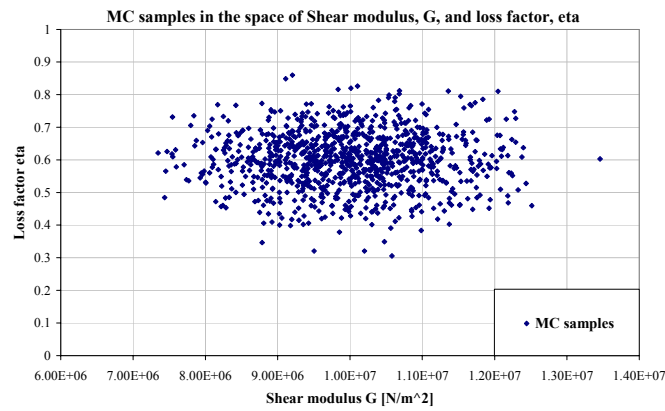


Figure 6.26 – CDF of the performance function calculated with MC method

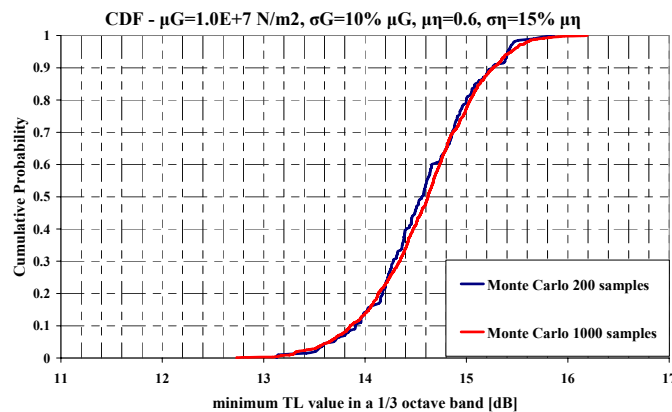


Figure 6.27 – CDF of the performance function calculated with MC method

Conclusions

This thesis is collocated in the framework of a consolidated experience acquired from the Vibration and Acoustics Group at Department of Aerospace Engineering of University of Naples in the field of vibroacoustics of transport aircraft during last 25 years. This topic in the past has been faced from a numerical point of view, except for the participation to experimental campaigns that took place in collaboration with industry. The present work and, in general, the activities of its author in last four years, contributed to build a laboratory where, other than the acoustic behaviour of small panels here presented, it is possible to measure impedance and absorption coefficient of soundproofing materials as well as dynamic complex modulus and loss factor of damping materials and treatments.

A small TL facility presents two main and conflicting properties i) the capability to perform fast and cheap measurements in order to evaluate different candidate solutions and ii) a careful analysis of the low frequency region results is required. It has been shown that, despite the announced and measured frequency limitations, the SMARF is a valid support for any engineering investigations and/or academic and research activities involving the group. Good numerical-experimental correlation achieved paved the way to improvements that soon will be made to the SMARF as possibility to perform measurements in presence of pressurization and temperature gradients.

The gained capability to perform experimental measurements allowed the group to enter the world of uncertainties and to broaden its view identifying the necessity to integrate traditional numerical approaches with statistical methods.

Well assessed numerical methodologies aimed to vibroacoustic prediction have been integrated with emerging probabilistic ones, also developing an in house code that gave the possibility to overcome limitations presented by commercial softwares available and that will be further used for research purposes. Achieved results confirmed the opportunity to apply probabilistic techniques to acoustic problems underlining the necessity to overcome traditional approaches when modelling parameters can have high variability, e.g. viscoelastic damping treatments, whose properties are strongly affected from manufacturing process and environmental conditions.

References and Bibliography

CHAPTER 1

1. H. Fletcher and W A Munson, Loudness, its definition, measurement and calculation, *J. Acoust. Soc. Am.*, 5, 1933, pp.82-108
2. D W Robinson and R S Dadson, A re-determination of the equal-loudness relations for pure tones, in *Br. J. Appl. Phys.*, 7, 1956, pp.166-181
3. L.L. Beranek, G.A. Work, Sound Transmission through Multiple Structures Containing Flexible Blankets, *J. Acoust. Soc. Am.*, 21 (4), 1949, pp.419-428
4. L.L. Beranek, *Acoustics*. First edition - 1954. Revised edition - 1986. American Institute of Physics, New York, 1954 (1986)
5. L. E. Kinsler, A.R. Frey, A.B. Coppens, J.V. Sanders, *Fundamentals of Acoustics*, Academic Press, 1982
6. F. Fahy. *Sound and structural vibration - Radiation, Transmission and Response*, Academic Press, 1985
7. L. Cremer, M. Heckl, and E.E. Ungar, *Structure-Borne Sound*, Springer-Verlag, 1988
8. A D. Pierce, *Acoustics: An Introduction to Its Physical Principles and Applications*, American Institute of Physics, New York, 1989
9. L.L. Beranek, I.L. Ver, *Noise and Vibration Control Engineering: Principles and Applications*, John Wiley and Sons, Inc., 1992
10. ISO 226-2003 *Acoustics - Normal equal-loudness-level contours*
11. ANSI S1.11-2004, *Specifications for Octave-Band and Fractional-Octave-Band Analog and Digital Filters*
12. ANSI S1.6-1984 (R2006), *Standard Preferred Frequencies, Frequency Levels, and Band Numbers for Acoustical Measurements*
13. F. Jacobsen, T. Poulsen, J. H. Rindel, A.C. Gade and M. Ohlrich, *Fundamentals of Acoustics and Noise Control*, Printed at Ørsted - DTU, Technical University of Denmark, Note n°31200, 2007

CHAPTER 2

14. W.C. Sabine, *Collected Papers on Acoustics (1900–1915)*, Peninsula, Los Altos, CA
15. A. H. Davis, Reverberation equations for two adjacent rooms connected by an incompletely soundproof partition, *Phil. Mag.*, 6 (50), 1925, pp.75-80
16. E. Buckingham, Theory and interpretation of experiments on the transmission of sound through partition walls, *Nat'l Bur. Stand. Sci. Papers*, 20, 1929, pp.194-199.
17. R.F Norris and C.A. Andree, An instrumental method of reverberation measurement, *J. Acoust. Soc. Am.* 1 (1), 1929, p.32.
18. C.F. Eyring, Reverberation time in 'dead' rooms, *J. Acoust. Soc. Am.* 1, 1930, p.168.
19. Von L. Cremer, Theorie der schalldämmung dünner Wände beu schrägem einfall, *Akustische Zeitschrift VII*, Drittes Heft, Siebenter Jahrgang, 1942
20. A. London, Transmission of Reverberant Sound through Single Walls, *J. Res. Natl. Bureau Stand.*, RP1998, 42, 1949, p.605
21. A. London, Transmission of reverberant sound through double walls, *J. Acoust. Soc. Am.*, 22 (2), 1950, pp.270-279.
22. A. London, Tentative recommended practice for laboratory measurement of airborne-sound transmission loss of building floors and walls (ASTM E 90-50 Tentative), *J. Acoust. Soc. Am.*, 23, 1951, pp.686-689
23. R. V. Waterhouse, Interference patterns in reverberant sound fields, *J. Acoust. Soc. Am.*, 27, 1955, pp.247-258

24. D. Ross, E.M. Kerwin, E.E. Ungar, Damping of plate flexural vibration by means of viscoelastic laminae, in *Structural Damping* (Ed. T.E. Ruzicka), ASME, New York, Sec. 111, 1959, pp.48-88
25. G. Kurtze, B. G. Watters, New Wall Design for High Transmission Loss or High Damping, *J. Acoust. Soc. Am.*, 31 (6), 1959, pp. 739-748
26. P.W. Smith Jr., Response and Radiation of Structural Modes Excited by Sound, *J. Acoust. Soc. Am.*, 34 (5), 1962, pp. 640-647
27. G. Maidanik, Response of ribbed plates to reverberant acoustic fields, *J. Acoust. Soc. Am.*, 34 (6), 1962, pp. 809-826
28. E.E. Ungar, E.M. Kerwin, Loss factors of viscoelastic systems in terms of energy concepts, *J. Acoust. Soc. Am.*, 34 (7), 1962, pp. 954-957
29. R.H. Lyon, Noise Reduction of Rectangular Enclosures With One Flexible Wall, *J. Acoust. Soc. Am.*, 35 (11), 1963, pp.1791 -1797.
30. R.H. Lyon, G. Maidanik, Review of some recent research on noise and structural vibration, NASA-TN-D-2266, 1964
31. R.H. Lyon, P.W. Smith Jr., Sound and structural vibration, NASA-CR-160, 1965
32. P. H. White and A. Powell, Transmission of random sound and vibration through a rectangular double wall, *J. Acoust. Soc. Am.*, 40 (4), 1966, pp.821-832
33. O.C. Zienkiewicz, R.L. Taylor, *The Finite Element Method*, volume 1 and 2, First published in 1967 by McGraw-Hill, Fifth edition published by Butterworth-Heinemann 2000
34. E.C. Sewell, Transmission of reverberant sound through a single-leaf partition surrounded by an infinite rigid baffle, *J. Sound Vib.*, 12 (1), 1970, pp.21-32
35. A.J. Price and M.J. Crocker, Sound Transmission through Double Panels Using Statistical Energy Analysis, *J. Acoust. Soc. Am.*, 47 (3) 1970, pp.683-693
36. M.C. Bhattacharya and R.W. Guy, Coincidence effect with sound waves in a finite plate, *J. Sound Vib.*, 18 (2), 1971, pp.157-169
37. A. C. Nilsson, Reduction index and boundary conditions for a wall between two rectangular rooms. Part I: Theoretical results, *Acustica* 26, 1972, pp.1-18
38. K.A. Mulholland, R.H. Lyon, Sound insulation at low frequencies, *J. Acoust. Soc. Am.*, 54 (4) 1973, pp.867-878
39. C.L. Dym, M.A. Lang, Transmission of sound through sandwich panels, *J. Acoust. Soc. Am.*, 56 (5), 1974, pp.1523-1532
40. C.L. Dym, C.S. Ventres, M.A. Lang, Transmission of sound through sandwich panels: a reconsideration, *J. Acoust. Soc. Am.*, 59 (2), 1976, pp.364-367
41. R.F. Gibson, R Plunkett, Dynamic stiffness and damping of fibre reinforced composite materials, *Shock Vibr. Digest*, 9 (2), 1977, pp.9-17
42. C.K. Barton., E.F. Daniels, Noise Transmission Through Flat Rectangular Panels Into a Closed Cavity, NASA TP-1321, 1978
43. A.Ordubadi and R.H. Lyon, Effect of orthotropy on the sound transmission through plywood panels, *J. Acoust. Soc. Am.*, 65 (1), 1979, pp.133-139
44. G.C. Everstine, Structural Analogies for Scalar Field Problems, *Int. J. Num. Meth. in Engrg.*, 17 (3), 1981, pp.471-476
45. G.C. Everstine, A Symmetric Potential Formulation for Fluid-Structure Interaction, *J. Sound Vib.*, 79 (1), 1981, pp.157-160
46. S. Gade, Sound intensity - Part I: Theory, *Brüel & Kjær Technical Review*, 3, 1982
47. C.D. Johnson, and D.A. Kienholz., Finite element prediction of damping in structures with constrained viscoelastic layers. *AIAA J.*, 20 (9), 1982, pp.1284-1290
48. L.A. Roussos, F.W. Grosveld, L. R. Koval and C. A. Powell, Noise Transmission Characteristics of Advanced Composite Structural Materials, *Proceedings of the 8th Aeroacoustics Conference*, Atlanta, GA, April 1983, AIAA Paper 1983-0694
49. F.W Grosveld, and V. L. Metcalf, Modal Response and Noise Transmission of Composite Panels, *AIAA Conference Publication*, CP 852, Part 2 of the

- AIAA/ASME/ASCE/AHS 26th Structures, Structural Dynamics and Materials Conference, Orlando, FL, April 1985, pp.617-628, AIAA Paper 1985-0789
50. L.A. Roussos, Noise Transmission Loss of a Rectangular Plate in an Infinite Baffle, NASA TP-2398, 1985
 51. A.D. Nashif, D.I.G. Jones, J.P. Henderson, Vibration Damping, John Wiley & Sons, 1985
 52. F.G. Leppington, E.G. Broadbent, K.H. Heron, & S.M. Mead, Resonant and nonresonant acoustic properties of elastic panels. I. The radiation problem. Proc. R. Soc. Lond., A 406, 1986, pp.139-171.
 53. F.G. Leppington, E.G. Broadbent, K.H. Heron, & S.M. Mead, Resonant and nonresonant acoustic properties of elastic panels. II. The transmission problem. Proc. R. Soc. Lond., A 412, 1986, pp.309-337
 54. D.A Saravanos, C.C. Chamis, The Effects of Interply Damping Layers on the Dynamic Response of Composite Structures, NASA TM 104497, 1991
 55. J.A. Moore and R.H. Lyon, Sound transmission loss characteristics of sandwich panel constructions, J. Acoust. Soc. Am., 89 (2), 1991, pp.777-791
 56. D.J. Oldham and S.N. Hilarby, The Acoustical Performance of Small Close Fitting Enclosures, Part 1; Theoretical Models, J. Sound Vib., 150 (2), 1991, pp.261-281
 57. M. J. Crocker, A Systems Approach to the Transmission of Sound and Vibration Through Structures, Proceedings of Noise-Con 94, 1994, pp. 525-533
 58. K. A. Cunefare and M. Noelle Currey, On the exterior acoustic radiation modes of structures, J. Acoust. Soc. Am., 96 (4), 1994, pp.2302-2312
 59. M.D. Rao, R. Echempati, S. Nadella., Dynamic analysis and damping of composite structures embedded with viscoelastic layers, Composites Part B, 28B, 1997, pp.547-554
 60. R. Chandra, S.P. Singh, K. Gupta, Damping studies in fiber-reinforced composites: a review, Composite Structures 46, 1999, pp.41-51
 61. J.Hald, Non stationary STSF, Brüel & Kjær Technical Review, 1, 2000.
 62. V. Hongisto, Airborne Sound Insulation of Wall Structures - Measurement and Prediction Methods, Helsinki University of Technology, Espoo, Finland, Report 56, 2000
 63. D.I.G. Jones, Handbook of Viscoelastic Vibration Damping, John Wiley & Sons, New York, 2001
 64. J.J. Christensen and J. Hald, Beamforming, Brüel & Kjær Technical Review, 1, 2004
 65. P. J. Shorter, Wave propagation and damping in linear viscoelastic laminates, J. Acoust. Soc. Am., 115 (5), 2004, pp.1917-1925
 66. B. Mace, D. Duhamel, M.J. Brennan, L. Hinke, Finite Element Prediction of Wave Motion in Structural Waveguides, J. Acoust. Soc. Am., 117 (5), 2005, pp. 2835-2843
 67. M.J. Crocker, Development of composite materials with high passive damping properties, Final Technical Report, U.S. Office of Naval Research, Project N00014-01-1-0592, 2006
 68. L.L. Beranek, Analysis of Sabine and Eyring equations and their application to concert hall audience and chair absorption, J. Acoust. Soc. Am., 120, 2006, pp.1399-1410

CHAPTER 3

69. M.R. Schroeder, Acustica 4, 1954, p.594.
70. K.H. Kuttruff and R. Thiele, Acustica 4, 1954, p.614.
71. M.R. Schroeder, and K.H. Kuttruff, On frequency response curves in rooms, comparison of experimental, theoretical, and Monte Carlo results for the average frequency spacing between maxima, J. Acoust. Soc. Am., 34 (1), 1962, pp.76-80
72. T.J. Schultz., Sound power measurements in a reverberant room, J. Sound and Vib., 16 (1), 1971, pp.119-129

73. R.E. Halliwell and A.C.C. Warnock, Sound transmission loss: Comparison of conventional techniques with sound intensity technique, *J. Acoust. Soc. Am.*, 77 (6), 1985, pp.2094-2103
74. H. Thrane, J. Wismer, H. Konstantin-Hansen, S. Gade, Practical Use of the Hilbert Transform, Brüel & Kjær, Application Note, 1994
75. ISO 3743-1:1994, Acoustics - Determination of sound power levels of noise sources - Engineering methods for small, movable sources in reverberant fields - Part 1: Comparison method for hard-walled test rooms
76. ISO 3743-2:1994, Acoustics - Determination of sound power levels of noise sources using sound pressure - Engineering methods for small, movable sources in reverberant fields - Part 2: Methods for special reverberation test rooms
77. ISO 140-3:1995, Acoustics - Measurement of Sound Insulation in Buildings and of Building Elements - Part 3: Laboratory Measurements of Airborne Sound Insulation of Building Element
78. M.R. Schroeder, The "Schroeder frequency" revisited, *J. Acoust. Soc. Am.*, 99 (5), 1996, pp.3240-3241
79. ISO 140-1:1997, Acoustics - Measurement of sound insulation in buildings and of building elements - Part 1: Requirements for laboratory test facilities with suppressed flanking transmission
80. ISO 3741-1999, Acoustics - Determination of sound power level of noise sources - Precision methods for reverberation rooms, International Organization for Standardization.
81. ASTM C 423-02 Standard Test Method for Sound Absorption and Sound Absorption Coefficients by the Reverberation Room Method
82. ASTM C 634-02 Standard Terminology Relating to Environmental Acoustics
83. ASTM E 2249 – 02 Standard Test Method for Laboratory Measurement of Airborne Transmission Loss of Building Partitions and Elements Using Sound Intensity
84. ASTM E 1332-90 R03 Standard Classification for Determination of Outdoor-Indoor Transmission Class
85. I. Chun, B. Rafaely, and P. Joseph, Experimental investigation of spatial correlation in broadband reverberant sound fields, *J. Acoust. Soc. Am.*, 113 (4), 2003, pp.1995-1998
86. ASTM E-90-04, Standard test method for laboratory measurement of airborne sound transmission loss of building partitions, The American Society for Testing and Materials
87. ASTM E 413-04 Standard Classification for Rating Sound Insulation
88. R. Velotto Romano, A. Paonessa, F. Marulo, T. Polito, Applicazione della Trasformata di Hilbert per il calcolo dello smorzamento strutturale in condizioni di elevata densità modale, Proceedings of the del XVIII National Congress of the Italian Association of Aeronautics and Astronautics AIDAA, Volterra (Pi), September 2005, paper n°153 (in Italian)
89. F. Marulo, T. Polito, A. Paonessa, Acoustic Measurements in a Small Transmission Loss Facility, Proceedings of ISMA 2006 Conference, Leuven, Belgium, September 2006
90. T. Polito, E. Barbieri, A. Cammarano, S. De Rosa, F. Marulo, Small Acoustic Research Facility (SMARF) for the Plate Qualification: Design, Assembly and Measurements, Proceedings of the 13th AIAA/CEAS Aeroacoustics Conference, Rome, May 2007, AIAA 2007-3581

CHAPTER 4

91. E.H. Dowel, and H.M. Voss, The Effect of a Cavity on Panel Vibration, *AIAA J.* 1 (2), 1963, p.476

92. L. Cremer, M. Heckl, Structure-Borne Sound, First edition 1966, 2nd edition, translated and revised by E. E. Ungar, Springer, Berlin, 1988
93. A.J. Pretlove, Forced Vibrations of a Rectangular Plate Backed by a Closed Rectangular Cavity. *J. Sound Vib.*, 3 (3), 1966, pp.252-261
94. J.A. Wolf Jr., D.J. Nefske, NASTRAN modeling and analysis of rigid and flexible walled acoustic cavities, NASA Langley Res. Center NASTRAN User's Experiences, 1975, pp.615-631
95. R.W. Guy, The response of a cavity backed panel to external airborne excitation: A general analysis. *J. Acoust. Soc. Am.*, 65 (3), 1979, pp.719-731
96. Y.P Lu, J.W. Killian, and G.C. Everstine, Vibrations of three layered damped sandwich plate composites, *J. Sound and Vib.*, 64, 1979, pp.63-71
97. D.J. Nefske, J.A. Wolf Jr., and L.J. Howell, Structural-acoustic finite element analysis of the automobile compartment: A review of current practice, *J. Sound and Vib.*, 80 (2), 1982, pp.247-266
98. S.L. Liguore, and J.B. Kosmatka, Evaluation of analytical methods to predict constrained layer damping behaviour, Proceedings of VI International Modal Analysis Conference, Kissimmee, FL, USA, 1988, pp. 421-427
99. J. Pan and D.A. Bies. The effect of fluid-structural coupling on sound waves in an enclosure-theoretical part, *J. Acoust. Soc. Am.*, 87 (2), 1990, pp.691-707
100. G. C. Everstine and F. M. Henderson, Coupled finite element/boundary element approach for fluid-structure interaction, *J. Acoust. Soc. Am.*, 87 (5), 1990, pp.1938-1947
101. M. Chargin, and O. Gartmeier, A Finite Element Procedure for Calculating Fluid-Structure Interaction Using MSC/ NASTRAN, NASA TM-102857, 1990
102. C.M. Fernholz, J.H. Robinson, Fully-Coupled Fluid Structure Vibration Analysis Using MSC NASTRAN, NASA-TM-110215, 1996
103. G.C. Everstine, Finite element formulations of structural acoustics problems. *Computers & Structures*, 65(2), 1997, pp.307-321
104. S. De Rosa, F. Franco, F. Marulo, G. Esposito, F. Conicella, Full Validation of the Structural-Acoustic Response of a Simple Enclosure, *AIAA J. of Aircraft*, 36 (5), 1999, pp.866-875
105. A.S. Plouin, E.Balmes, A test validated Model of Plates with Constrained Viscoelastic Materials, Proceedings of the XVII International Modal Analysis Conference, Kissimmee, FL, USA, 1999, pp. 194-200 .
106. A.S. Plouin, and E. Balmes, Steel/viscoelastic/steel sandwich shells computational methods and experimental validations, Proceedings XVIII International Modal Analysis Conference, San Antonio, TX, USA, 2000, pp. 384-390
107. E.Balmes, A. Bobillot, Analysis and Design Tools for Structures Damped by Viscoelastic Materials, Proceedings of the XX International Modal Analysis Conference, Los Angeles, CA, USA, 2002
108. R. Moreira and J. D. Rodrigues, Constrained Damping Layer Treatments: Finite Element Modeling, *Journal of Vibration and Control*, 10, 2004, pp. 575-595
109. E. Barbieri, A. Cammarano, S. De Rosa, F. Franco, Waveguides of a Laminate Composite Panel using Spectral Finite Element Theory, *Journal of Vibration and Control*, in press

CHAPTER 5

110. S. Ulam, R. D. Richtmyer, and J. von Neumann, Statistical methods in neutron diffusion. Los Alamos Scientific Laboratory report LAMS-551, 1947.
111. N. Metropolis and S. Ulam, The Monte Carlo method. *Journal of the American Statistical Association* 44, 1949, pp. 335-341

112. Rosenblatt, M., "Remarks on a Multivariate Transformation," *Annals of Mathematical Statistics*, 23 (3), 1952, pp.470-472
113. G.P. Box, and D.W. Behnken, Some New Three-Level Designs for the Study of Quantitative Variables, *Technometrics*, 2, 1960, pp.455-475
114. A. Nataf, Determination des distributions de probalites dont les marges sont donnees. *Comptes Rendus de l'Academie des Sciences* 225, 1962, pp.42-43..
115. L.A. Zadeh, Fuzzy sets, *Information and Control*, 8, 1965, pp.338-353
116. R.E. Moore., *Interval Analysis*. Prentice-Hall, Inc., Englewood Cliffs, New Jersey, 1966
117. M.L. Shooman, *Probabilistic Reliability: An Engineering Approach*, McGraw-Hill, 1968
118. A.M. Hasofer, and N.C. Lind, Exact and Invariant Second-Moment Code Format, *J. of Engrg. Mech. Div., ASCE*, 100 (EM1), 1974
119. L.A. Zadeh., *Fuzzy Sets as a Basis for a Theory of Possibility*. *Fuzzy Sets and Systems*, 1, 1978, pp.3-28
120. R. Rackwitz, and B. Fiessler, Structural Reliability Under Combined Load Sequences, *J. of Computers and Structures*, 9, 1978, pp. 489-494
121. M. D. McKay, W.J. Conover, and R.J. Beckman, A comparison of three methods for selection values of input variables in the analysis of output from a computer code. *Technometrics*, 22 (2), 1979, pp. 239-245
122. K. Breitung, Asymptotic Approximations to Multinormal Integral, *J. of Engrg. Mech.*, 110 (3), 1984, pp.357-366
123. I. Miller, and J. Freund, *Probability and Statistics for Engineers*, Prentice Hall, Englewood Cliffs, 1985
124. H.O. Madsen., S. Krenk, and N.C. Lind., *Methods of Structural Safety*, Prentice Hall Inc., Englewood Cliffs, New Jersey, 1986
125. Y. Ben-Haim, and I. Elishakoff, *Convex Models of Uncertainty in Applied Mechanics*. Elsevier Science, Amsterdam, 1990
126. Y.-T. Wu, H.R. Millwater, and T.A. Cruse., *An Advanced Probabilistic Structural Analysis Method for Implicit Performance Functions*, *AIAA J.*, 28 (9), 1990, pp.1663-1669
127. P. Walley., *Statistical Reasoning with Imprecise Probabilities*. Chapman and Hall, London, 1991.
128. D. Berleant, Automatically verified reasoning with both intervals and probability density functions. *Interval Computations* 2, 1993, pp.48-70
129. Y.-T., Wu, S.B. Gureghian, and R.B. Codell, Sensitivity and Uncertainty Analysis Applied to One-Dimensional Transport in a Layered Fractured Rock. Part 11: Probabilistic Methods Based on the Limit-State Approach, *Nuclear Technology J.*, 104 (2), 1993, pp.297-308
130. R.H. Myers, D.C. Montgomery, *Response Surface Methodology: Process and Product Optimization Using Designed Experiments*, Wiley & Sons, 1995
131. S. Ferson, and L.R. Ginzburg, Different methods are needed to propagate ignorance and variability. *Reliab. Engng. Syst. Saf.* 54, 1996, pp.133-144
132. Y. Ben-Haim, Reliability of Vibrating Structures with Uncertain Inputs, *The Shock and Vibration Digest*, 30, 1998, pp.106-113
133. I. Elishakoff, *Probabilistic Theory of Structures*, second edition, New York, Dover Publications, 1999
134. R.E. Melchers., *Structural Reliability, Analysis and Prediction* J. Wiley & Sons, New York, 1999
135. W. Oberkampf, S. DeLand, B. Rutherford, K. Diegert, K. Alvin, A new methodology for the estimation of total uncertainty in computational simulation, in: *Proceedings of the 40th AIAA/ASME/ASCE/AHS/ASC Structures, Structural Dynamics and Materials Conference*, AIAA-99-1612, 1999, pp.3061-3083

136. H. Pradlwarter, G. Schuëller, Assessment of low probability events of dynamical systems by controlled Monte Carlo simulation, *Prob. Engrg. Mech.* 14, 1999, pp.213–227.
137. M.W. Long, J.D. Narciso, Probabilistic Design Methodology For Composite Aircraft Structures, DOT/FAA/AR-99/2, 1999
138. H.P. Kan, Assessment of Probabilistic Certification Methodology for Composite Structures, DOT/FAA/AR-00/74
139. A. Haldar and S. Mahadevan, Reliability Assessment Using Stochastic Finite Element Analysis, John Wiley & Sons, New York, 2000
140. D.S. Riha, B.H. Thacker, D.A. Hall, T.R. Auel, and S.D. Pritchard, Capabilities and Applications of Probabilistic Methods in Finite Element Analysis, *Int. J. of Materials & Product Technology*, 16 (4/5), 2001
141. B.H. Thacker, D.S. Riha, H.R. Millwater, and M.P. Enright, Errors and Uncertainties in Probabilistic Engineering Analysis, Proceedings of AIAA/ASME/ASCE/AHS/ASC 42nd Structures, Structural Dynamics, and Materials (SDM) Conf., AIAA Paper 2001-1239, Seattle, WA, April 2001
142. Department of Defense, Composite Materials Handbook, MIL-HDBK-17-2F, 2002
143. B.D. Youn, K.K. Choi, Y.H. Park, Hybrid Analysis Method for Reliability-Based Design Optimization, *J. of Mech. Design*, 125, 2003, pp.221-232
144. B.D. Youn, K.K. Choi, Liu Du, Adaptive Probability Analysis Using An Enhanced Hybrid Mean Value Method, *Journal of Structural and Multidisciplinary Optimization*, 29 (2), 2004, pp.134-148
145. Riha, D.S. and B.H. Thacker, NESSUS Capabilities for Ill-Behaved Performance Functions, Proceedings of the AIAA/ASME/ASCE/AHS/ASC Structures, Structural Dynamics, and Materials (SDM) Conference, Palm Springs, California, April 2004
146. B.H. Thacker, D.S. Riha, and L.J. Huyse, Robust Most Probable Point Search Algorithm for Difficult Performance Functions, Proceedings of the ASCE Joint Specialty Conference on Probabilistic Mechanics and Structural Reliability, July 26-28, Albuquerque, New Mexico, 2004
147. J.M. Rios Fonseca, Uncertainty in Structural Dynamic Models, PhD Thesis, University of Wales Swansea, 2005
148. Moens, D., Vandepitte, D., A survey of non-probabilistic uncertainty treatment in finite element analysis, *Comput. Methods Appl. Mech. Engrg.*, 194, 2005, pp.1527-1555
149. Y. Ben-Haim, *Info-Gap Decision Theory: Decisions Under Severe Uncertainty*, Academic Press, 2nd edition, 2006.
150. B.H. Thacker, D.S. Riha, S. H.K. Fitch, L. J. Huyse and J. B. Pleming, Probabilistic engineering analysis using the NESSUS software, *Structural Safety*, 28(1-2), *Structural Reliability Software*, 2006, pp.83-107
151. G.I. Schuëller, On the Treatment of Uncertainties in Structural Mechanics and Analysis, *Computers & Structures*, 85 (5-6), 2007, pp. 235-243

CHAPTER 6

152. D.J. Ewins, *Modal Testing: Theory and Practice*, Research Studies, John Wiley and Sons, New York, 1984
153. MSC.Nastran Advanced Dynamic Analysis User's Guide
154. NESSUS Theoretical Manual, Version 7.0, Southwest Research Institute, 2001
155. Noesis Solutions, OPTIMUS, Rev. 5.2, 2006
156. T. Polito, F. Marulo, Probabilistic finite elements for vibroacoustic applications, Proceedings of the 12th AIAA/CEAS Aeroacoustics Conference, AIAA Paper 2006-2659, Cambridge, MA, May 2006
157. T. Polito, F. Marulo., R. d'Ippolito, D. Turo, N. Tsannetakis., Probabilistic analysis and optimization of the acoustic radiation of a composite panel, Proceedings of the 13th

- AIAA/CEAS Aeroacoustics Conference, AIAA Paper 2007-3573, Rome, Italy, May 2007
158. T.Polito, Probabilistic analysis of panels sound transmission loss and correlation with experimental results, Proceedings of the 1st International Conference on Uncertainty in Structural Dynamics, Sheffield, UK, June 2007, pp.121-130

Appendix A – Plate flexural vibrations

Equation that determines bending vibrations of a plate descends from equilibrium of moments in direction x and y and of forces in direction z .

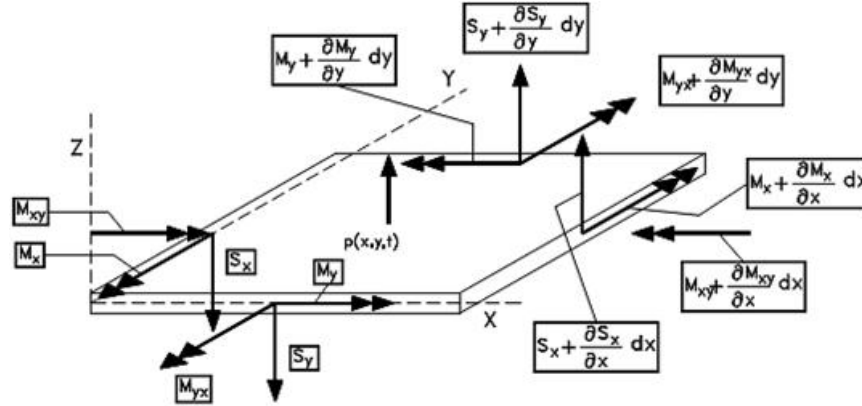


Figure A.0.1 – Force and Moments definition

$$\frac{\partial M_x}{\partial x} + \frac{\partial M_{xy}}{\partial y} - S_x = 0 \quad (\text{A.1})$$

$$\frac{\partial M_{xy}}{\partial x} + \frac{\partial M_y}{\partial y} - S_y = 0 \quad (\text{A.2})$$

$$\frac{\partial S_x}{\partial x} + \frac{\partial S_y}{\partial y} + p(x, y, t) = \rho_s \frac{\partial^2 w}{\partial t^2} \quad (\text{A.3})$$

Where $\rho_s \frac{\partial^2 w}{\partial t^2}$, directed along z , is the inertial force.

By deriving the first equation with respect to x and the second equation with respect to y and then substituting in the third one, it can be achieved:

$$\frac{\partial^2 M_x}{\partial x^2} + 2 \frac{\partial^2 M_{xy}}{\partial x \partial y} + \frac{\partial^2 M_y}{\partial y^2} + p(x, y, t) = \rho_s \frac{\partial^2 w}{\partial t^2} \quad (\text{A.4})$$

The relation between moments and curvatures can be obtained considering that, following lamination classic theory, membrane and bending behaviour of the plate are uncoupled for a symmetric laminate.

$$\begin{bmatrix} M_x \\ M_y \\ M_{xy} \end{bmatrix} = - \begin{bmatrix} D_{11} & D_{12} & D_{16} \\ D_{12} & D_{22} & D_{26} \\ D_{16} & D_{26} & D_{66} \end{bmatrix} \begin{bmatrix} \kappa_x \\ \kappa_y \\ \kappa_{xy} \end{bmatrix} \quad (\text{A.5})$$

Where D is called bending stiffness matrix of the laminate and the curvatures κ are related to the derivatives of the displacements from the following relations:

$$\begin{bmatrix} \kappa_x \\ \kappa_y \\ \kappa_{xy} \end{bmatrix} = \begin{bmatrix} \frac{\partial^2 w}{\partial x^2} \\ \frac{\partial^2 w}{\partial y^2} \\ \frac{\partial^2 w}{\partial x \partial y} \end{bmatrix} \quad (\text{A.6})$$

By substituting the (A.6) in the (A.4), the equation of the bending vibrations of an orthotropic plate is achieved:

$$D_{11} \frac{\partial^4 w}{\partial x^4} + 4D_{16} \frac{\partial^4 w}{\partial x^3 \partial y} + 2(D_{12} + 2D_{66}) \frac{\partial^4 w}{\partial x^2 \partial y^2} + 4D_{26} \frac{\partial^4 w}{\partial x \partial y^3} + D_{22} \frac{\partial^4 w}{\partial y^4} + \rho_s \frac{\partial^2 w}{\partial t^2} = p(x, y, t) \quad (\text{A.7})$$

If the bending and twisting stiffnesses of the laminate are uncoupled, it results that $D_{16}=D_{26}=0$ and the laminate is called to have the property of special orthotropy. The analysis of laminated plates is simplified if the conditions for special orthotropy are satisfied. Also, because end load and shear, and bending and twisting moments, are all uncoupled, distortion during manufacture is minimised.

In the hypothesis of special orthotropy, the previous equation becomes:

$$D_{11} \frac{\partial^4 w}{\partial x^4} + 2(D_{12} + 2D_{66}) \frac{\partial^4 w}{\partial x^2 \partial y^2} + D_{22} \frac{\partial^4 w}{\partial y^4} + \rho_s \frac{\partial^2 w}{\partial t^2} = p(x, y, t) \quad (\text{A.8})$$

The homogeneous form of equation (A.8) can be solved by imposing for the flexural displacement the steady state form:

$$w(x, y, t) = W(x, y) e^{j\omega t}$$

With $W(x, y)$ that satisfies boundary conditions.

If the plate is simply supported along the edges, these conditions are:

$$W(x, 0) = W(x, b) = W(0, y) = W(a, y) = 0 \quad \forall (x, y) \in [a, b] \quad (\text{A.9})$$

$$M_x(x, 0) = M_x(x, b) = M_x(0, y) = M_x(a, y) = 0 \quad \forall (x, y) \in [a, b] \quad (\text{A.10})$$

$$M_y(x, 0) = M_y(x, b) = M_y(0, y) = M_y(a, y) = 0 \quad \forall (x, y) \in [a, b] \quad (\text{A.11})$$

We can choose for the spatial displacement an expression as:

$$W(x, y) = \sum_{m=1}^{\infty} \sum_{n=1}^{\infty} W_{mn} \sin(k_x x) \sin(k_y y) \quad (\text{A.12})$$

That, if k_x and k_y are correctly chosen, satisfies also the boundary conditions introduced for the bending moments. In fact, it results:

$$M_x = -D_{11} \frac{\partial^2 w}{\partial x^2} - D_{12} \frac{\partial^2 w}{\partial y^2} \quad (\text{A.13})$$

$$M_y = -D_{12} \frac{\partial^2 w}{\partial x^2} - D_{22} \frac{\partial^2 w}{\partial y^2} \quad (\text{A.14})$$

That, by substituting for $w(x,y,t)$ the expression of the generic mode shape becomes:

$$M_x = -(D_{11}k_x^2 + D_{12}k_y^2)W(x,y) \quad (\text{A.15})$$

$$M_y = -(D_{12}k_x^2 + D_{22}k_y^2)W(x,y) \quad (\text{A.16})$$

Then, if the expression found for $W(x,y)$ satisfies the boundary conditions for the displacements, all the others are satisfied in the same manner.

Considering the generic mode shape:

$$W(x,y) = W_{mn} \sin(k_x x) \sin(k_y y) \quad (\text{A.17})$$

and applying the boundary conditions (A.9) leads to the relations:

$$W_{mn} \sin(k_x x) \sin(k_y b) = 0 \quad \forall x \in [a, b] \Rightarrow bk_y = n\pi \quad (\text{A.18})$$

$$W_{mn} \sin(k_x a) \sin(k_y y) = 0 \quad \forall y \in [a, b] \Rightarrow ak_x = m\pi \quad (\text{A.19})$$

From where it can be achieved that:

$$k_x = \frac{m\pi}{a} \quad ; \quad k_y = \frac{n\pi}{b}$$

with k_x and k_y bending wavenumbers.

By substituting in the (A.12) it results:

$$W(x,y) = \sum_{m=1}^{\infty} \sum_{n=1}^{\infty} W_{mn} \sin\left(\frac{m\pi}{a}x\right) \sin\left(\frac{n\pi}{b}y\right) \quad (\text{A.20})$$

From where it descends that the solution of the homogeneous equation of the bending vibration of a plate can be expressed as:

$$w(x,y,t) = \sum_{m=1}^{\infty} \sum_{n=1}^{\infty} W_{mn} \sin\left(\frac{m\pi}{a}x\right) \sin\left(\frac{n\pi}{b}y\right) \sin(\omega t) \quad (\text{A.21})$$

By substituting the generic eigenfunction in the equation (A.8) with $p=0$ leads to relation:

$$\left[D_{11}k_x^4 + 2(D_{12} + 2D_{66})k_x^2k_y^2 + D_{22}k_y^4 - \rho_s\omega^2 \right] W(x,y) = 0 \quad (\text{A.22})$$

From where it can be achieved the expression of the bending natural frequencies of the panel:

$$f_{mn} = \frac{\omega_{mn}}{2\pi} = \frac{1}{2\pi} \sqrt{\frac{D_{11}k_x^4 + 2(D_{12} + 2D_{66})k_x^2k_y^2 + D_{22}k_y^4}{\rho_s}} \quad (\text{A.23})$$

That, for an homogeneous panel $D_{11} = D_{22} = D_{66} = D$; $D_{12} = 0$ is in the well known form:

$$f_{mn} = \frac{\omega_{mn}}{2\pi} = \frac{1}{2\pi} \sqrt{\frac{D(k_x^2 + k_y^2)^2}{\rho_s}} = \frac{1}{2\pi} \sqrt{\frac{D}{\rho_s}} \left[\left(\frac{m\pi}{a} \right)^2 + \left(\frac{n\pi}{b} \right)^2 \right] = \frac{\pi}{2} \sqrt{\frac{D}{\rho_s}} \left[\left(\frac{m}{a} \right)^2 + \left(\frac{n}{b} \right)^2 \right] \quad (\text{A.24})$$

If the complete form of the equation (A.8) is considered, it can be derived the modal forced response of the panel in terms of superposition of mode shapes, opportunely weighted.

The generic solution can be expressed in modal coordinates as:

$$w_{mn}(x, y, t) = W_{mn} \sin\left(\frac{m\pi}{a}x\right) \sin\left(\frac{n\pi}{b}y\right) q_{mn}(t) \quad (\text{A.25})$$

Where $q_{mn}(t)$, called modal coordinate or generalized coordinate, is non dimensional and takes into account temporal behaviour of the displacements. By using the property of orthogonality of the eigenfunctions, the equation (A.8) can be expressed in the form:

$$\ddot{q}_{mn}(t) + q_{mn}(t)\omega_{mn}^2 = \frac{P_{mn}}{\gamma_{mn}} \quad (\text{A.26})$$

Where P_{mn} , given by the relation:

$$P_{mn}(t) = \int_0^a \int_0^b p(x, y, t) \sin\left(\frac{m\pi x}{a}\right) \sin\left(\frac{n\pi y}{b}\right) dx dy \quad (\text{A.27})$$

is the generalized forcing pressure and γ_{mn} is the generalized mass:

$$\gamma_{mn} = \int_0^a \int_0^b \rho_s \sin^2\left(\frac{m\pi x}{a}\right) \sin^2\left(\frac{n\pi y}{b}\right) dx dy = \frac{\rho_s ab}{4} \quad (\text{A.28})$$

By solving the equation (A.26), the forced response of the panel can be achieved as sum of the response to individual modes:

$$w(x, y, t) = \sum_{m=1}^{\infty} \sum_{n=1}^{\infty} W_{mn} \sin\left(\frac{m\pi}{a}x\right) \sin\left(\frac{n\pi}{b}y\right) q_{mn}(t) \quad (\text{A.29})$$

response to individual modes:

$$w(x, y, t) = \sum_{m=1}^{\infty} \sum_{n=1}^{\infty} W_{mn} \sin\left(\frac{m\pi}{a}x\right) \sin\left(\frac{n\pi}{b}y\right) q_{mn}(t) \quad (\text{A.30})$$

If the property of special orthotropy is not verified, the derivatives:

$$D_{16} \frac{\partial^4 w}{\partial x^3 \partial y} ; D_{26} \frac{\partial^4 w}{\partial x \partial y^3}$$

are not equal to zero, then the solution can not be expressed anymore in terms of Fourier series. In this case variational approaches, as Rayleigh-Ritz method, can be used.